

**LOW-LYING COLLECTIVE EXCITATIONS IN $^{18}\text{F}_{\text{g.s.}}$ and $^{18}\text{F}^{\text{m}}$ STUDIED VIA
INTERMEDIATE-ENERGY COULOMB EXCITATION**

by

James Aaron Zimmerman

A dissertation submitted in partial fulfillment
of the requirements for the degree of
Doctor of Philosophy
(Chemistry)
in The University of Michigan
2000

Doctoral Committee:

Professor Fred Becchetti, Co-chair
Professor Richard Sacks, Co-chair
Professor Thomas Glasmacher, Michigan State University
Professor Joseph Marino
Professor Robert Sharp

To my adoring wife Andrea
and my parents

ACKNOWLEDGMENTS

A hardy thanks to all of the support staff I relied on through the difficult process of graduate school. First, to the members of my dissertation committee: I thank each and every one of you for the critical comments and positive perspectives that allowed me to achieve my goals. Your presence and guidance were crucial to this process. Second, to my adoring wife who stood by me through the good times (and the bad) and to my parents who gave me the room to explore as a child. A big thank you to the nuclear physics group at Michigan. Don, Tom, and especially Mu, thank you for your patience and your companionship during the frequent trip to Notre Dame and MSU.

I would also like to thank the helpful group of researchers at MSU: Reg Ronningen, Thomas, Boris, Rich, Heiko, and the A1200 staff. Without your help and that of the cyclotron staff, this research could not have been so successful. My time spent at the Nuclear Structure Lab at Notre Dame would have been much less interesting without all of the fine scientists I worked with. Thanks to the Hope College contingent (Paul, Graham, and Pete), and the cast of characters at the Tandem (Don, Stuart, Peter, Dr. Kolata, et al.) for showing me the ropes! Thank goodness for rotary hammers as well. My final thanks has been reserved to the four master teachers who made graduate school bearable. Without your interest and encouragement, my career path could have turned out horribly different. My deepest thanks to Brian Coppola, Nancy Kerner, Barbara Weathers, and Marian Hallada. Thank you all for shaping my time at the University of Michigan.

TABLE OF CONTENTS

DEDICATION	II
ACKNOWLEDGMENTS	III
LIST OF TABLES	V
LIST OF FIGURES	VII
LIST OF APPENDICES	X
CHAPTER	
1. Introduction.....	1
2. Experimental Setup and Detector Calibration.....	17
3. The Coulomb Excitation of ^{197}Au and ^{12}C	41
4. The Coulomb Excitation of $^{18}\text{F}_{g.s.}$ and $^{18}\text{F}^m$	57
5. Future Outlook: The Accelerated Emission of Gamma Rays from the 162-ns ^{18}F Isomer Induced by the Coulomb Interaction	75
APPENDICES	89
REFERENCE LIST	106

LIST OF TABLES

Table

2.1	Data on the optimization of $^{18}\text{F}^m$ yield at the face of the Zero Degree Detector by secondary beam-tuning, using the 46 mg/cm^2 thick ^{12}C production target.....	23
2.2	Data on the optimization of $^{18}\text{F}^m$ yield at the face of the Zero Degree Detector by secondary beam-tuning, using the 8.9 mg/cm^2 thin ^{12}C production target.....	23
2.3	Energy calibration and energy resolutions of the eleven detectors that form the inner ring of the NSCL large-angle γ -array, using the ^{88}Y and ^{228}Th calibration sources.....	34
2.4	Calibration data for the two HPGe detectors using to monitor the secondary beam production of $^{18}\text{F}^m$	40
3.1	Computational Fits for the yield of the 548 keV γ -ray from ^{197}Au after Coulomb excitation.....	47
3.2	Sources of uncertainty included in the final ^{197}Au Coulomb excitation cross section.....	48
3.3	Experimental and Theoretical $B(E2\uparrow)$ values for the $7/2^+$ to $3/2^+$ transition in ^{197}Au	48
3.4	Fits of the 4.4 MeV photopeak and first-escape peak due to the Coulomb excitation of the ^{12}C beam fragments.....	55
3.5	Sources of uncertainty included in the calculated ^{12}C Coulomb excitation cross section	55
3.6	Experimental and Theoretical $B(E2\uparrow)$ values for the 2^+ to 0^+ transition in ^{12}C	56
4.1	Fits of the 2.1 MeV photopeak and the 2.5 MeV photopeak due to the Coulomb excitation of ^{18}F ground state beam fragments	67
4.2	Sources of uncertainty included in the final error calculated for the ^{18}F ground state Coulomb cross section value.....	68

4.3	Comparison of experimental and theoretical $B(E\lambda\uparrow)$ values for ground state ^{18}F Coulomb excitations	68
4.4	Excited ^{18}F nuclear states containing probable E2 transition channels to the $^{18}\text{F}^m$ state	70
4.5	Experimentally determined upper-level limits for the measured transition strengths $B(E2\uparrow)$ of $^{18}\text{F}^m$ Coulomb excitations	71
5.1	Calculated NSCL large-angle γ -array detection efficiencies for $^{18}\text{F}^m$ isomeric decay photons.....	84
5.2	Experimental data collected on the number of observed 184 keV-938 keV isomeric coincidences for each 88 ps timing segment.....	87
D.1	Photons used to determine detector energy, efficiency, and position calibrations for the NSCL NaI(Tl) large-angle detector array.....	101
D.2	Photons used to determine detector energy and efficiency calibrations for the two HPGe detectors used to monitor beam purity	102

LIST OF FIGURES

Figure

1.1	A chart of isotopes	2
1.2	Low-level nuclear states of ^{209}Bi	6
1.3	Nuclear level schemes for ^{238}U and ^{114}Cd	10
1.4	Classical picture of projectile trajectory during Coulomb excitation.	11
1.5	General nuclear level scheme displaying the distinction between the representation of two types [B(E2 \downarrow) and B(E2 \uparrow)] of reduced transition probabilities.....	12
1.6	Examples of well-studied nuclear isomers	15
2.1	A1200 fragment separator.....	22
2.2	Experimental Apparatus for Particle Detection, Identification, and on-line secondary beam purity monitoring during intermediate-energy Coulomb excitation.....	24
2.3	The energy loss (ΔE) in the fast-plastic face of the zero-degree detector (ZDD) versus the time-of-flight.....	25
2.4	Photograph of the NSCL position sensitive NaI Array	27
2.5	Schematic view of the mechanical setup of the NSCL large-angle array.....	28
2.6	The NSCL large-angle γ -array, with a significant portion of the low-background lead shielding in place.....	28
2.7	Typical position calibration spectrum for one detector	31
2.8	Calibrated position versus calibrated energy for one of the eleven inner ring NaI(Tl) detectors in the NSCL large-angle γ -array	31
2.9	Typical photopeak γ -ray energy calibration for one detector and position slice using the ^{88}Y and ^{228}Th calibration sources	33

2.10	Photopeak efficiency for a typical NaI(Tl) detector from the NSCL large-angle γ -array.....	36
2.11	Efficiency for a typical inner ring NaI(Tl) detector divided into ten position slices.....	38
2.12	Typical HPGe detector spectrum gated in software by the ^{18}F particle identification in the DE v. TOF spectrum.....	39
3.1	A simplified level scheme for ^{197}Au	42
3.2	Raw [a] and Doppler-corrected [b] spectra for the Coulomb excitation of the ^{197}Au excitation target.....	44
3.3	Particle identification spectrum displaying Energy loss (ΔE) versus Time of Flight for the ^{197}Au Coulomb excitation data.....	46
3.4	A comparison of experimental and deduced reduced transition probabilities $B(E2\uparrow)$ for the $^{7/2^+}$ to $^{3/2^+}$ transition in ^{197}Au	49
3.5	Particle-identification spectrum displaying ΔE versus Time of Flight for the ^{12}C Coulomb excitation data.....	51
3.6	A simplified level scheme for ^{12}C	52
3.7	Raw [a] and Doppler-corrected [b] energy spectrum for the ^{12}C Coulomb excitation data.....	53
4.1	Level Scheme of ^{18}F	59
4.2	Particle-identification spectrum displaying Energy loss (ΔE) versus Time of Flight for the ^{18}F Coulomb excitation data.....	61
4.3	Transit-timing spectrum for the ^{18}F Coulomb excitation experiment.....	62
4.4	Transit timing spectrum for ^{197}Au Coulomb excitation experiment.....	63
4.5	Raw energy [a] and Doppler-corrected [b] energy spectra for the ^{18}F Coulomb excitation data.....	65
4.6	A simplified level scheme for ^{18}F	73
5.1	Low-lying nuclear levels of ^{235}U	76
5.2	Feynman diagrams for three nuclear excitation mechanisms; NEET, laser-assisted NEET and NEEC.....	77
5.3	A simplified nuclear level scheme for ^{178}Hf	81

5.4	A raw-energy spectrum collected under the condition of detecting a 938 keV gamma-ray within a 88 ps time window.....	82
5.5	Observed number of coincidences due to the in-flight decay of isomeric ^{18}F nuclei ($^{18}\text{F}^m$).....	86
C.1	Doppler-shifted γ -ray energies in the laboratory frame for the 973 keV photon as a function of emission angle in the particle frame.....	99

LIST OF APPENDICES

Appendix

A.	Semi-Classical Coulomb Excitation Theory.....	90
B.	Nuclear Transition Matrix Elements for Electric Quadrupole Transitions	95
C.	Doppler Shift Corrections for Photons Emitted from Fast Moving ($\beta \approx 0.3c$) Projectiles.....	98
D.	γ -emission Data for Energy, Efficiency, and Position Calibrations.	101
E.	Manipulation of Experimental Data from Remote Locations.....	103

CHAPTER 1

INTRODUCTION

1.1 Historical Nuclear Science

Experimental nuclear science has been established for several decades. Beginning with the work of Becquerel and Roentgen with the discovery of the x-ray followed by the Curies and the understanding of natural radioactivity, continuing with the theory of Mayer and the nuclear shell model, the discovery of fission and the Manhattan project, nuclear science has shaped not only the scientific world through its discoveries, but also profoundly effects the societies in which we live.

During the first half of the twentieth century, nuclear scientists were concerned primarily with understanding the properties of long-lived (*i.e.* “stable”) nuclei (<300 isotopes) and the relatively few naturally occurring unstable radioisotopes. Rapidly following the interest in the stable nuclei, researchers realized that the vast majority of isotopes did not occur naturally and must be artificially produced. Following this realization, nuclear theorists predicted that approximately 7,000 isotopes could be produced artificially that would not decay via prompt, spontaneous particle emission and therefore had lifetimes several orders of magnitude longer than events on a nuclear time scale (<fs = 10^{-15} s). The experimental investigation of many of the predicted unstable nuclei began in the latter half of the twentieth century with the development of particle accelerators. This research continues to present day with considerable progress [Sin85, Liu96]. The significant progress in the area of experimental nuclear science can be illustrated by Figure 1.1 which displays the table of the presently known isotopes.

The table of isotopes

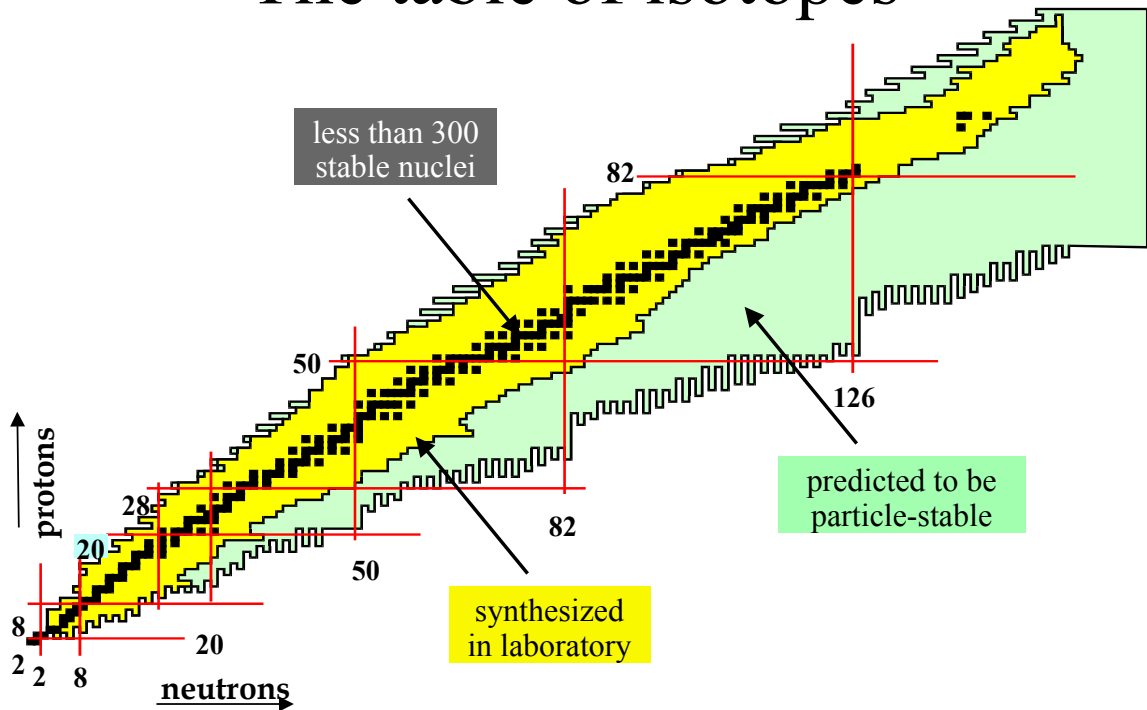


Figure 1.1: A chart of isotopes. The solid squares indicate the stable isotopes, while the light inner area indicates a recently published boundary (February 1997) for experimentally observed radioisotopes. The large darker area indicates the proton and neutron “driplines” according to the predictions of Myers and Swiatecki [Mye66]. The proton and neutron shell closures which possess an unusual particle stability (*i.e.* “magic” numbers) are marked by axial lines.

The solid squares indicate the stable isotopes, while the light inner area indicates a recently published boundary (February 1997) for experimentally observed radioisotopes. The large darker area indicates the proton and neutron driplines (theoretical boundaries for particle-stable nuclei) according to the predictions of Myers and Swiatecki [Mye66]. The proton and neutron shell closures, which possess an unusual particle stability (*i.e.* "magic" numbers), are marked by axial lines. The information uncovered through the process of examining the large number of radioisotopes has given scientists the opportunity to refine our understanding of the atomic nucleus and its role in a wide variety of nuclear processes from astrophysics to nuclear medicine.

1.2 The Atomic Nucleus

The atomic nucleus can be visualized as a many-body system consisting of neutrons and protons which interact mainly via the strong nuclear interaction. These nucleons are spin- $\frac{1}{2}$ particles and obey Fermi-Dirac statistics. Due to the strong, short-range ($\sim 10^{-15}$ m) interaction between nucleons, the many-body nature, and the small physical size of typical atomic nuclei [on the order of 10 fm ($= 10^{-14}$ m)], the structure of the nucleus is very complicated and difficult to model. To further complicate the nuclear system, nucleons typically travel at speeds on the order of $\beta = 0.2c - 0.3c^1$, leading to nucleon de-Broglie wavelengths of

$$\lambda = \frac{2\pi\hbar}{mv} \approx 4.5 \text{ fm} \quad (1-1)$$

where \hbar is equal to Planck's constant divided by 2π . These nucleon wavelengths are on the order of the physical nuclear size leading one to require a relativistic quantum mechanical description of the nucleus.

¹ c represents the speed of light; $c = 2.998 \times 10^8$ m/s.

1.3 Nuclear Models

The difficulty in modeling the nucleus leads us, as with most quantum mechanical descriptions, to the Schrödinger equation:

$$H\Psi = E\Psi. \quad (1-2)$$

In order to accurately describe the nucleus theoretically, one must incorporate a Hamiltonian that correctly predicts the characteristics of the nucleus. Unfortunately, even with an accurate Hamiltonian, there are exact Schrödinger solutions for only the lightest of nuclei. Therefore, in order to experimentally probe certain aspects of the nucleus, various nuclear phenomenological models have been introduced. A broad range of nuclear models exist with some models being transparent and computationally convenient, while others offer a more detailed look at the structure of a many-body nuclear system. These models can be divided into two groups based on the coordinate system they select to describe the nucleus.

One group (microscopic models) describes the nucleus using familiar coordinates to describe the bodies within the nucleus (*i.e.* nucleon position \mathbf{r} , the spin \mathbf{s} , and the isospin $\boldsymbol{\tau}$) which in turn uniquely identifies nuclear states:

$$\Psi = \Psi(r_1, s_1, \tau_1, r_2, \dots) \quad (1-3)$$

For this group of models, the Hamiltonian can be defined:

$$H = \sum_{i=1}^A \frac{p_i^2}{2m} + \frac{1}{2} \sum_{i,j} v(i, j) + \frac{1}{6} \sum_{i,j,k} v(i, j, k) + \dots \quad (1-4)$$

and is summed over all nucleons.

The other group of nuclear models uses macroscopic shape coordinates and are called collective models. These models describe the nucleus using the degrees of freedom of the nucleons collectively (*i.e.* center of mass R , and nuclear quadrupole moment Q):

$$R = \frac{1}{A} \sum_{i=1}^A r_i \quad Q_t = \sum_{i=1}^A r_i^2 Y_t(\Omega_i) \quad (1-5)$$

Both the microscopic model and the macroscopic collective model will be described in the following sections.

1.3.1 The Nuclear Shell Model

The nuclear shell model continues to be the most widely accepted and most popular of the nuclear models. The development of the nuclear shell model by Mayer and Jensen [May48] was motivated by the experimental observation of the extraordinary stability possessed by nuclei with specific numbers of neutrons and protons. It was observed that nuclei containing protons or neutrons matching the values of 2, 8, 20, 28, 50, 82, or 126 exhibited an unusual stability. These exceptional values, called “magic numbers”, were analogous to the shell structure that exists for atomic electrons, and give rise to the special stability of the filled electron shells associated with the Noble gases (He, Ne, Ar, etc.). Mayer and Jensen separately developed a model which included a spin-orbit interaction that not only accounts for the stability of “magic number” nuclei, but also accounts for discontinuities in other physical nuclear quantities (*e.g.* binding energies, first-excited state energies, reaction cross-sections) that occur in the vicinity of closed nuclear shells. The shell model assumes that all nucleons in the nucleus move independently of each other in the collective nuclear potential produced by all other nucleons. This allows the model to produce an external mean field from the vast number of interactions between the various nucleons.

The power of the nuclear shell model in explaining many of the properties of nuclei can be displayed using the case of ^{209}Bi . Figure 1.2 shows some of the excited nuclear states of ^{209}Bi [Sat 90]. Basic shell model theory predicts that this nucleus consists of a ^{208}Pb core (containing “magic numbers” of protons (80) and neutrons (128)), which creates a mean nuclear field, plus one proton in the $h_{9/2}$ shell. In this case, the shell model correctly predicts the spin and parity of the ^{209}Bi ground state as $J^\pi = 9/2^-$. A

number of the ^{209}Bi excited-state spins, parities, and energies presented in Figure 1.2 can be explained simply by promoting the lone $h_{9/2}$ proton into higher and higher orbits.

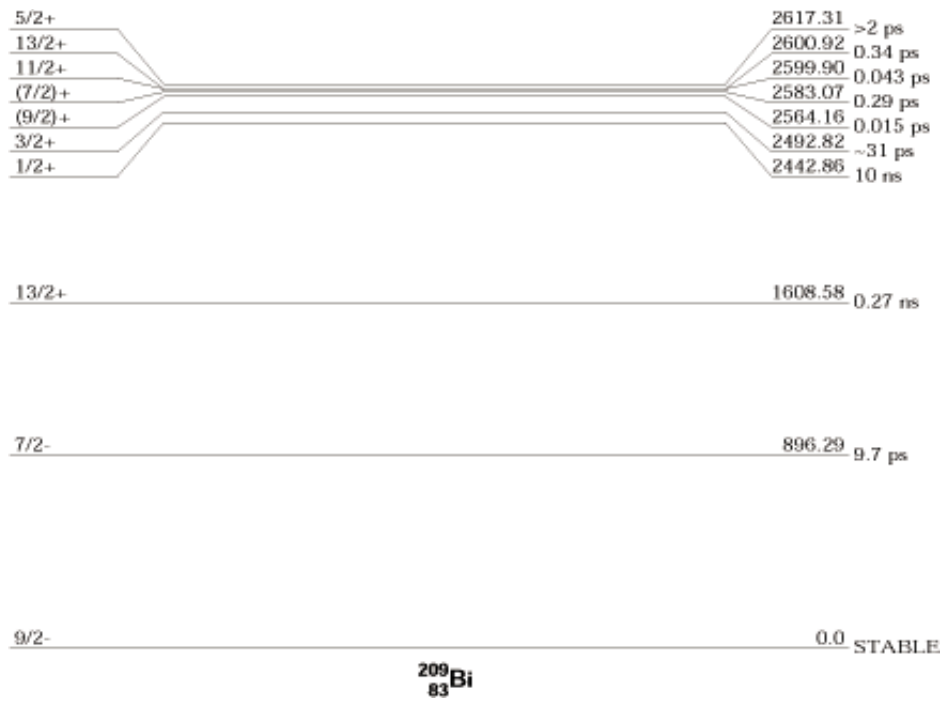


Figure 1.2: Low-level nuclear states of ^{209}Bi .

The shell model has difficulty with larger model spaces, however, when examining the group of levels in Figure 1.2 tightly bunched around an excitation energy of 2.6 MeV. The first excited state in ^{208}Pb is a $J^\pi = 3^-$ state having an excitation energy of 2.6 MeV. The states in ^{209}Bi at 2.6 MeV correspond to an excitation in the ^{208}Pb core *coupled* to the lone $h_{9/2}$ proton, giving the excited states approximate energies of 2.6 MeV, positive parities and spins ranging from $3/2$ to $15/2$ (*i.e.* $3^- \otimes 9/2^- = 6/2 \otimes 9/2 = 3/2, \dots, 15/2$). In order to explain these states using a microscopic model such as the shell model, the nucleons in the Pb nucleus would have to be coupled to the lone proton in order to arrive at the proper wavefunction for these states. In order to more easily describe coupling such as the 2.6 MeV excited states in ^{209}Bi , specific collective excitation models can be used.

1.3.2 Collective Excitation Models

As described in section 1.3.1, most features of nuclei in the vicinity of magic numbers can be described quite easily with microscopic models such as the nuclear shell model. However, as one begins to stray from the areas of nuclear stability, the predictions of the nuclear shell model begin to diverge from experimental data. In order to more accurately predict properties of nuclei in the mid-shell regions, collective excitation models have been used. The rationale of collective modeling is based on the idea that *all* nucleons are involved in excitations, which contrasts with the simple shell model where one nucleon is responsible for an excitation. The best example of a collective excitation is a giant resonance, which can be modeled as a coherent oscillation of many nucleons.

Several other excitations in mid-shell nuclei can also be understood using the collective excitation model. In many mid-shell nuclei, there are low-energy excited states (too low in energy to be considered single particle excited states as in section 1.3.1) with

excitation matrix elements having relatively large values. These large values exclude the possibility of a single nucleon excitation giving rise to this transition. Thus, low-energy excitations in mid-shell nuclei are said to be features of highly-collective nuclei, arising when two or more nucleons participate in a collective motion. One might predict the collective character of a nucleus simply by the energy spacing between levels. By examining neighboring nuclei with similar first excited state energies, one is tempted to predict similar collective character for the two nuclei, but this may not be the case. The most direct method for experimentally determining the collective nature of a nucleus is to measure the reduced transition probability $B(\pi\lambda)$ of a transition between two states in the nucleus. Here, π represents the parity of the transition, and λ denotes the multipolarity of the excitation. The $B(\pi\lambda)$ value for a particular transition from an initial nuclear state i to a final nuclear state f is proportional to the square of the absolute value of the reduced transition matrix element between states i and f :

$$B(\pi\lambda) \propto \left| \langle f \| M(\pi\lambda) \| i \rangle \right|^2 \quad (1-6)$$

Values for the reduced transition probability can be calculated from lifetimes of nuclear excited states typically collected in nuclear experiments, or from direct measurements of excitation cross sections. Equation 1.6 depends directly on the wavefunctions of the nuclear states involved in the transition, making the $B(\pi\lambda)$ value an excellent indicator of collective behavior.

Two primary mechanisms lead to low-energy collective states in mid-shell nuclei: vibration of the nuclear surface and rotational motion of a spatially deformed nucleus. Two excellent examples of collective even-even nuclei are displayed in Figure 1.3. The level energies for ^{238}U follow a distinctive $J(J+1)$ pattern and the spins are spaced with $\Delta J = 2$ (*i.e.* $0^+, 2^+, 4^+, 6^+, \dots$). This level scheme is typical for a rigidly-deformed rotating nucleus. In contrast, the level scheme of ^{114}Cd exhibits a completely different nuclear

structure. In the case of ^{114}Cd , a single 2^+ state is observed at 0.56 MeV with a set of five states ($J^\pi = 0^+, 2^+, 4^+$) around 1.2 MeV. This coupling of states is representative of a nuclear surface vibration. The initial excited state ($J^\pi = 2^+$) is due to a one-photon transition carrying 2 units of angular momentum and having positive parity. Two phonons (corresponding to the second harmonic vibration) can then couple to 0^+ , 2^+ and 4^+ (*i.e.* $2^+ \otimes 2^+$) as the phonons obey Bose-Einstein statistics (in our particular study of $^{18}\text{F}^m$ we will be focusing on transitions occurring in rotating nuclei due to the suspected deformed nature of the $^{18}\text{F}^m$ nucleus).

Nuclear transitions occurring in rotating deformed nuclei are dominated by electric quadrupole (E2) transitions due to angular momentum and parity selection rules. By relating the E2 transition operator to the quadrupole moment operator, one can show that the $B(E2)$ value for a transition is directly related to the *intrinsic* quadrupole moment [Boh98] Q_0 of the nucleus.

$$B(E2) \propto Q_0^2 \quad (1-7)$$

The proportionality factor depends on the angular momentum J of the initial state, and on the quantum number K characterizing the orientation of the deformed nucleus with respect to the symmetry axis.

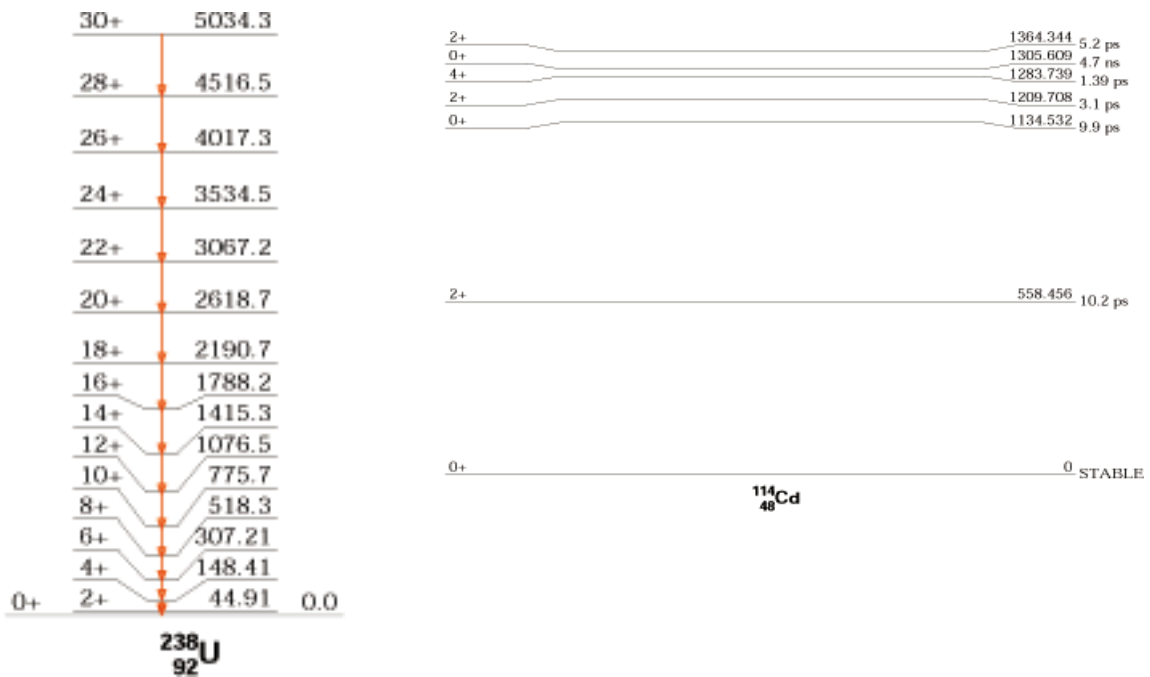


Figure 1.3: Nuclear level schemes for ^{238}U and ^{114}Cd .

1.4 Experimental Probes of Nuclear Structure

As briefly noted in section 1.3.2, the nucleus can be either studied passively (through the observation of decay radiation), or directly by studying the electronic environment of the nucleus through the collection of nuclear structure via its excitation spectrum. The most fruitful approach, and the one applied here, is to apply an external field to the nucleus and subsequently study the reaction of the nucleus to the field. This can generally be done by directing a beam of particles onto a target and observing the reaction products (nuclei, neutrons, electrons, γ rays, etc.). A variety of external fields can be produced by varying the target nuclei, the projectile nuclei, and the projectile energy. This will result in a wide range of experimental environments that can be utilized

to probe the nucleus of interest. The most informative probes are the methods that tend to limit the physical disturbance of the nucleus of interest while producing a relatively large reaction cross section and hence nuclear excitation probability.

1.4.2 Coulomb Excitation as an Experimental Probe

The electromagnetic interaction is a well-known and extremely useful experimental probe. Current forms of the electromagnetic probe range from nuclear magnetic resonance (NMR), used to deduce molecular structure, to electron scattering experiments, used to map the charge distribution of nuclei. Another useful form of the electromagnetic probe is Coulomb excitation, where a nucleus of interest is excited by the Coulomb field of another nucleus (see Figure 1.4). The excited nucleus subsequently de-excites, typically through photon emission, revealing information on the energy and structure of the excited state. The cross section for a Coulomb excitation reaction is directly related to the nuclear transition matrix element connecting the levels involved in the excitation as well as the nuclear charges (Z_p and Z_t).

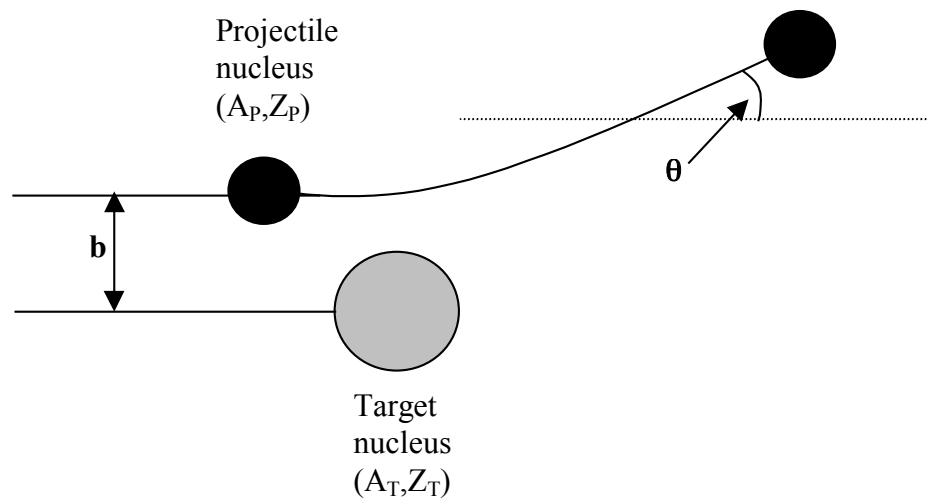


Figure 1.4: Classical picture of the projectile trajectory. The projectile nucleus can be Coulomb excited due to the time-dependent tidal forces exerted by the electric field of the target nucleus (similarly, the target nucleus can be excited by the electric field of the projectile).

One needs to specify the technique used to populate the excited nuclear state in order to uniquely identify the direction of a measured reduced transition probability $B(\pi\lambda)$. In typical radioactive decay experiments, excited states of nuclei are passively populated through a process of particle absorption or emission [electron capture (EC) or β^- respectively], followed by a cascade of de-excitation photons (see Figure 1.5). With this population method, one can identify a particular transition in question, measure the mean-lifetime of the de-excitation photons due to the transition, and calculate a “down” reduced transition probability $B(E2\downarrow)$. In the case of a direct population of an excited nuclear state using a Coulomb excitation technique (see section 1.4.1), the ground state of a nucleus is first collectively promoted to a specific nuclear excited state and the latter is then allowed to de-excite through photon emission (see Figure 1.5). One can arrive at a value for the “up” reduced transition probability $B(E2\uparrow)$ by measuring the photon yield, and determining an excitation cross section.

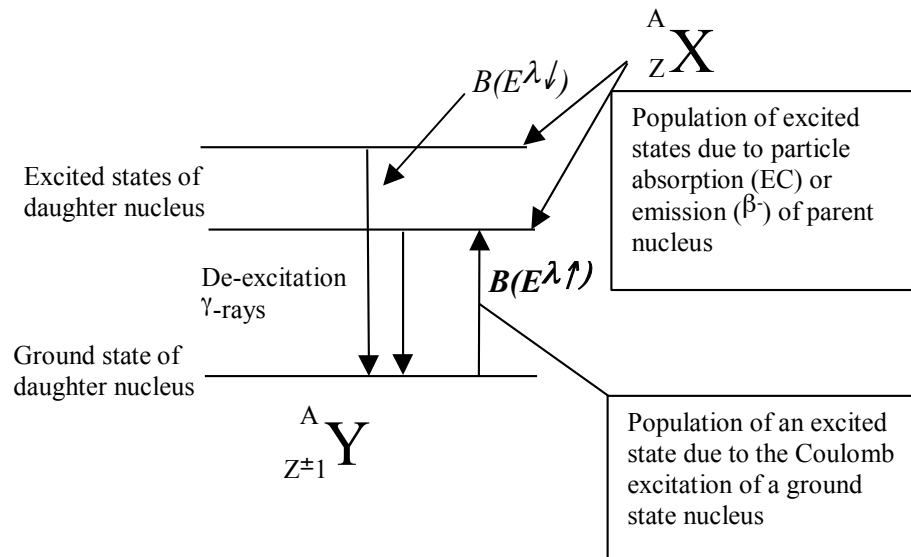


Figure 1.5: General nuclear level scheme displaying the distinction between the representation of two types [$B(E2\downarrow)$ and $B(E2\uparrow)$] of reduced transition probabilities.

The experimental distinction between the two representations of reduced transition probabilities is important because the experimentally measured $B(E2\downarrow)$ and $B(E2\uparrow)$ values for the same nuclear transition are related:

$$B(E2; I_i \rightarrow I_f) = \left(\frac{2I_f + 1}{2I_i + 1} \right) B(E2; I_f \rightarrow I_i) \quad (1-8)$$

In the case of the $B(E2\downarrow)$, the excited nuclear state is populated from higher excited states through various electromagnetic transitions (*i.e.* E2, M1, etc.) with a wide range of transition probabilities and branching ratios. This leads to an ambiguity in the population of the excited state prior to the emission of the de-excitation photon which in turn leads to uncertainties in determining the value of the down reduced transition probability $B(E2\downarrow)$. This population uncertainty is greatly reduced when the excited state is directly populated through the same electromagnetic channel that will be measured by the de-excitation photon. One can “exactly” measure this population by determining the “up” reduced transition probability $B(E2\uparrow)$. Coulomb excitation, while being able to measure both $B(E2\downarrow)$ and $B(E2\uparrow)$ values, allows one to uniquely populate an excited nuclear state using the electromagnetic channel of interest, making the up reduced transition probability $B(E2\uparrow)$ a more direct measure of the transition probability and a clearer interpretation of the collective behavior of the excited state. Decay methods must correct however, for the admixtures of various decay types (M1/E2, etc).

1.5 Nuclear Isomeric Excited States

A chemist would define an isomer as a substance having the same molecular formula as another substance but exhibiting a different geometrical structure. A nuclear analog to this chemist’s term was adopted by a British nuclear chemist Frederick Soddy to describe relatively long-lived nuclear states with nuclear properties distinct from other states formed by the same nucleus.

The lifetime (or stability) of a nuclear state depends primarily on two parameters; the relative energy of the excited state and the transition probabilities of the excited state with lower-energy states in the same nucleus via photon emission or with states in neighboring nuclei via particle emission. Typical non-isomer nuclear excited-state lifetimes range from several femtoseconds (10^{-15} s) up to several picoseconds (10^{-12} s). There are certain nucleon combinations however, that lead to relatively long-lived excited states (as compared to typical nuclear lifetimes) in atomic nuclei. Nuclei containing an odd number of protons and an odd number of neutrons tend to exhibit low-energy isomeric states with a relatively high spin. The lifetimes of odd-odd nuclei isomeric states can vary by several orders of magnitude. Examples of well-studied isomeric states are displayed in Figure 1.6: the 75 keV ($J^\pi = 9^-$) isomeric state of ^{180}Ta with a half-life of 10^{15} years, the 2447 keV ($J^\pi = 16^+$) ^{178}Hf isomer ($T_{1/2} = 31$ y), and the 2921 keV ($J^\pi = 18^+$) isomer in ^{212}Po ($T_{1/2} = 45$ s) [Dra98].

Two basic properties of nuclei are their level structure and the transition matrix elements by which these levels are joined. This information is directly related to the shape of the nucleus. Nuclei that are deformed have small excitation energies and larger coupling strengths whereas spherical nuclei typically exhibit large excitation energies and small coupling strengths (see Chapter 3). As indicated earlier, a large coupling strength indicates collective motion, since a single particle can not give rise to large transition matrix elements.

Intermediate-energy Coulomb excitation experiments using radioactive beams have been shown to be feasible and powerful tools in the study of nuclear structure of radioactive nuclei. Recently, such experiments have defined a new region of deformation, and its boundaries, by measurement of 2^+_1 energies and $B(E2\uparrow)$ values in radioactive beam nuclei of Si, S, and Ar around mass 40 [Sch96]. We use the intermediate-energy Coulomb excitation technique and the NSCL large solid-angle

NaI(Tl) array to study another class of radioactive nuclei, namely, those in isomeric states.

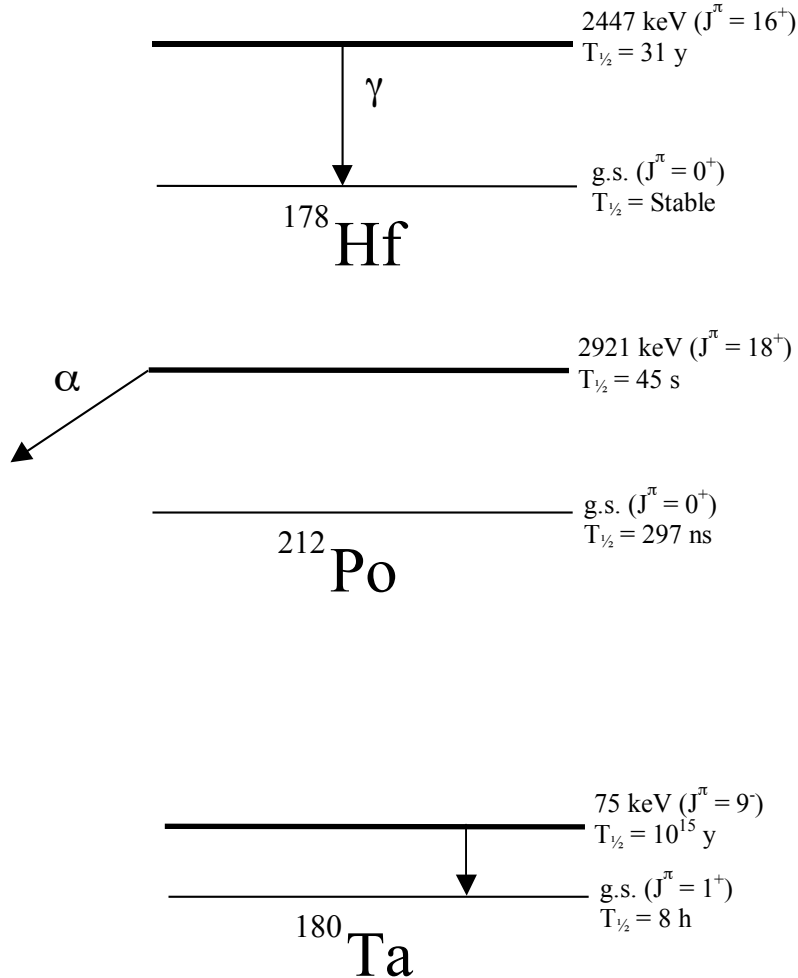


Figure 1.6: Examples of well-studied nuclear isomers.

Heavy elements ($Z > 20$) are produced in astrophysical events such as nova and supernova through a process of rapid-neutron capture (r-process). The pathway of this process proceeds through several isomeric states which act as “waitpoints” or bottlenecks to the production of heavy elements. In order to model these complex astrophysical processes, the characteristics of nuclear isomeric states must be understood. The nucleus of ^{18}F , while not directly involved in the r-process, serves as an excellent analog for

study. The nucleus of the unstable ^{18}F isotope has been the subject of discussion and research because of the unusual properties of its 1.1 MeV ($T_{1/2} = 163$ nsec) isomeric state. The configuration of the isomeric state has been described as a “deuteron” orbiting a core consisting of ^{16}O [Bro95]. This unusual configuration suggests a deformed $^{18}\text{F}^m$ nuclei and would lead one to expect a collective structure built on the isomeric state. In the present work, the unstable nucleus ^{18}F has been studied via intermediate-energy Coulomb excitation in an attempt to populate collective states above the short-lived 1.1 MeV ($J^\pi = 5^+$) isomeric ($T_{1/2} = 163$ ns) state. An introduction to the experimental technique and apparatus is given in Chapter 2. Results of an experiment measuring the intermediate-energy Coulomb excitation of ^{197}Au and ^{12}C , used to test the capabilities of the experimental apparatus, are presented in Chapter 3. Chapter 4 describes the intermediate-energy Coulomb excitation of $^{18}\text{F}_{\text{g.s.}}$ and $^{18}\text{F}^m$ and presents the results of our measurements. Chapter 5 outlines proposed future work based on the results of our findings.

CHAPTER 2

EXPERIMENTAL SETUP AND DETECTOR CALIBRATION

2.1 Motivation and Introduction

Coulomb excitation is a well known and powerful tool used to study nuclei [Sch96, Ibb98]. If the charge distributions of two colliding nuclei do not overlap during the collision process, the measured Coulomb excitation cross sections are directly linked to the electromagnetic matrix elements that characterize the electromagnetic excitation of specific nuclear states. Therefore, Coulomb excitation can provide information on the electromagnetic transition strength, hence, on the nuclear collectivity and deformation of a nucleus. In the past, Coulomb excitation has been used to study low-lying nuclear states by bombarding stable targets with light and heavy ions at bombarding energies well below the reaction Coulomb barrier. This ensures that Coulomb excitation is the only possible excitation process available to the nuclei. Work was restricted to stable nuclei until the advent of radioactive-beam particle accelerators.

Particle accelerators, coupled with recent improvements in the area of fragment (mass) separation devices have allowed for the production of intense beams of short-lived radioactive nuclei [Bec90, Yen92]. These advancements have made it possible to use the process of Coulomb excitation to study short-lived nuclei adjacent to the valley of stability. Currently, three different nuclear processes are used at particle accelerator facilities to produce a wide range of scientifically interesting radioactive fragments. The Isotope Separator On-Line (ISOL) technique, with subsequent acceleration of the secondary beams to energies below the Coulomb barrier, allow studies similar to those used for stable beams. One disadvantage of this technique is that only nuclei with rather

long half-lives ($>ms$) are accessible due to the time it takes to separate and (re-) accelerate the fragments.

One may also make radioactive ions by fragmenting the beam projectile. Projectile fragmentation enables one to perform experiments with radioactive nuclei that have a much shorter half-life. By limiting the distance from the production target to the experimental area, one can conduct experiments on nuclei with half-lives on the order of tens of nanoseconds (with a speed of $\beta = 0.3$, particles are typically moving at ~ 3 cm/ns). The secondary beams produced in projectile fragmentation reactions are typically very high energy, forward focused, fully ionized, and travel with virtually the same velocity as the incident (primary) beam. These advantages make projectile fragmentation a good choice for producing a radioactive ion beam of virtually any element. However, the beam often includes unwanted fragments as well as the desired beam. The ability to produce a wide range of secondary beams allows one to conduct experiments with secondary radioactive beams which mimic similar experiments with stable beams. This new area of experimental nuclear physics is only presently hindered by the relatively low secondary beam intensities produced using the process of particle fragmentation, typically $<10^6/s$. Also, the fact that secondary radioactive beams produced with the fragmentation method are at high incident beam energies is not always advantageous. With some exceptions [Kol98, Dey98], most astrophysical nuclear reactions producing heavy nuclei occur at energies well below the energies reached by particle fragmentation, making ISOL facilities potentially better equipped to model this type of reaction, at least for long-lived nuclei ($t_{1/2} > ms$).

In order to produce and react secondary beams with a relatively low-energy and with half-lives of the order of nanoseconds, one can employ a nucleon transfer reaction. These low- to intermediate-energy reactions produce a transfer of nucleons from the target nucleus to the projectile nucleus (or vice versa). The products of transfer reactions typically travel at a small fraction of the speed of light ($0.05 c - 0.3 c$). The advantages of

this type of nuclear reaction include a relatively low reaction energy, particle selectivity, and increased post-reaction particle stability which make transfer reactions useful for studying short-lived nuclei in the vicinity of stable isotopes. Details on these and other methods of radioactive beam production are published in [Gei95].

2.2 Experimental Apparatus and Setup

In the following sections the experimental method used to produce the secondary ^{18}F ion beam, the experimental setup for the subsequent Coulomb excitation measurements, including the position-sensitive NaI γ -array, and the detector calibration process will be presented. Details will be given on how the position, energy, and efficiency calibrations of the NaI array were performed for the detection of fragments moving at a fraction of the speed of light.

2.2.1 The A1200 Fragment Separator

A 45 MeV/nucleon ^{17}O beam produced by the K1200 cyclotron at the National Superconducting Cyclotron Laboratory (NSCL) at Michigan State University irradiated a ^{12}C target located at the Dispersive Image 2 position of the A1200 fragment separator, shown in Figure 1 [She91]. The unusual placement of the production target at Dispersive Image 2 was required in order to minimize the distance from the ^{18}F production target to the excitation target. The time-of flight of each particle was measured on an event-by-event basis over the approximately 30 m flight path between the thin fast plastic scintillator (0.01" = 0.254 mm, BC404), located at the Final Achromatic Image at the exit of the A1200, and the zero-degree detector (fast-slow phoswich detector) located at the

end of the NaI array. A schematic layout of the NSCL A1200 fragment separator is shown in Figure 2.1.

A secondary beam of ~ 30 MeV/u ^{18}F ions was selectively produced using the $^{12}\text{C}(^{17}\text{O}, ^{18}\text{F})^{11}\text{B}$ neutron-transfer reaction. This transfer reaction produces a copious amount of the high-spin, stretched (5^+) ^{18}F isomeric state ($^{18}\text{F}^m$) with high yield in the forward direction [Bro95, Rob95]. The use of thin (~ 10 mg/cm²) production targets optimized the production of the secondary beam in its isomeric state, but also limited the secondary beam intensity. Alternatively, a relatively thick (~ 50 mg/cm²) production target was also used to gain a order of magnitude increase in the secondary beam production, but the ratio of secondary beam produced in the isomeric state versus beam particles populating the low-spin ^{18}F ground state was found to be smaller by about 20%. In order to quantify the effect of primary target thickness on the production rate of high-spin ^{18}F isomer, data were acquired for approximately 24 h using each production target.

The magnetic rigidity of the first half of the A1200 fragment separator was set to a value of $B_p = 2.0767$ T·m, to transport the ^{17}O ion beam from the K1200 cyclotron to the primary (46 mg/cm²) ^{12}C target located at the Dispersive Image 2 position of the A1200. The energy spread of the primary beam was limited to $\pm 0.4\%$ by using a pair of momentum-limiting slits located at Dispersive Image 1 of the separator. The second pair of focusing magnets located downstream of the primary target were tuned to maximize the throughput of ^{18}F ions populating the high-spin (5^+) isomeric state. The isomer population was by monitored by measuring the yield of γ -rays de-populating the isomer using a pair of HPGe γ -ray detectors located near the zero-degree detector (see Figure 2.2). Magnet settings were varied around the calculated magnetic rigidity value ($B_p = 1.8291$ T·m) for the throughput of ions with a mass to charge ratio of 2. The magnet settings were changed in small increments for the thick target runs, from $B_p = 1.8113$ T·m to $B_p = 1.8438$ T·m in order to maximize the throughput of isomeric $^{18}\text{F}^m$ (see Table 2.1). A magnetic rigidity value of $B_p = 1.8275$ T·m was subsequently used for the thick target

runs. At this rigidity setting, ^{18}F was the major beam component at 64%, with 16% of that fraction being $^{18}F^m$, for a total $^{18}F^m$ beam fraction of :

$$0.64 * 0.16 = 0.102, \quad \mathbf{10.2\%} \text{ } ^{18}F^m \text{ of total beam}$$

A similar process was used for the thin (8.9 mg/cm^2) production target runs. The magnet settings for the thin target data acquisition were varied from $B_p = 1.8641 \text{ T}\cdot\text{m}$ to $B_p = 1.8748 \text{ T}\cdot\text{m}$ in order to maximize the ratio of isomeric ^{18}F to ground state ^{18}F (see Table 2.2). A magnetic rigidity value of $B_p = 1.8672 \text{ T}\cdot\text{m}$ was then used for the data acquired with the thin production target. At this rigidity setting, ^{18}F was the major beam component at 56% with 20% of that fraction being $^{18}F^m$ for a total $^{18}F^m$ beam fraction of :

$$0.56 * 0.20 = 0.112, \quad \mathbf{11.2\%} \text{ } ^{18}F^m \text{ of total beam}$$

The second half of the A1200 was used to focus the secondary beam fragments. Because there was no energy-loss wedge at Image 2, only one magnetic rigidity slice could be performed. Higher purity can be obtained using the short flight-path UM 7 Tesla Solenoid [Bec90; Bro95], but this device was not available at the time of this experiment.

The experimental apparatus used in the Coulomb excitation experiment is shown in Figure 2.2. The primary beam produced by the K1200 cyclotron passed through one set of x-y position-sensitive parallel-plate gas avalanche-counter (PPAC) detectors [Swa84; Sou92; War95] and was delivered to the primary production target located at Dispersive Image 2. The secondary beam fragments were measured in the A1200 focal plane by using a second set of x-y position sensitive PPAC detectors. The PPAC detectors were primarily used to monitor the relative beam position (resolution $< 2\text{mm}$) and to assure that the beam position did not shift over the course of the experiment. These detectors were also used to track the incoming primary beam particles as well as track the scattered secondary fragments. A fast-slow phoswich scintillator detector placed at the end of the experimental apparatus stopped the secondary beam fragments and was used for energy loss (fast plastic) and total energy (slow plastic) measurements.

We used a cylindrical fast-slow plastic phoswich detector with a 10.2 cm (4") diameter as our

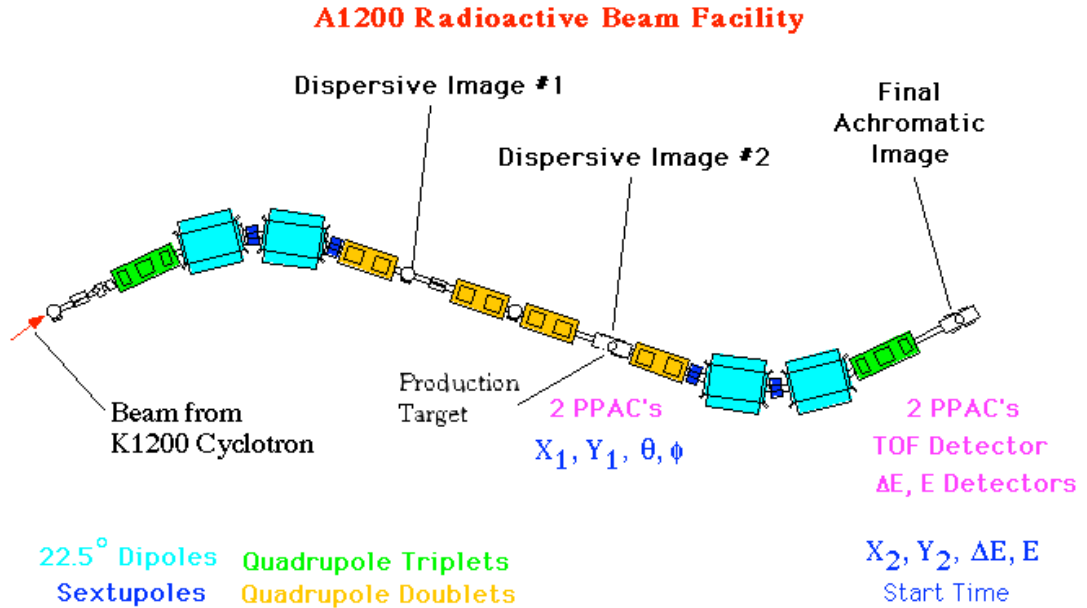


Figure 2.1 A1200 Fragment Separator.

zero-degree detector. The phoswich detector consisted of a 0.6 mm layer of BC400 (fast) plastic attached to the front surface of a 10 cm thick piece of BC444 (slow) plastic. When placed in our experimental apparatus 514.3 mm downstream from the excitation target position, the stopping detector subtended an angle with respect to the excitation target of :

$$\arctan\left(\frac{5.08\text{cm}}{51.44\text{cm}}\right) = 5.64^\circ \quad (2-1)$$

For reference, $\theta_{max} = 5.6^\circ$ in the laboratory frame corresponds to $\theta_{max} = 6.1^\circ$ in the center-of-mass system.

Table 2.1: Data on the optimization of $^{18}F^m$ yield at the face of the Zero Degree Detector by secondary beam-tuning, using the 46 mg/cm^2 thick ^{12}C production target.

<i>B-Rho</i>	<i>Ge counts</i> <i>184 keV γ</i>	<i>Ge counts</i> <i>938 keV γ</i>	<i>184 keV</i> <i>γ-rays</i>	<i>938 keV</i> <i>γ-rays</i>	<i>Total ^{18}F</i> <i>particles</i>	<i>Isomeric</i> <i>Production</i> <i>(%)</i>
1.81130	3	1	82.4	56.8	20479	0.3
1.81483	116	52	3186.8	2954.5	21489	14.3
1.81846	137	62	3763.7	3522.7	24578	14.8
1.82210	157	74	4313.2	4204.5	27115	15.7
1.82575	320	153	8791.2	8693.2	62004	14.1
1.82715	499	220	13708.8	12500.0	80500	16.3
1.82914	42	27	1153.8	1534.1	7523	17.9
1.83097	227	102	6236.3	5795.5	39943	15.1
1.83280	199	70	5467.0	3977.3	29739	15.9
1.83647	161	61	4423.1	3465.9	27183	14.5
1.84015	98	37	2692.3	2102.3	13331	18.0
1.84383	3	2	82.4	113.6	28555	0.3

Table 2.2: Data on the optimization of $^{18}F^m$ yield at the face of the Zero Degree Detector by secondary beam-tuning, using the 8.9 mg/cm^2 thin ^{12}C production target.

<i>B-Rho</i>	<i>Ge counts</i> <i>(938 keV γ)</i>	<i>938 keV</i> <i>γ-rays</i>	<i>Total ^{18}F</i> <i>particles</i>	<i>Total Slit</i> <i>Width (cm)</i>	<i>Isomeric</i> <i>Production</i> <i>(%)</i>
1.86410	413	23465.9	149759	slits= 2.0 cm	15.7
1.86580	232	13181.8	74700	slits = 1.0 cm	17.6
1.86720	727	41306.8	205542	slits= 2.0 cm	20.1
1.86730	244	13863.6	69895	slits = 1.0 cm	19.8
1.86730	279	15852.3	78282	slits = 1.7 cm	20.3
1.86740	316	17954.5	88819	slits = 1.0 cm	20.2
1.86920	228	12954.5	68788	slits = 1.0 cm	18.8
1.87010	248	14090.9	58582	slits = 1.7 cm	24.1
1.87090	236	13409.1	50732	slits = 1.7 cm	26.4
1.87100	179	10170.5	51762	slits = 1.0 cm	19.6
1.87100	253	14375.0	61954	slits= 2.0 cm	23.2
1.87480	0	0.0	0	slits= 2.0 cm	0.0

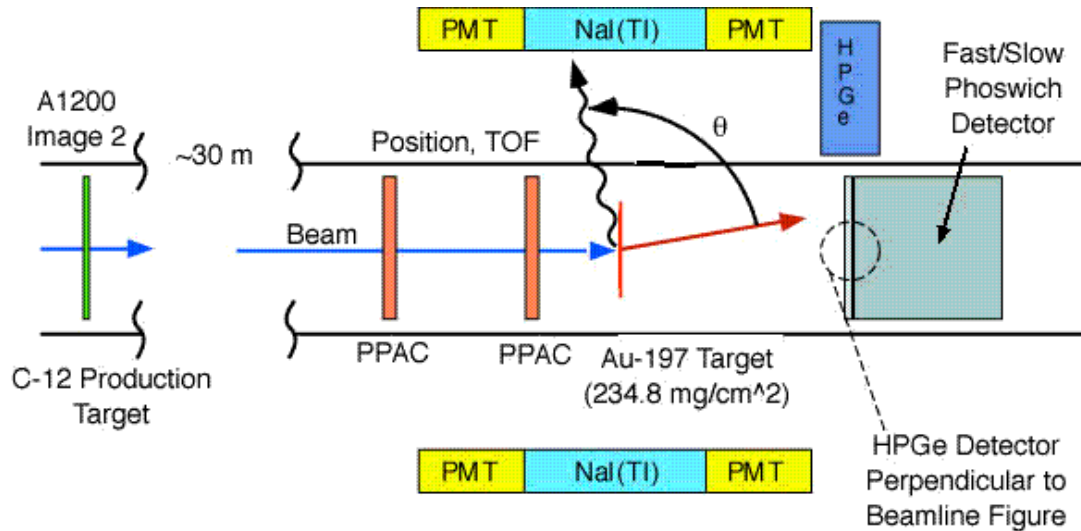


Figure 2.2 Experimental Apparatus for Particle Detection, Identification, and on-line secondary beam purity monitoring during intermediate-energy Coulomb excitation.

The excitation target was fabricated by combining two ^{197}Au foils with respective thicknesses of 184.1 and 50.73 mg/cm^2 giving a total excitation-target thickness of 234.8 mg/cm^2 . The active area of the excitation target was ≈ 4 cm in diameter assuring complete interaction with the secondary beam particles (≈ 1 cm beam spot). The excitation target was placed at the center of the NSCL position-sensitive NaI γ -array, which will be described in the following section. Figure 2.3 displays the energy loss in the fast plastic face of the zero-degree detector (ZDD) versus the time-of-flight calculated using a Time-to-Analog Converter (TAC) to quantify the secondary beam particle flight time from the exit of the A1200 to the ZDD. The separation of the various beam constituents are clear, and the $N=Z$ line clearly identifiable. This combination of parameters allowed for software-based fragment separation and identification.

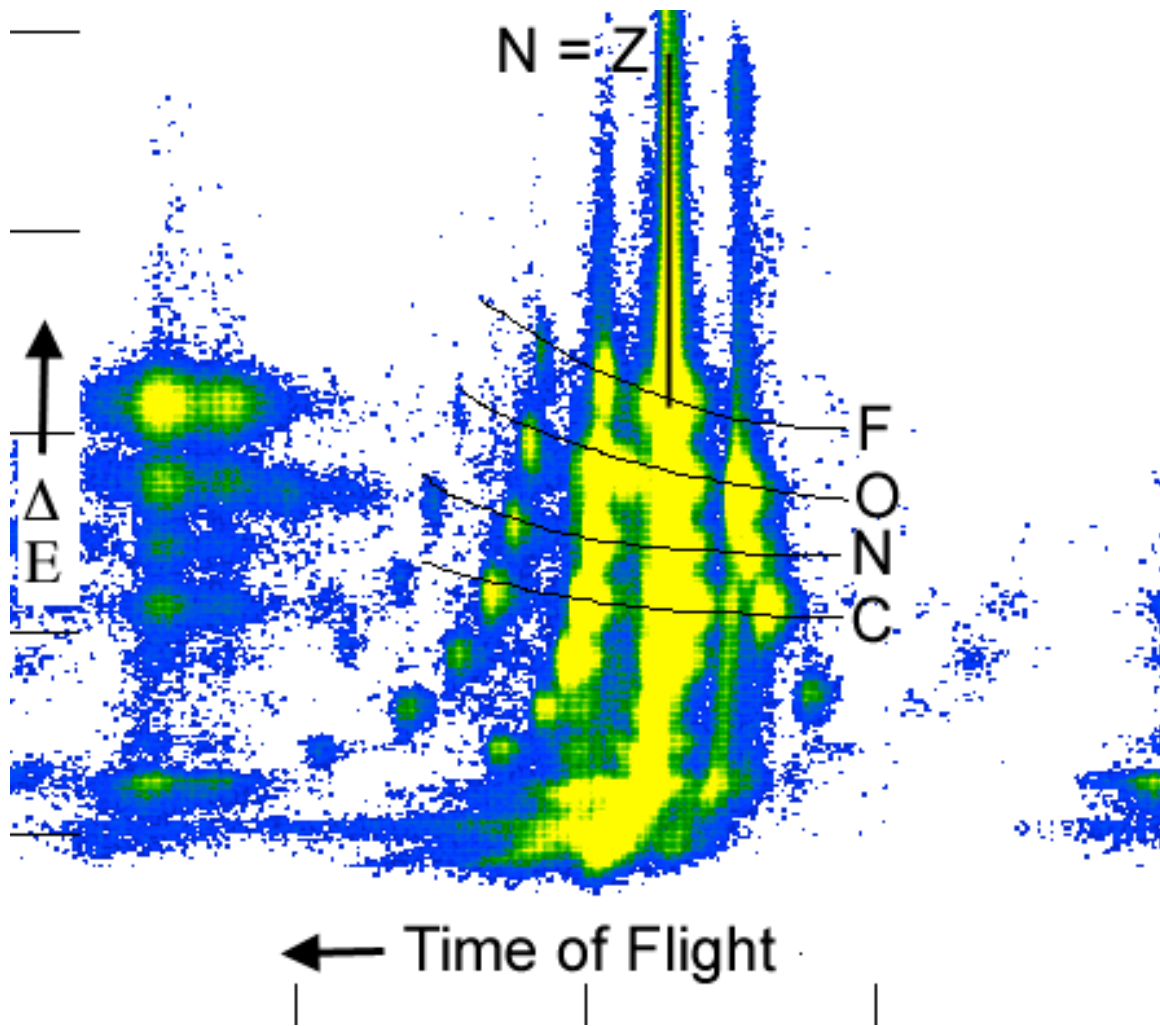


Figure 2.3: The energy loss (ΔE) in the fast-plastic face of the zero-degree detector (ZDD) versus the time-of-flight determined using a Time-to-Analog Converter (TAC) to quantify the secondary beam particle flight time from the exit of the A1200 to the ZDD is displayed. The separation of the various beam constituents can be identified, with the $N=Z$ line clearly shown.

2.2.2 The NSCL position-sensitive NaI γ -detector array

A high-efficiency photon spectrometer is needed to measure the de-excitation γ -rays following intermediate-energy projectile Coulomb excitation of low-intensity radioactive ion beams. The spectrometer is to be used for the analysis of a wide range of radioactive species, thus it must have specific characteristics. Due to the low beam intensities of secondary radioactive beams, the detector array must be highly efficient over a large energy range, as well as cover a large fraction of the 4π solid angle of γ -ray emission. In radioactive beam studies, the photons are usually being emitted from an excited projectile moving at a significant fraction of the speed of light (typically on the order of $\beta = 0.2c - 0.4c$). The high velocity of the excited projectile causes a significant Doppler-shift (see appendix C) in the detected γ -ray energies, and spectral corrections must be applied. When the shift in γ -ray energy due to the speed of the emitting projectile is corrected, the Doppler-shift of the detected photopeak is greatly reduced. As an example, the width of the 4.4 MeV photopeak in the Coulomb excitation of ^{12}C ($\beta = 0.28c$) was approximately 850 keV (20%) without Doppler-correction as opposed to 225 keV (5%) with the proper correction.

The NSCL NaI γ -detector array [Gla97] consists of 38 position sensitive NaI(Tl) detectors arranged in three concentric rings parallel to the beamline. The detectors are from a decommissioned Positron Emission Tomography (PET) machine at Washington University in St. Louis. Each detector is comprised of a NaI(Tl) crystal (5.75 cm dia. x 18 cm length) enclosed in a 0.45 mm aluminum shield, optically joined to a photomultiplier tube on each end of the crystal. The position and energy of a detected photon can be reconstructed from the characteristics of the electrical signals produced by the two photomultiplier tubes. Assuming a coordinate system with the origin at the

center of the crystal and with the x-axis denoting the cylindrical axis of the crystal, the light yield from each photomultiplier ($Y_{1,2}$) is proportional to [Won 90]:

$$Y_{1,2} \propto e^{\pm x} \quad (2-2)$$

The energy and position of the incident photon are consequently given by:

$$Energy \propto \sqrt{Y_1 + Y_2} \quad (2-3)$$

$$Position \propto \log\left(\frac{Y_1}{Y_2}\right) \quad (2-4)$$

To shield against ambient γ -radiation, the entire array is surrounded by a 16.5 cm layer of low-background (pre-WW2) lead. This corresponds to a weight of approximately 6 tons, requiring a significant amount of mechanical support. A photograph of the array without the support structure is presented in Figure 2.4. A schematic drawing of the front and side view of the array and the lead shielding is shown in Figure 2.5. The photograph labeled Figure 2.6 shows the NSCL array with part of the lead shielding in place.

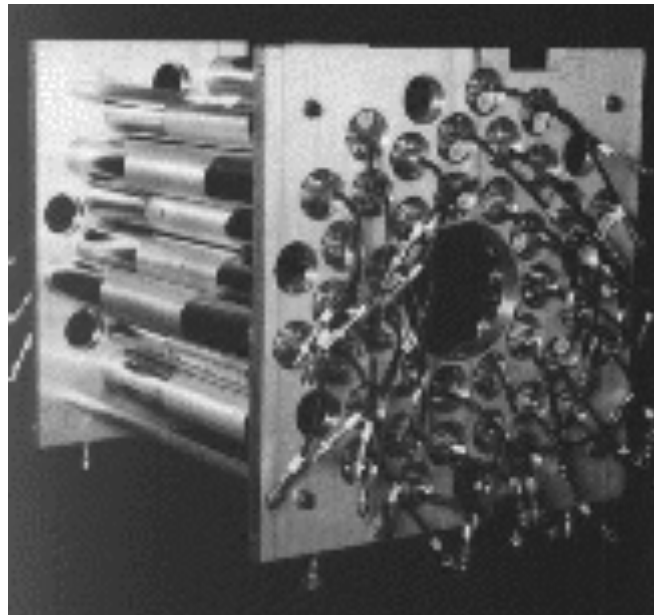


Figure 2.4 Photograph of the NSCL position sensitive NaI Array [Sch 99].

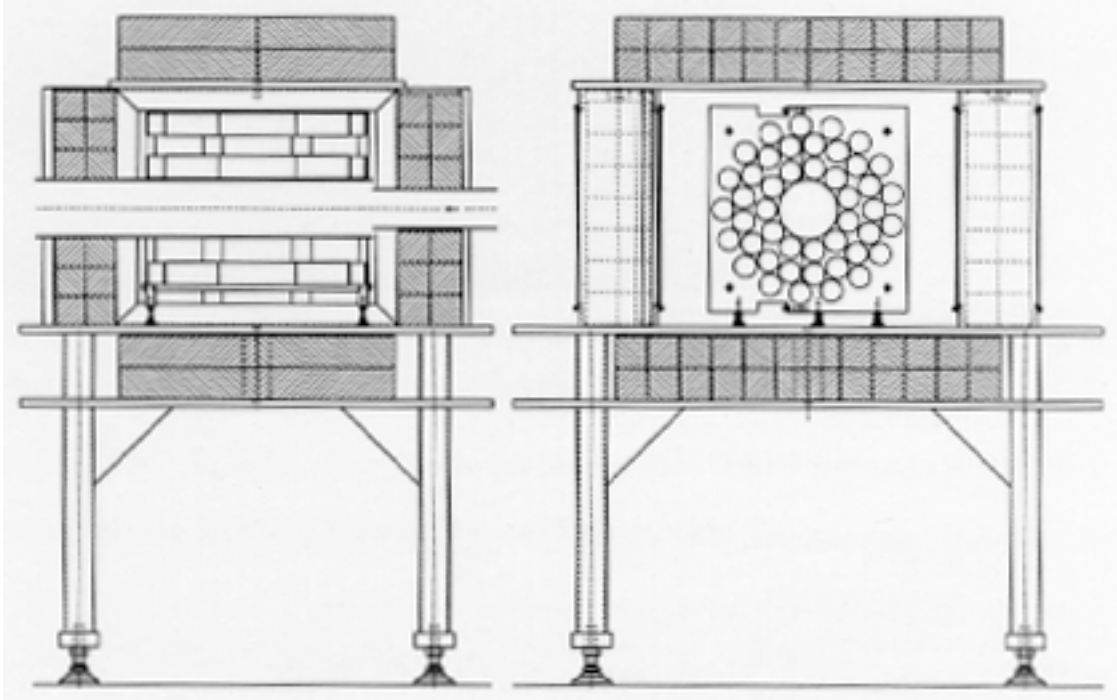


Figure 2.5: Schematic view of the mechanical setup of the NSCL large-angle array. The support structure and the lead shielding (shaded area) can be seen. The target is located in the center of the beampipe. The beam enters from the right in the left-hand picture, and the figure on the right hand side shows the array in the beam direction.

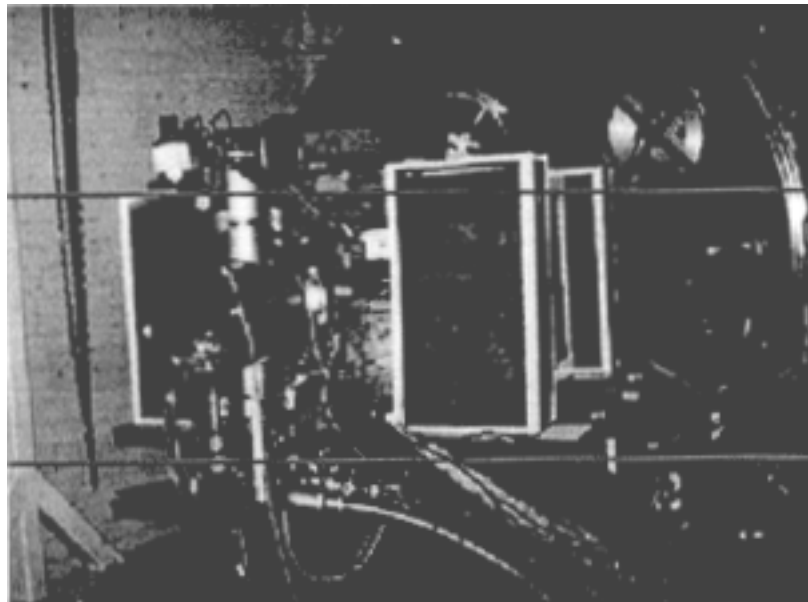


Figure 2.6: The NSCL large-angle γ -array, with a significant portion of the low-background lead shielding in place.

2.2.3 Position Calibration of the NSCL γ -Detector Array

All 38 detectors that form the NSCL array are calibrated before each experiment for energy, position and detection efficiency. The methods used to perform these important calculations will be described in the following sections. The importance of a position calibration (with accuracy on the order of 1-2 cm) and a satisfactory position resolution (≤ 2 cm) is quite clear in view of the Doppler-shift correction that must be performed on the detected photons of interest (see appendix C) and for accurate transit-time measurements (see section 5.4). The deposited energy of a detected photon is converted to light in the scintillating NaI(Tl) crystal and collected by a photomultiplier tube (PMT) connected to each end of the NaI(Tl) crystal. The position of the incident photon is proportional to the logarithm of the ratio of the light collected in each of the PMTs. The pseudo-parameter $Position(i)$ was calculated using the following formula and subsequently recorded for each detector :

$$Position(i) = 2000 + 1000 * \log\left(\frac{i_1}{i_2}\right) \quad (2-5)$$

This calculates a position for each detected photon using a $4k-12$ bit scale (0-4096) that places a photon detected in the center of the crystal into channel 2000, which can be thought of as the ‘center’ of the $4k$ scale. A well-collimated ^{60}Co γ -source was used to illuminate the array in order to correlate the absolute photon detection position to our pseudo parameter $Position(i)$. The isotope ^{60}Co is a well-known and widely-used calibration γ -source primarily because of the emission of two photons at energies of 1173.2 keV and 1332.5 keV from each nuclear decay. These photons can be individually resolved with most NaI(Tl) crystals. The initial position calibration is labor intensive, as each detector had to be calibrated individually. Individual detectors were removed from the array and placed in a low-background lead castle for the calibration to shield the detectors from ambient radiation and to collimate the ^{60}Co source. The γ -rays from the

source reached the detector through a small hole in the lead “castle” and illuminated about 1 cm of the crystal. Each detector had a reference length scale, which ranged from 0 to 20 cm, attached to the aluminum sheath covering the crystal.

Initially, the detector was placed inside the lead castle, so that the center of the crystal (position 10 cm) was illuminated by the source. Care was taken to insure that the signal heights from all PMT’s were approximately equal by matching the amplifier outputs on an oscilloscope. This places the pseudo parameter Position(*i*) around channel number 2000 for the central position (10 cm) of the crystal.

This measurement was repeated eight times for each detector in 2 cm steps, each time the centroids of the calculated position peaks were recorded. The position of the detector inside the cavity was determined by removing the source, and visually inspecting the position of the detector relative to the collimator opening and the length scale on the detector housing. A cubic fit was used to model the calibration data. The results were stored in a table which provided for each detector the relation between the detection position (in centimeters) and the “position” in channel numbers. A typical position calibration – given as position in centimeters versus calculated position in channel numbers – for one detector is shown in Figure 2.7, together with the results from a cubic fit. The vertical error bars represent the width of the fitted position distribution. One has to be sure that the curvature of the cubic fit to the data does not invert within the active range of the detector. This would result in an ambiguity of the determined position.

Very accurate position resolution is achieved when a strong correlation between the calculated position and the measured position exists. The average position accuracy achieved was better than 2 cm. This corresponds to an angular resolution of better than 10° in the current detector configuration. Prior to the ^{18}F Coulomb excitation experiment, the detectors were placed in the array support structure and surrounded by the low-background lead, and the validity of the position calibration was checked again. A γ -source was placed at the secondary target position at the center of the array.

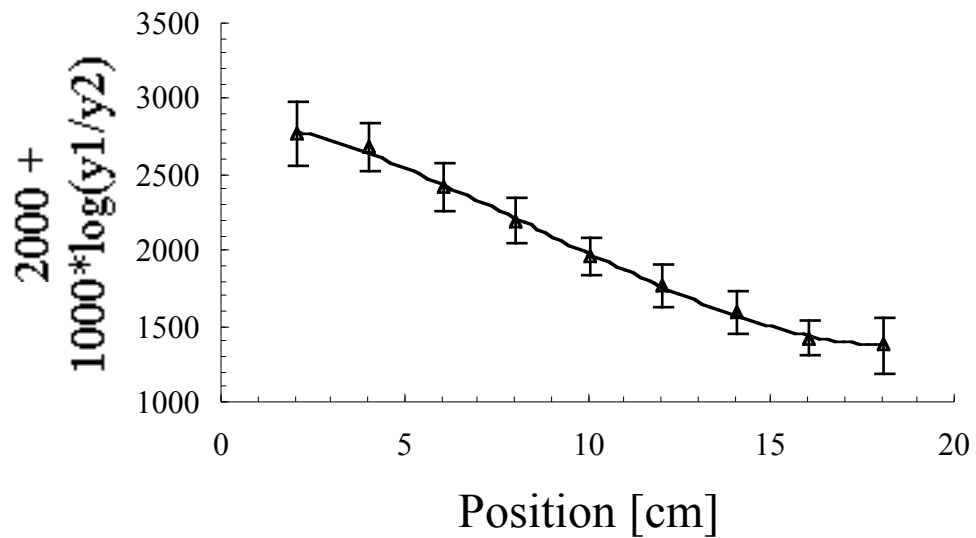


Figure 2.7: Typical position calibration spectrum for one detector. Shown is the true detector position (in cm) versus the calculated position from the two photomultiplier signals (in channel number). The points represent the measurements, the error bars represent the width of the distribution, and the solid line shows a cubic fit to the data.

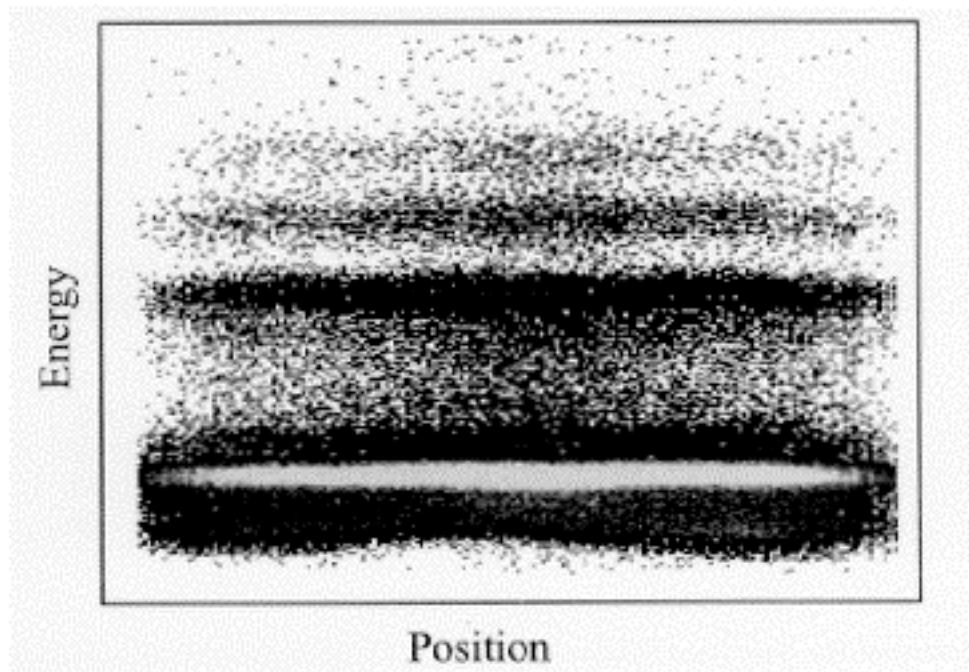


Figure 2.8: Calibrated position versus calibrated energy for one of the eleven inner ring NaI(Tl) detectors in the NSCL large-angle γ -array.

The correlation between the detected γ -ray energy and the calibrated position was recorded. If the position calibration is correct, one should see no correlation between the detected γ -ray energy and the calibrated position from a stationary source emitting radiation isotropically. This was confirmed using a ^{228}Th γ -ray source and presented in Figure 2.8.

2.2.4 Photopeak γ -Ray Energy Calibration of the NSCL γ -Detector Array

In order to generate a suitable γ -ray energy calibration for the 38 detectors in the γ -detector array, several sources emitting radiation ranging from 100 keV to 2.7 MeV were placed at the excitation target position at the center of the NSCL array. As demonstrated in Equation 2-3, the deposited energy in the photo-electric peak due to the interaction of the incoming photon with the detector crystal is approximately proportional to the square root of the product of the light yield from the two photomultiplier tubes (PMT's) [Won90]. A precise determination of γ -ray energy versus PMT signal was needed for each position slice of the 38 detectors. This process required an independent calibration for each of ten position slices for each detector. The pseudo parameter Position (see Equation 2-5), was used instead of the calibrated position parameter in order to limit the sources of error in the energy calibration.

A linear fit of channel number to a known γ -ray energy for each position slice was used to calibrate the energy signals detected in the appropriate detector portion. A typical energy calibration spectrum for a single position slice is presented in Figure 2.9. The linear dependence between the calibration energy (keV) and ADC signal (channels) calculated via Equation 2-3 can clearly be seen. The calibrated γ -ray sources used in this case were ^{88}Y and ^{228}Th (see appendix D). In order to confirm the independence of the calibrated position parameter and the calibrated energy, we plot the calibrated γ -ray

energy versus the ten calibrated position slices in Figure 2.8 for one individual detector using the ^{228}Th source. Note the 235 and 2651 keV γ -rays emitted in the decay of the ^{228}Th source are detected and appear at the same energy throughout the detector crystal.

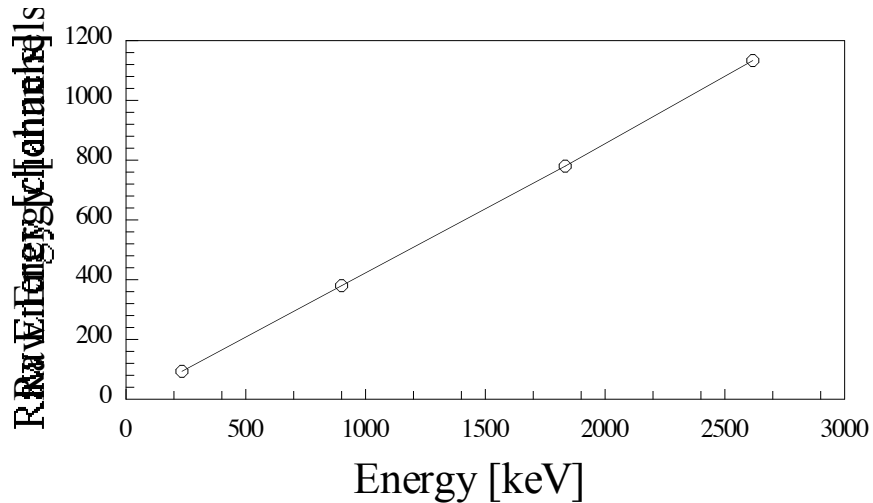


Figure 2.9: Typical photopeak γ -ray energy calibration for one detector and position slice using the ^{88}Y and ^{228}Th calibration sources. The open circles represent the measured data points.

Table 2.3, shows the energy calibration data for the γ -rays detected by the eleven detectors that comprise the inner ring of the NSCL γ -detector array. Photons spanning an energy range from 235 keV to 2615 keV were detected in the array from the decay of two calibrated sources, ^{228}Th and ^{88}Y . The centroids for individual calibration peaks, Table 2.3 and the energy resolution, measured in full-width at half-maximum (FWHM), are given for each of the calibration photons. Typically we obtained energy resolutions from $\approx 15\%$ for the 235.6 keV photon to values of $\approx 6\%$ for the 2615 keV photon (see Table 2.3). While some inner ring detectors had rather poor energy resolution, they were included in the data analysis to maximize the required spectrum statistics due to the low secondary beam rate and the subsequent low number of counts in the Coulomb-excitation photopeaks.

Table 2.3: Energy calibration and energy resolutions of the eleven detectors that form the inner ring of the NSCL large-angle γ -array, using the ^{88}Y and ^{228}Th calibration sources.

<i>Detector</i>	$E_\gamma = 235.6 \text{ keV}$		$E_\gamma = 898.1 \text{ keV}$		$E_\gamma = 1836.1 \text{ keV}$		$E_\gamma = 2615 \text{ keV}$	
	<i>chan</i>	<i>FWHM</i> (<i>chan</i>)	<i>chan</i>	<i>FWHM</i> (<i>chan</i>)	<i>chan</i>	<i>FWHM</i> (<i>chan</i>)	<i>chan</i>	<i>FWHM</i> (<i>chan</i>)
01	232.2	33.6	904.8	81.6	1838.9	120.1	2602.0	153.1
02	232.8	34.2	915.0	84.6	1855.1	120.5	2618.4	166.3
03	232.1	33.4	907.4	81.3	1843.2	108.4	2602.2	133.5
04	231.4	38.6	911.3	103.0	1852.8	131.5	2619.2	179.1
05	229.6	31.6	907.2	82.6	1843.1	107.5	2607.3	125.0
06	229.8	30.2	904.3	76.7	1839.5	96.5	2602.1	122.5
07	230.0	32.6	902.0	81.7	1834.6	107.0	2602.2	134.3
08	230.6	30.1	906.1	77.4	1841.3	96.9	2605.0	133.5
09	230.0	40.1	900.7	103.7	1836.2	127.7	2601.9	180.1
10	230.6	35.8	911.0	95.1	1853.1	122.9	2614.0	165.2
11	227.7	32.9	894.0	81.9	1820.6	107.7	2577.0	138.0
Avg	230.6	33.9	905.8	86.3	1841.7	113.3	2604.7	148.2

During the in-beam experiment we performed several qualitative calibrations in order to verify the stability of the detector energy calibrations. A ^{152}Eu γ -ray source was placed between the support structure and the lead shielding, allowing the source to illuminate the detectors to the extent that a qualitative determination of the stability of the energy calibrations could take place (the source could not be placed at the excitation target position as that would have required venting to air a significant portion of the beamline). The energy calibrations of the detectors did not change during the course of the experiment, allowing the use of the original calibrations for the entire experimental data set.

2.2.5 Photopeak Efficiency Calibration of the NSCL γ -Detector Array

The efficiency calibration of the NaI(Tl) detectors was performed with the set of calibrated sources listed in Appendix D. As with the energy calibration, we wanted to cover a wide range of photon energies. Calibrated sources of ^{88}Y , ^{152}Eu , and ^{228}Th were used. The ^{152}Eu source emitted strong photon lines at energies that filled in the gaps in energy of the other primary calibration sources. These three sources emitted photons with known intensities that adequately covered the energy range from 200 keV to 2700 keV. The sources were placed in the middle of the NSCL γ -detector array, replacing the excitation target during the calibration runs. The efficiency data was also calibrated for each of the ten position slices for each γ -ray detector. The efficiency for each position slice was determined by counting the number of calibration photons detected in a specific position slice, correcting for the live time of the data acquisition system, and comparing these values to the expected number of photons emitted from the calibrated source. The results of the efficiency calibration measurements for one detector is presented in Figure 2.10.

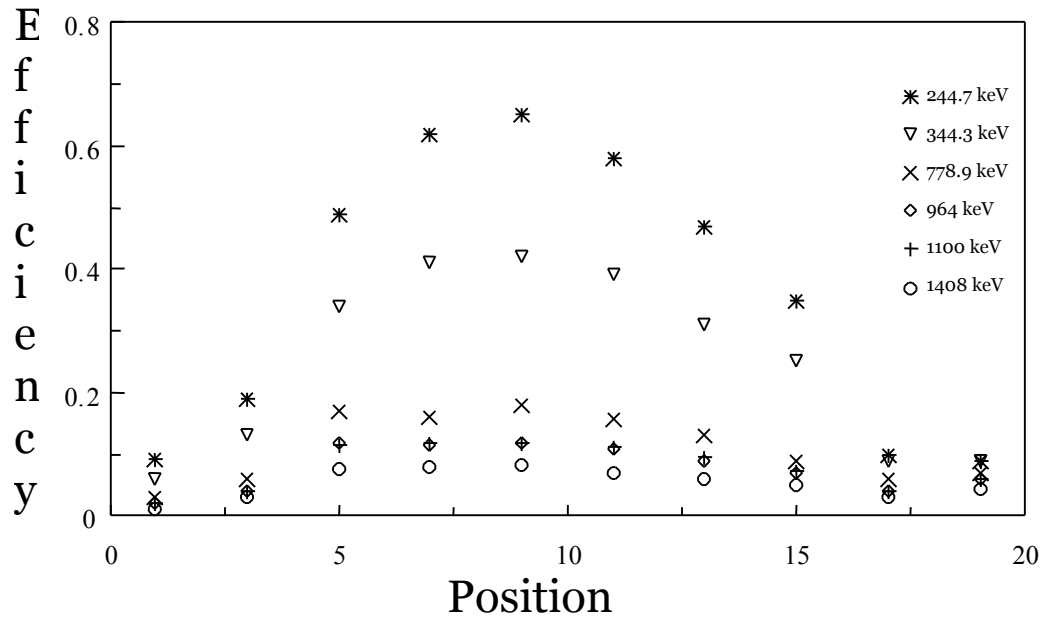


Figure 2.10: Photopeak efficiency for a typical NaI(Tl) detector from the NSCL large-angle γ -array, as a function of detector position for several different photon energies from the calibrated sources.

The energies displayed in Figure 2.10 range from 200 to 1500 keV. The higher-energy calibration curves are similar and are not displayed. The accuracy of the calibrated efficiency determined using this calibration method was verified using an alternative calibration method. The ^{88}Y source emits two photons at 898 and 1836 keV. These photons stem from a single nuclear decay and occur in sequence. The detector efficiencies for the specific photon energies can be obtained by measuring the coincidence rate of these correlated photons. The result from the coincidence measurement agreed within statistics with the calibrated efficiency values obtained from the original calibration method.

In order to represent the decrease in efficiency with increasing photon energy, we fit the calibrated efficiencies with a function typically used to model scintillator detector efficiencies [Won 90] :

$$\varepsilon = e^{-(a_0 + a_1 * \log(\frac{E\gamma}{50keV}))} * e^{-f(\ln(\frac{E\gamma}{50keV}) - 5)} \quad (2-6)$$

The second term in Equation 2-6 models the loss of efficiency at very low energies. The fit parameters a_0 , a_1 , and f for each detector slice were written to a table. Figure 2.11

presents the results from the efficiency calibration (data points) as well as the curves obtained using Equation 2-6. The results are shown for each of the ten position slices from a single NSCL array inner-ring detector. As one can see in this plot, by using this model, an excellent efficiency calibration can be achieved for the entire energy calibration range over the eight inner position slices. The final position slices can not be accurately represented by our efficiency model and therefore are excluded from the data analysis (several alternate efficiency models were tested with very little success in order to include the final position slices in the analysis).

The large efficiency loss for the low-energy calibration photons is caused by two primary factors: absorption of the low-energy γ -ray scintillations inside the detection crystal, and absorption of the γ -ray while passing through the aluminum accelerator beampipe. In order to eliminate detector noise and limit the amount of dead-time in the data acquisition unit, energy-signal discriminators were set at a relatively high energy value. This caused low energy photons that were detected at a position close to a phototube at one end of the crystal to be attenuated due to the length of the crystal to such an extent as to be too low in light output to trigger the relevant discriminator. This factor did not seriously impact our data analysis as the majority of the excitation photons of interest, except for the 184 keV ^{18}F isomeric decay γ -ray, were at energies above 700 keV.

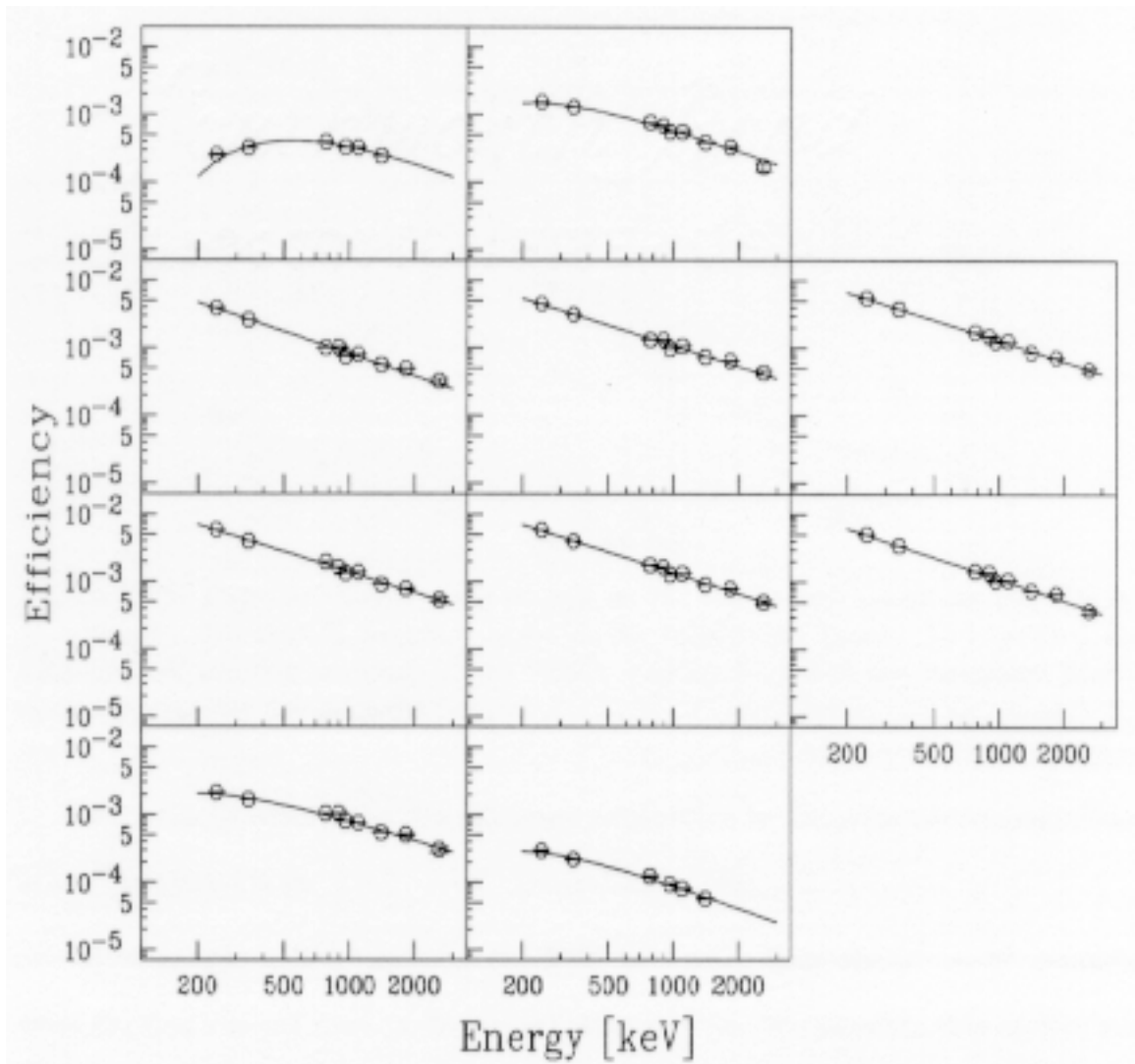


Figure 2.11: Efficiency for a typical inner ring NaI(Tl) detector divided into ten position slices. The open circles represent the measured efficiencies, with the lines showing a fit to the data, using equation 2-6. The position slices are in ascending order from left to right and from top to bottom.

2.3 Calibration of HPGe γ -ray detectors

Two high-purity Germanium detectors for monitoring the on-line purity of the secondary $^{18}\text{F}^m$ beam were placed facing the zero degree detector. The HPGe detectors were used to measure with good energy resolution (<3 keV) gamma-rays emitted during the decay of the $^{18}\text{F}^m$ ($T_{1/2} = 163$ ns) isomeric nuclei stopped by the zero-degree detector (see Figure 4.1). By comparing the number of captured isomeric gamma-rays to the number of ^{18}F particles identified by the ΔE v. TOF particle identification spectrum, one can calculate the $^{18}\text{F}^m$ isomeric composition of the secondary beam. A typical HPGe spectrum unambiguously showing the detection of ^{18}F isomeric γ -rays is displayed in Figure 2.12.

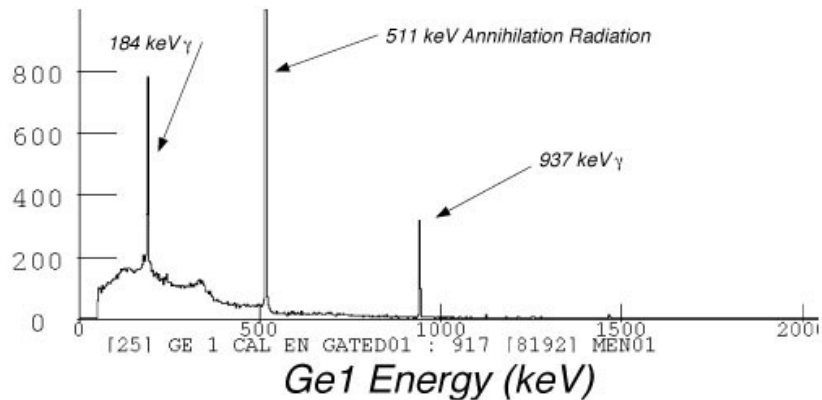


Figure 2.12: Typical HPGe detector spectrum gated in software by the ^{18}F particle identification in the DE v. TOF spectrum. Note the clear detection of the γ -rays produced in the decay of the 1.1 MeV isomeric state in ^{18}F nuclei.

An accurate energy and efficiency calibration of the High-Purity Germanium detectors was needed in order to calculate the number of $^{18}\text{F}^m$ nuclei in the beam using this method. This was achieved by carefully attaching a ^{60}Co calibrated γ -ray source to the front face of the zero-degree detector and moving the Germanium detectors into

place. The energy resolution achieved by the two HPGe detectors at 1.3 MeV were 2.48 keV (0.19%) and 2.64 keV (0.20%) respectively. A mixed radioactive calibration source (^{125}Sb , $^{154,155}\text{Eu}$) was used to determine an accurate efficiency calibration over the range of energies from 100 to 1600 keV (see appendix D). Calibration data were taken for several hours, giving the calculated efficiencies for the 184 and 938 keV ^{18}F isomeric γ -rays listed in Table 2.4.

Table 2.4 Calibration data for the two HPGe detectors using to monitor the secondary beam production of $^{18}\text{F}^m$.

E_γ [keV]	Ge1 Efficiency %	Ge2 Efficiency %	Total Efficiency (%)
184 keV	2.09(2)	1.55(2)	3.64(3)
938 keV	1.05(2)	0.71(2)	1.76(3)

CHAPTER 3

THE COULOMB EXCITATION OF ^{197}Au AND ^{12}C

3.1 Motivation and Introduction

In order to test the experimental setup and to determine the usefulness of the detector configuration in quantifying Coulomb excitation events, two peripheral experiments were run in tandem with the primary $^{18}\text{F}^m$ investigation. The experimental results of these tests will be presented in separate sections. The first section will present the experimental results of the Coulomb excitation of ^{197}Au target nuclei, from the $3/2^+$ ground state to the $7/2^+$ 548 keV excited state, through an electric quadrupole (E2) interaction with the ^{17}O primary beam. The second section will describe the experimental results of the Coulomb excitation of ^{12}C secondary beam nuclei, from the 0^+ ground state to the 2^+ 4.439 MeV excited state, through an electric quadrupole (E2) interaction with the ^{197}Au target. Due to the beam energies used in these experiments as well as the use of a “heavy” (*i.e.* high-Z) target together with detecting beam fragments at extreme forward scattering angles, we are certain to be examining effects primarily from Coulomb excitation, making the interpretation of the collected data straightforward. The measured Coulomb excitation cross-sections, along with the $B(E2\uparrow)$ strengths derived from our experimental data, for each experiment will be presented. These $B(E2\uparrow)$ values will be compared to published values from previous experiments to verify the ability of our experimental apparatus to accurately quantify Coulomb excitation events.

3.2 The Coulomb Excitation of ^{197}Au

The ^{12}C fragment production target located at the Dispersive Image 2 of the A1200 fragment separator (see Figure 2.2) was removed from the beam pathway, and the 45 MeV/nucleon ^{17}O primary beam was allowed to directly illuminate the ^{197}Au excitation target for this particular experiment. This increased the particle flux at the excitation target and only a short (~ 5 h) exposure was required to obtain sufficient statistics to measure the ^{197}Au Coulomb excitation cross section. A simplified ^{197}Au level scheme illustrating the Coulomb excitation of the $^{3/2^+}$ ground state is displayed in Figure 3.1.

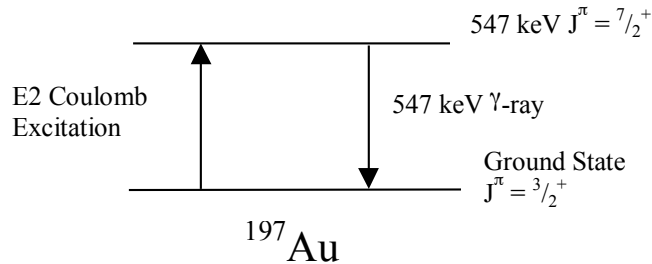


Figure 3.1: A simplified level scheme for ^{197}Au . The ^{197}Au nucleus in its ground state is promoted to the 548 keV excited state via an electric quadrupole (E2) Coulomb excitation, followed by the emission of a 548 keV de-excitation photon.

The raw and Doppler-corrected γ -ray spectra for the ^{197}Au excitation target are presented in Figure 3.2. These spectra represent summed spectra collected from the eleven NaI(Tl) detectors that comprise the inner ring of the NSCL γ -detector array. Each was recorded with the condition that a ^{17}O beam particle was detected in the zero-degree detector ($\theta_{lab} \leq 5.6^\circ$). As previously noted, this insures that the excitation will be primarily pure Coulomb in nature. In other words, the γ -ray detected in the NSCL array was emitted from the subsequent deexcitation of a nucleus excited by the interaction of the electric fields of a beam particle (identified in the zero-degree detector as a ^{17}O ion—see Figure 3.3) and the ^{197}Au excitation target atom. In the laboratory frame ($\beta = 0$) the intense

photopeak with a centroid corresponding to a γ -ray energy of approximately 540 keV is clearly visible while in the projectile frame ($\beta = 0.27c$) this photopeak is broader in energy. These spectra indicate that the γ -rays in the ~ 540 keV photopeak detected in the NSCL array were emitted by a stationary source, leading one to identify the photopeak in the lab frame spectrum (Figure 3.2a) as the γ -rays produced by the 548 keV deexcitation of the $7/2^+$ excited state in ^{197}Au to the $3/2^+$ ground state. The width of this photopeak was measured to be 59 keV (10.8% FWHM). This agrees well with the data collected during the energy calibration of the NSCL array (see section 2.2.4). Assuming Rutherford trajectories, one calculates the minimum impact parameter between the ^{197}Au excitation target and the ^{17}O nuclei to be approximately 14 fm (Figure 1.4). This is about 3 fm larger than the distance between the centers of the ^{197}Au target and the ^{17}O projectile, assuming touching spheres. In this case and at these distances, it was important to restrict angles in order to sample impact parameters appropriate for Coulomb excitation. This assures that the photons detected in the NSCL array are indeed primarily due to Coulomb excitation events [Pri99].

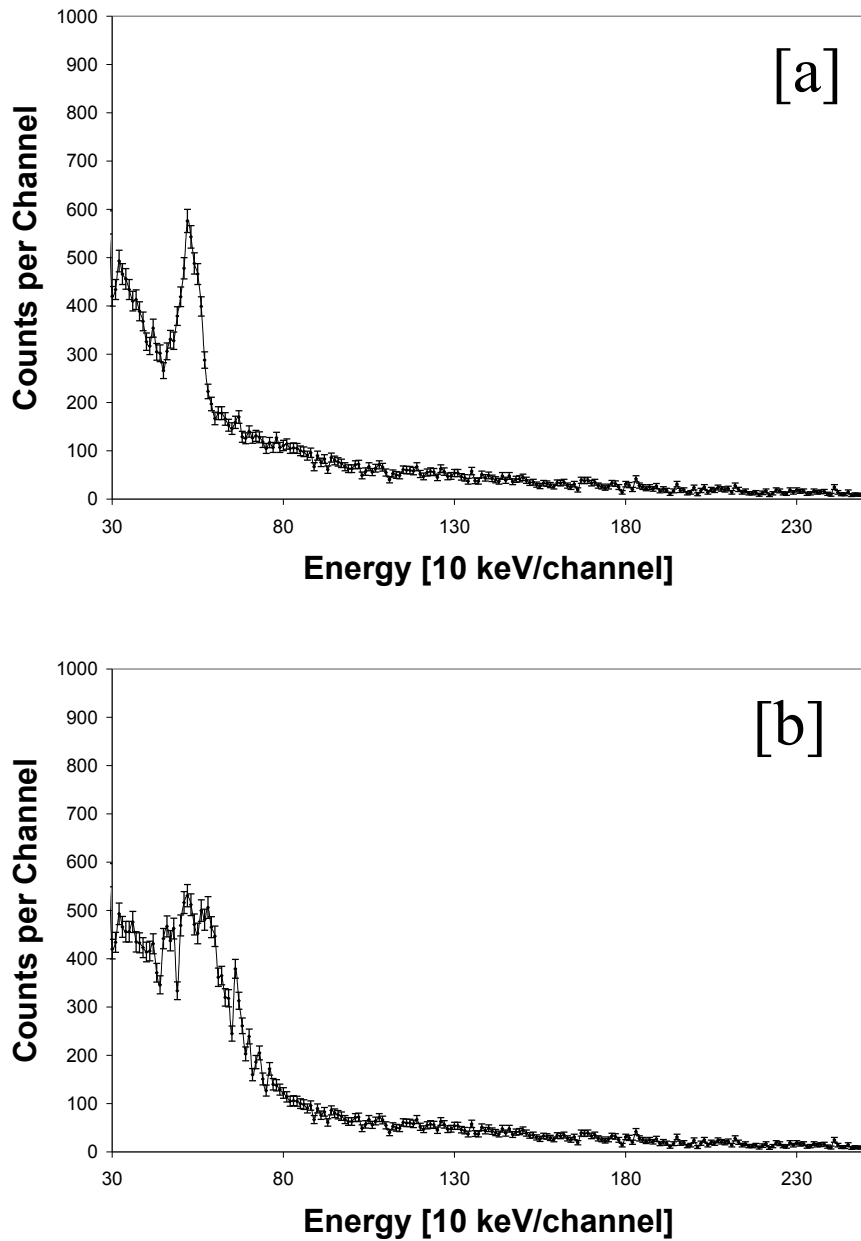


Figure 3.2: Raw [a] and Doppler-corrected [b] spectra for the Coulomb excitation of the ^{197}Au excitation target. Note the 548 keV excitation in the laboratory frame ($a_j; \beta = 0$) that dissipates in the projectile ($b_j; \beta = 0.28c$) frame.

In order to determine the cross section for the ^{197}Au target excitation, one can employ the equation commonly used to calculate cross sections:

$$\sigma_{clx} = \left[\frac{\gamma_{yield}}{\varepsilon_{\gamma} P_{flux}} \right] \left[\frac{AW_{tgt}}{N_a Tk_{tgt}} \right] \quad (3-1)$$

where the first half of the equation is comprised of three parameters: γ_{yield} represents the integrated number of background-subtracted γ -rays in the ^{197}Au Coulomb-excitation photopeak assuming uniform emission into 4π solid angle, ε_{γ} is the photopeak detection efficiency of the NSCL array at the γ -ray energy of interest, and P_{flux} represents the corresponding integrated number of ^{17}O beam particles detected in the zero-degree detector ($\theta_{lab} \leq 5.6^{\circ}$). The second portion of the equation represents the number of scattering centers in the excitation target with AW_{tgt} representing the atomic weight of the ^{197}Au target (197 g/mole), N_a carrying its usual definition of Avagadro's number ($6.022 \times 10^{23} \text{ atoms/mole}$), and Tk_{tgt} symbolizing the thickness of the ^{197}Au excitation target (0.2348 g/cm^2). When calculating the efficiency of the NSCL array, care was taken to correct the efficiency value for the absorption of Coulomb-excitation photons within the relatively dense ^{197}Au target material. The number of detected events also can be effected by the angular distribution of the emitted photons. In the case of the Coulomb excitation of ^{197}Au target nuclei from a $3/2^+$ ground state to a $7/2^+$ 548 keV excited state, the angular distribution on the subsequent emission of a de-excitation γ -ray is isotropic and therefore can be ignored.

By including all eleven inner ring detectors in the final analysis of the ^{197}Au target excitation, we were able to accumulate 2010 ± 59 counts in the background-subtracted 548 keV photopeak in approximately five hours. The final value and quoted error for the background-subtracted photopeak take into account the statistical uncertainties (added in quadrature) of three independent fits to the spectra summed over the eleven inner ring

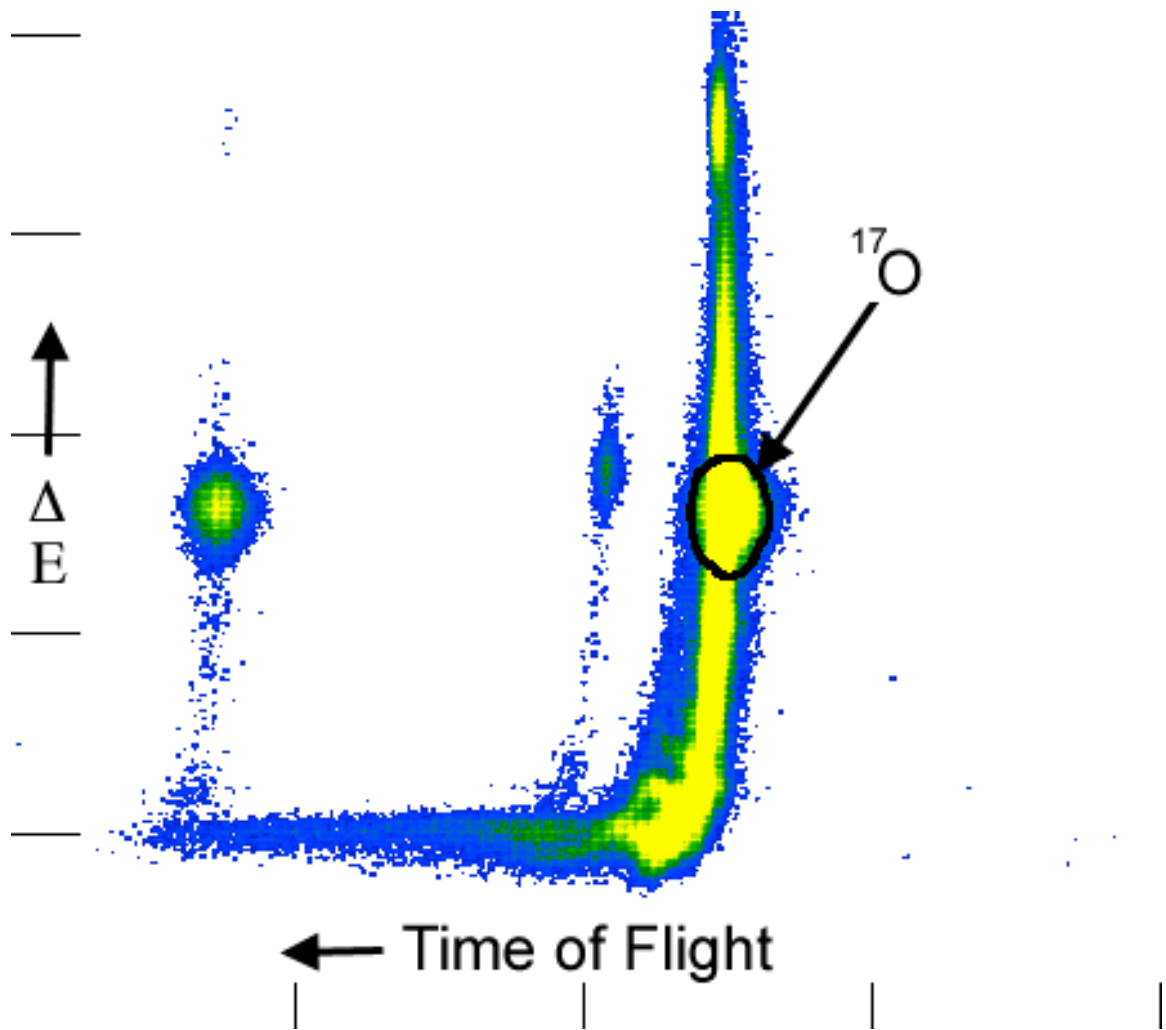


Figure 3.3: Particle identification spectrum displaying Energy loss (ΔE) versus Time of Flight for the ^{197}Au Coulomb excitation data. The energy and time resolution in the zero-degree detector allows us to identify beam constituents. Note the software gate identifying the ^{17}O nuclei.

detectors. Table 3.1 displays the results of three fits of the background-subtracted 548 keV photopeak.

Table 3.1: Computational Fits for the yield of the 548 keV γ -ray from ^{197}Au after Coulomb excitation.

<i>Fit</i>	<i>Background -Subtracted Area</i>	<i>Background -Subtracted Area Uncertainty</i>	<i>Width (FWHM)</i>	<i>Width (FWHM) Uncertainty</i>	<i>Chi square/ D.o.F.</i>
1*	2087	103	60.5	1.8	1.01
2	1954	101	58.1	1.8	1.51
3	1990	101	58.7	1.8	1.43
Average 2,3	1972	71	58.4	1.27	
Average 1-3	2010	59	59.1	1.04	

**Fit 1 omitted from final cross section calculation based on statistical comparison*

If one examines the chi square/degrees of freedom (D.o.F.) values, the fit labeled Fit 1 returns a value of 1.003 which is statistically very improbable for fitting a Gaussian peak acquired with a NaI(Tl) detector via an analog to digital converter (ADC). Typically, gamma-ray detector responses being converted by ADC's exhibit a binning effect and introduce an additional electronic variance factor which broadens the photopeak. While this added peak width is adequately dealt with by conducting a good energy and efficiency calibration prior to the experiment, the statistical fitting process is not informed by the calibration information. This conflict typically leads to a proper chi square/ D.o.F. value of 1.3-1.5. Using the average value (2010 counts) of the three statistical fits, we extracted a Coulomb excitation cross section of (21.1 ± 1.5) mb for the ^{197}Au target excitation. The quoted uncertainty takes into account the statistical uncertainty, and uncertainties from the background subtraction, the efficiency calibration, as well as the correction for the photon absorption in the target. The individual uncertainties listed in Table 3.2 were added in quadrature to arrive at the total cross sectional uncertainty.

Table 3.2: Sources of uncertainty included in the final ^{197}Au Coulomb excitation cross section.

<i>Target Excitation</i>	<i>Statistical [%]</i>	<i>Fit/ Background [%]</i>	<i>Efficiency [%]</i>	<i>Absorption [%]</i>	<i>Total Error [%]</i>
^{197}Au	2	3	5	4	7

Assuming pure first-order Coulomb excitation and adopting the formalism of Alder and Winther [Win79] (see Appendix A), we extract the reduced “up” transition strength, $B(E2\uparrow)$ of $5003 \pm 350 e^2\text{fm}^4$ for the Coulomb excitation of ^{197}Au target nuclei from a $3/2^+$ ground state to a $7/2^+$ 548 keV excited state from the measured Coulomb excitation cross section. Our $B(E2\uparrow)$ value is compared to various published results of previous Coulomb excitation experiments, as well as to values obtained from lifetime measurements. These are listed in Table 3.3. A brief explanation on the relationship between the lifetime of an excited state and the corresponding reduced “up” transition strength can be found in Appendix B.

Table 3.3: Experimental and Theoretical $B(E2\uparrow)$ values for the $7/2^+$ to $3/2^+$ transition in ^{197}Au .

<i>Experiment</i>	<i>Reference</i>	<i>Excitation Beam</i>	<i>E_{lab} [MeV/nucleon]</i>	<i>$B(E2\uparrow)$ [$e^2\text{fm}^4$]</i>
Initial Value	-	^{17}O	45	5003 ± 350
Final Value	-	^{17}O	45	4910 ± 340
2	[Fog71]			4570 ± 120
3	[Mcg71]			4470 ± 220
Adopted*	NDS 42 p.481	-	-	4988 ± 249

* Based on an adopted experimental decay lifetime of 6.65(17) ps.

As can be seen in Figure 3.4, our final value for the reduced transition strength for the gold target excitation agrees within statistics with both the published experimental values and with the value calculated from the experimentally deduced lifetime of the $7/2^+$ excited state. Our initial calculation for the $B(E2\uparrow)$ value could be due to the inclusion of a high value for the background-corrected photopeak during the fit process. On this basis, we can omit Fit 1 from the data set used to calculate the Coulomb cross section and arrive

at a final value of 20.7 ± 1.5 mb. This cross section results in a “final” value for the reduced transition strength of 4910 ± 340 e²fm⁴.

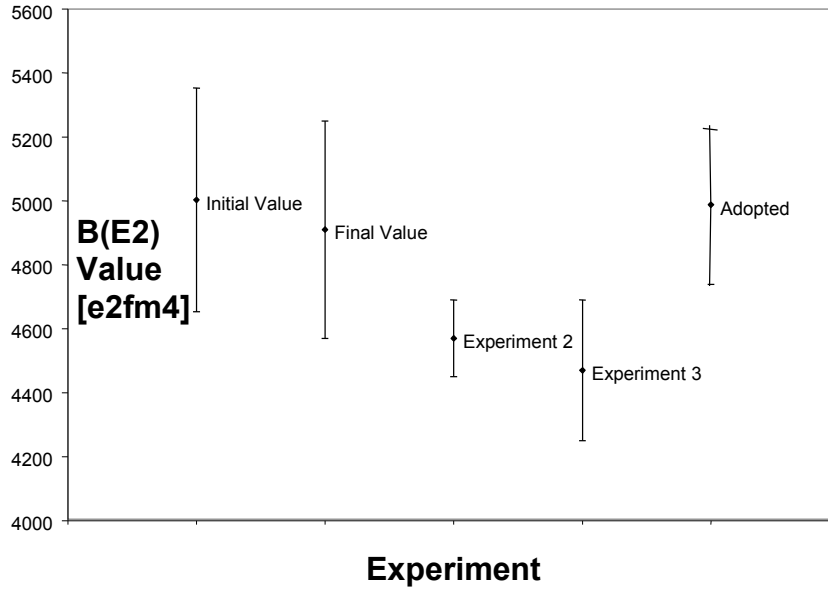


Figure 3.4: A comparison of experimental and deduced reduced transition probabilities $B(E2\uparrow)$ for the $7/2^+$ to $3/2^+$ transition in ^{197}Au . The data labels used in this Figure correspond to the labels used in Table 3.3

In conclusion, the extracted value for $B(E2\uparrow)$ of $4910(340)$ e²fm⁴ for the ^{197}Au target excitation agrees well with both previous experimental data as well as with values calculated from experimentally-derived lifetimes. While our value is slightly higher than the previous Coulomb excitation measurements, all values agree within error bars including the lifetime measurements. The fact that the previous measurements can only account for about 90% of the adopted $B(E2\uparrow)$ value extracted from the lifetime measurements indicates that nuclear excitation effects could be present. However, our current measurement seem to limit the contribution of nuclear mechanisms to the reduced transition strength to below the precision of the experimental measurements (*i.e.* 7%).

3.3 The Coulomb Excitation of ^{12}C

To determine the ability of the NSCL array to measure the Coulomb excitation of high- β in-flight beam fragments, a constituent of the mixed beam produced in the ^{12}C ($^{17}\text{O}, ^{18}\text{F}$) ^{11}B primary reaction was examined. The ^{12}C production target located at the Dispersive Image 2 of the A1200 fragment separator (see Figure 2.2) for this particular experiment was returned to the beam pathway, and the zero-degree detector was instructed by software to require the detection of a ^{12}C beam fragment along with gamma-rays in the NSCL array (see Figure 3.5).

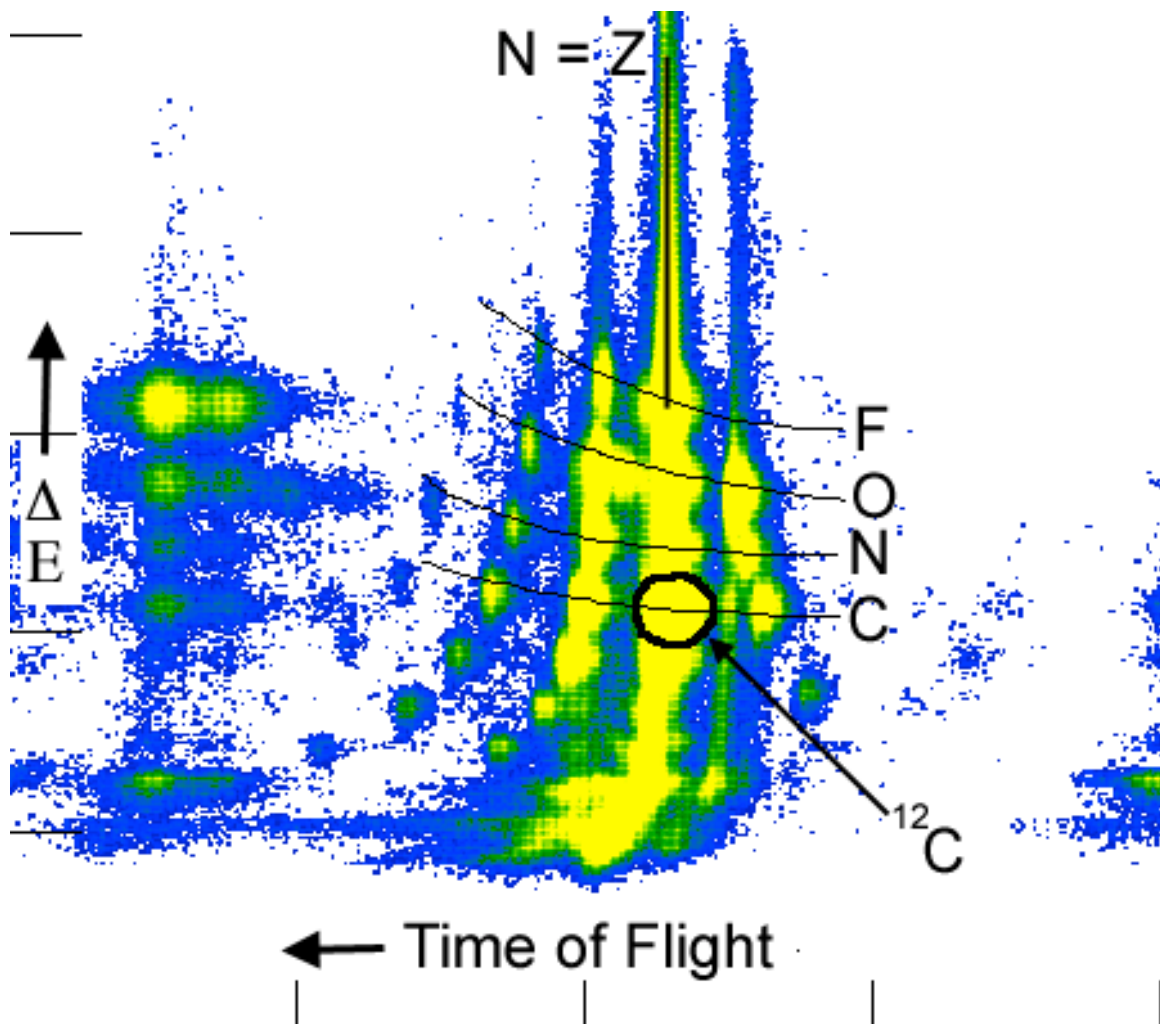


Figure 3.5: Particle-identification spectrum displaying ΔE versus Time of Flight for the ^{12}C Coulomb excitation data. The energy and time resolution in the zero-degree detector allows us to identify beam constituents. Note the software gate identifying the ^{12}C nuclei.

This allowed us to search for photons indicating a transition between the 0^+ ground state in ^{12}C and the 4.439 MeV 2^+ excited state. A simplified ^{12}C level scheme illustrating the Coulomb excitation of the 0^+ ground state is displayed in Figure 3.6.

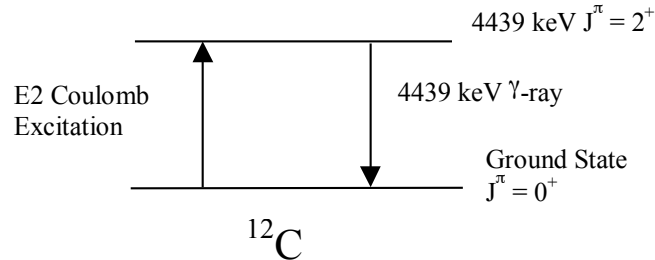


Figure 3.6: A simplified level scheme for ^{12}C . A ^{12}C nucleus in its ground state is promoted to the 4439 keV excited state via an electric quadrupole (E2) Coulomb excitation, followed by the emission of a 4439 keV de-excitation photon.

In Figure 3.7 we show raw (lab-frame) and Doppler-corrected γ -ray energy spectra, recorded under the condition that a ^{12}C fragment was detected in the zero degree-detector along with a coincident γ -ray in the NSCL array. As in section 3.2, the spectra displayed are summed over the eleven NaI(Tl) detectors that form the inner ring of the NSCL γ -array used for analysis. In the projectile frame ($b_j: \beta = 0.27c$) two peaks with centroids corresponding to γ -ray energies of approximately 4.4 MeV and 3.85 MeV are visible, while in the laboratory frame ($a_j: \beta = 0$) these photopeaks disperse. These spectra indicate that the γ -rays producing the high energy peaks were emitted by a source moving at beam velocity, leading one to identify the peaks in the projectile-frame spectrum [b] as the photopeak and first-escape peak produced by the 4.4

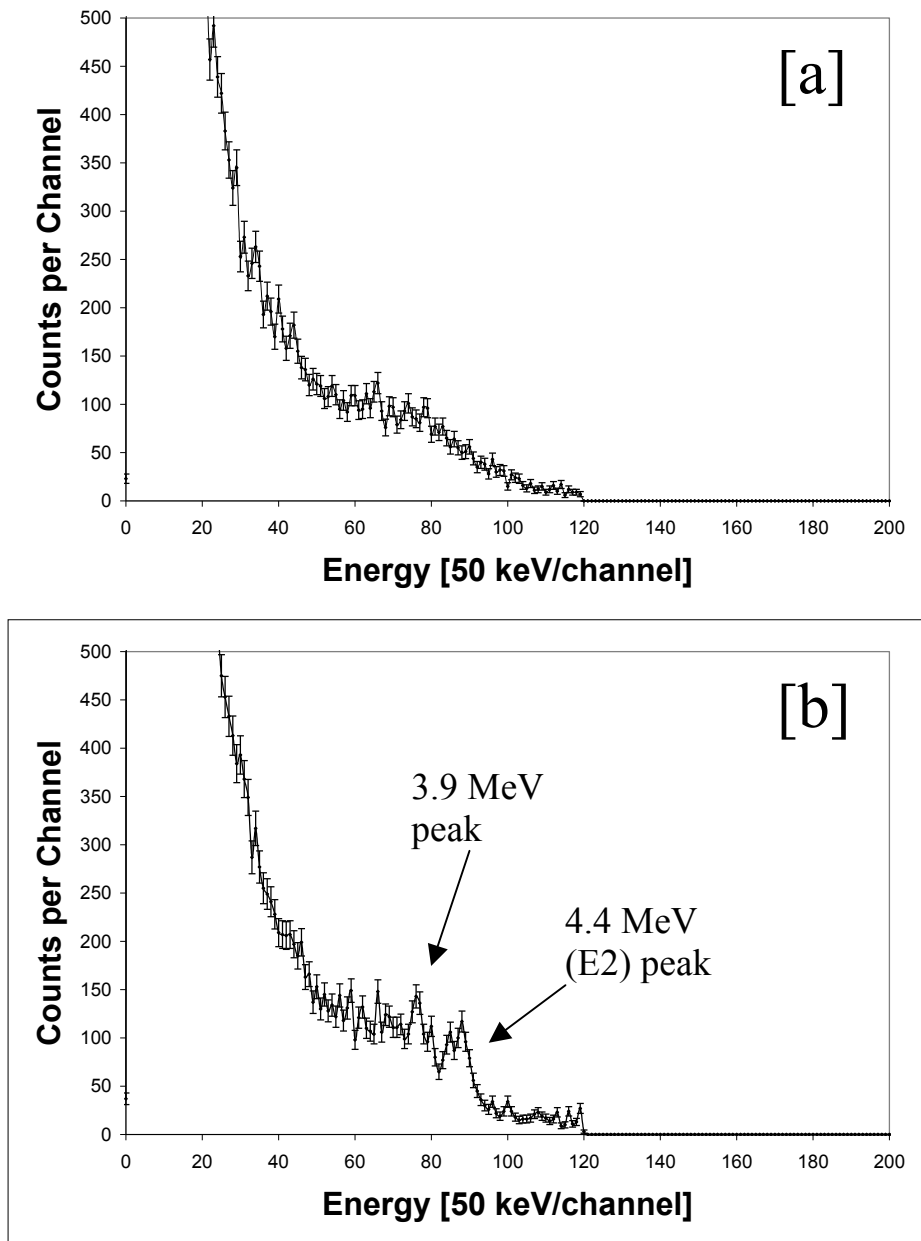


Figure 3.7: Raw [a] and Doppler-corrected [b] energy spectrum for the ^{12}C Coulomb excitation data. Note that the excitation photopeaks in the projectile ($b_j; \beta = 0.27c$) frame dissipate in the laboratory frame ($a_j; \beta = 0$).

MeV de-excitation of the 2^+ excited state in ^{12}C to the 0^+ ground state. There was no indication of a double-escape peak. The width of the 4.4 MeV photopeak was measured to be 225 keV (5.1%) FWHM. The experimentally-identified photon energy falls outside the energy calibration range of the NSCL array making direct comparison with the calibrated widths at this energy impossible. However, by extrapolating from the calibration data, one can confirm that a FWHM width of 5% at 4.4 MeV falls within the resolution of the array expected at this energy (see section 2.2.4). Assuming Rutherford trajectories, one can calculate the minimum impact parameter between the ^{197}Au excitation target and the ^{12}C nuclei to be approximately 16 fm. This is about 6 fm larger than the distance between the centers of the ^{197}Au target and the ^{12}C projectile assuming touching spheres. In this case and at these distances, one can certainly estimate that nuclear contributions to the reaction cross section at the forward angles covered by the zero-degree detector are small. This assures that the photons detected in the NSCL array are indeed primarily due to Coulomb excitation events.

By including all eleven inner ring detectors in the final analysis of the ^{12}C beam excitation, we were able to accumulate 271 ± 25 counts in the background-subtracted 4.4 MeV photopeak and 163 ± 25 net counts in the 3.9 MeV escape peak in approximately nineteen hours. The adopted value and the quoted uncertainty for the background-subtracted peaks take into account the statistical uncertainties (added in quadrature) of three independent fits to the spectra summed over the eleven inner ring detectors. Table 3.4 displays the data gathered from the three fits of the background-subtracted peaks.

Table 3.4: Fits of the 4.4 MeV photopeak and first-escape peak due to the Coulomb excitation of the ^{12}C beam fragments.

<i>Fit</i>	<i>Background -Subtracted Area</i>	<i>Background -Subtracted Area Uncertainty</i>	<i>Width (FWHM) keV</i>	<i>Width (FWHM) keV Uncertainty</i>	<i>Chi square/ D.o.F.</i>
1 (photo)	268	44	240	26	1.59
2 (photo)	236	42	220	26	1.52
3 (photo)	224	41	214	25	1.56
Average	271	25	225	26	
1 (escape)	175	43	234	26	1.59
2 (escape)	147	40	214	26	1.52
3 (escape)	160	39	209	25	1.56
Average	163	24	219	26	

As in section 3.2, one can employ equation 3-1 to arrive at the Coulomb excitation cross section for the ^{12}C excitation. By taking the average photopeak value (271 counts) of the three statistical fits, we extract a Coulomb excitation cross section of (11.5 ± 1.4) mb for the ^{12}C beam fragment excitation. The quoted uncertainties take into account the statistical uncertainty, the uncertainty from the background subtraction, the uncertainty due to the efficiency calibration, as well as the error introduced by correcting for the photon absorption in the target. The individual uncertainties listed in Table 3.5 were added in quadrature to arrive at the total cross sectional uncertainty.

Table 3.5: Sources of uncertainty included in the calculated ^{12}C Coulomb excitation cross section.

<i>Projectile Excitation</i>	<i>Statistical [%]</i>	<i>Fit/ Background [%]</i>	<i>Efficiency [%]</i>	<i>Absorption [%]</i>	<i>Total Uncertainty [%]</i>
^{12}C	2	8	5	7	12

From the area of the ^{12}C photopeak, we extract a Coulomb excitation cross section of (11.5 ± 1.4) mb for the ^{12}C beam-fragment excitation. Again, assuming pure first-order Coulomb excitation and adopting the formalism put forth by Alder and Winther [Win79] (see Appendix A), we extracted a modified reduced transition strength, $B(E2\uparrow)$

of $52 \pm 6 e^2\text{fm}^4$ for the Coulomb excitation of ^{12}C projectile nuclei from a 0^+ ground state to a 2^+ 4.4 MeV excited state from the measured Coulomb cross section. Our $B(E2\uparrow)$ value agrees within uncertainties with various published results of previous Coulomb excitation experiments as well as to calculations of the transition strength based on lifetime measurements. These comparisons are listed in Table 3.6 (see Appendix B).

Table 3.6: Experimental and Theoretical $B(E2\uparrow)$ values for the 2^+ to 0^+ transition in ^{12}C .

<i>Experiment</i>	<i>Reference</i>	<i>Excitation Beam</i>	<i>E_{lab} [MeV/nucleon]</i>	<i>B(E2) [e²fm⁴]</i>
Photopeak	This expt.	^{12}C	40	52 ± 6
Literature				41 ± 5
Adopted*	NDS 42 p.481	-	-	43 ± 5

* Based on an adopted experimental decay lifetime of 58 fs.

CHAPTER 4

THE COULOMB EXCITATION OF $^{18}\text{F}_{g.s.}$ AND $^{18}\text{F}^m$

4.1 Motivation and Introduction

Measurements of proton scattering on both the ground and excited state of ^{18}F have previously been performed [Bro95] as well as measurements of the total reaction cross sections for ^{18}F and $^{18}\text{F}^m$ on Si [Rob95]. In these experiments, the relative populations of nuclei in the $^{18}\text{F}_{g.s.}$ and the $^{18}\text{F}^m$ isomeric state were measured by a method of detecting the isomeric de-excitation gamma-rays denoted as “gamma-tagging”. We also employ this “gamma-tagging”, the NSCL NaI(Tl) array, and the intermediate-energy Coulomb excitation technique to look for collective states built over the $J=5^+$, $E_x = 1.121$ MeV isomeric ($T_{1/2} = 163$ nsec) state in ^{18}F . An extensive nuclear level scheme for ^{18}F is displayed in Figure 4.1 [Fir96].

4.2 Experimental Procedure

To produce the ^{18}F secondary beam, a primary beam of $^{17}\text{O}^{8+}$ with an energy of $E/A = 45$ MeV was produced with the NSCL ion source and accelerated in the K1200 cyclotron. A ^{12}C production target located at the Dispersive Image 2 of the A1200 fragment separator (see Figure 2.2) was used for this particular experiment, and the ^{18}F secondary beam was obtained via a $^{12}\text{C} (^{17}\text{O}, ^{18}\text{F}) ^{11}\text{B}$ primary beam transfer reaction. The various beam constituents produced in this reaction are displayed in Figure 4.2 with ^{18}F being the major nucleus produced at $\sim 64\%$ of the total secondary beam. After optimizing the production of $^{18}\text{F}^m$ using the “gamma-tagging” technique (see section 2.2.1), the zero-degree plastic scintillator detector was instructed in software to require the detection of

^{18}F beam fragments using a time-of-flight method (see Figure 4.2) along with coincident gamma-rays detected in the NSCL array.

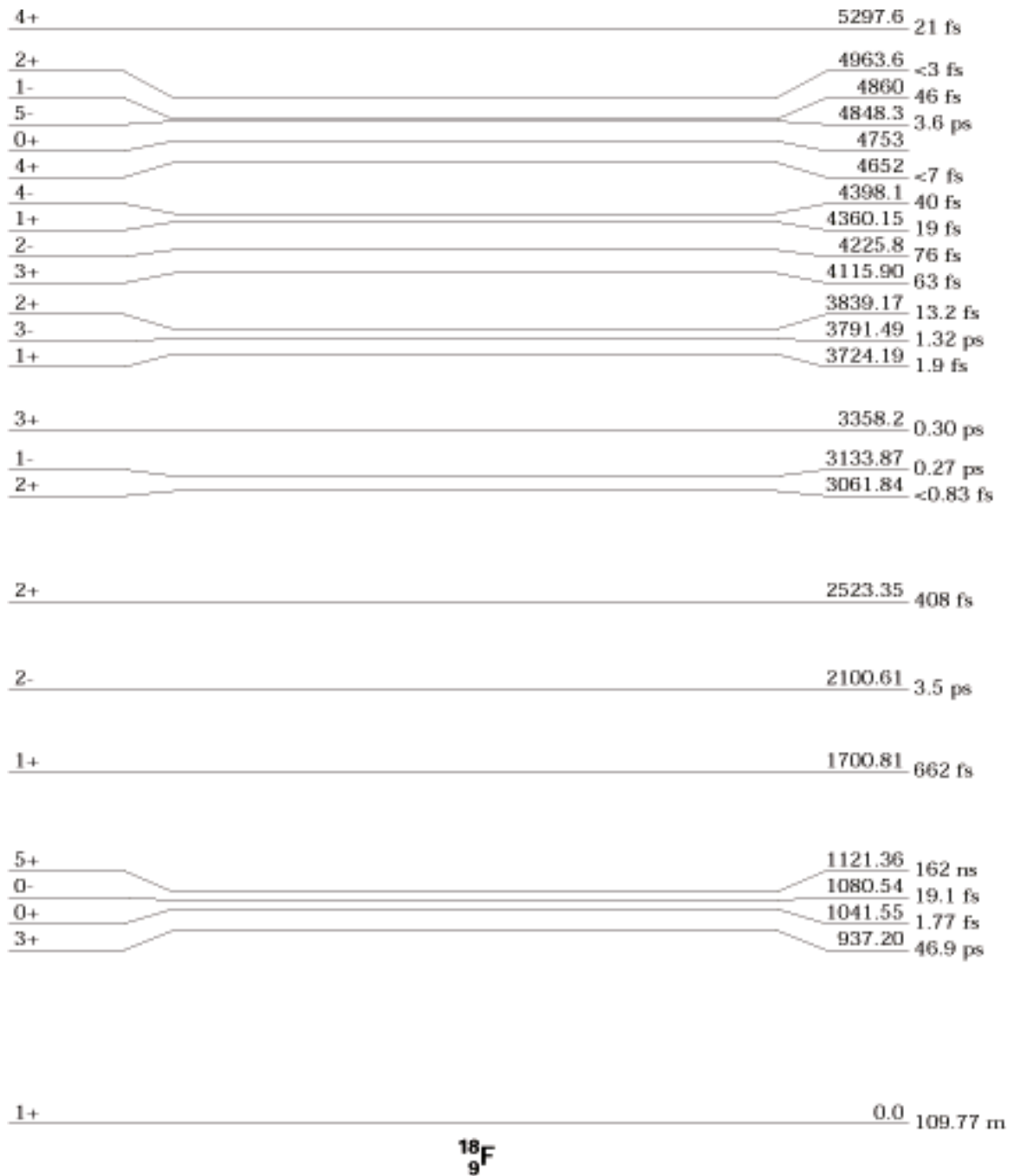


Figure 4.1: Level Scheme of ^{18}F . The labels on the left of the figure denote the spins and parities of the levels whereas the labels on the right give the level energies in keV and the half-lives.

Although we are searching primarily for collective states built over the 1.121 MeV ($J^\pi = 5^+$) $^{18}\text{F}^m$ isomeric state, this beam particle identification condition does not differentiate between $^{18}\text{F}_{\text{g.s.}}$ and $^{18}\text{F}^m$ nuclei. Consequently, the coincident photons detected in the NSCL array are not only due to Coulomb interactions with ^{18}F nuclei in the isomeric state, but will also include any photons produced from $^{18}\text{F}_{\text{g.s.}}$ interactions with the ^{197}Au excitation target. One also must exclude the detection of gamma-rays from processes other than the Coulomb to confidently assign any photopeaks to Coulomb excitation. To that end, a timing spectrum was constructed by requiring a ^{18}F nucleus in the Delta E-time of flight (ΔE -TOF) particle ID spectrum and a coincident gamma-ray in the NSCL large-angle array.

A typical timing spectrum (gated on a γ -ray multiplicity parameter that requires the detection of at least one gamma-ray in coincidence with a beam particle) from a single PMT at one end of a inner-ring NaI(Tl) detector is presented in Figure 4.3. Two distinct timing peaks can be resolved in this figure. The first peak corresponds to gamma-rays detected at a time corresponding to a beam particle interaction with the ^{197}Au excitation target while the second peak corresponds to gamma-rays produced at a time correlated with an interaction with the zero-degree detector. The in-flight decay and target-excitation peak indicated in Figure 4.3 are much stronger than the zero-degree detector peak. This contradicts what is normally observed in an intermediate-energy Coulomb excitation experiment and needs explanation. Because of the low probability of Coulomb interaction, typically the photons due to interactions with the front face of the stopping detector are detected in the large-angle γ -array with a rate much greater than the corresponding Coulomb de-excitation photons (see Figure 4.4). This leads to a timing spectrum in which the timing peak due to Coulomb interactions with the excitation target is orders of magnitude smaller than the timing peak corresponding to photons emitted after interactions with the face of the zero-degree detector.

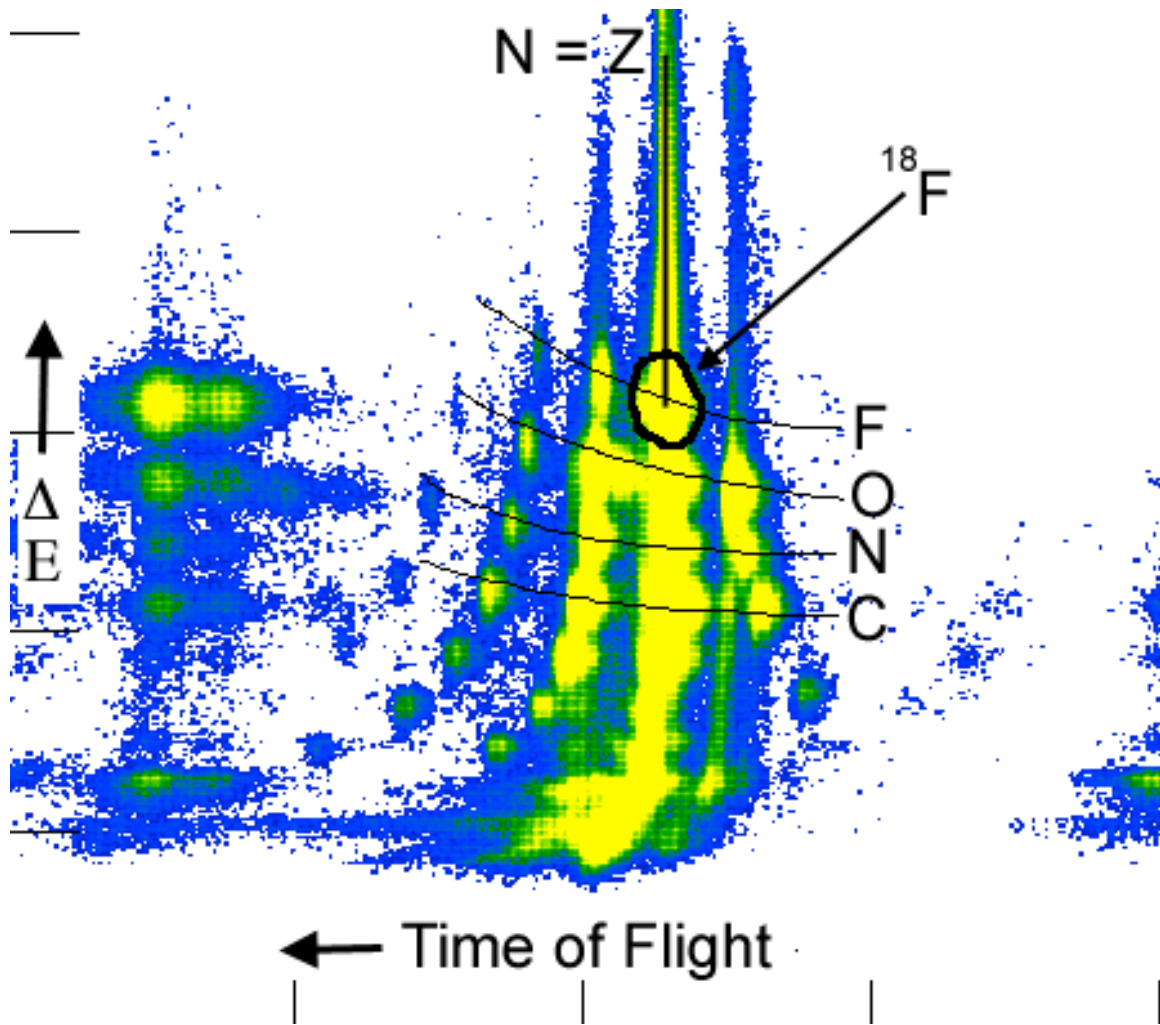


Figure 4.2: Particle-identification spectrum displaying Energy loss (ΔE) versus Time of Flight for the ^{18}F Coulomb excitation data. The energy and time resolution in this zero-degree detector allows us to identify beam constituents. Note the software gate identifying the ^{18}F nuclei.

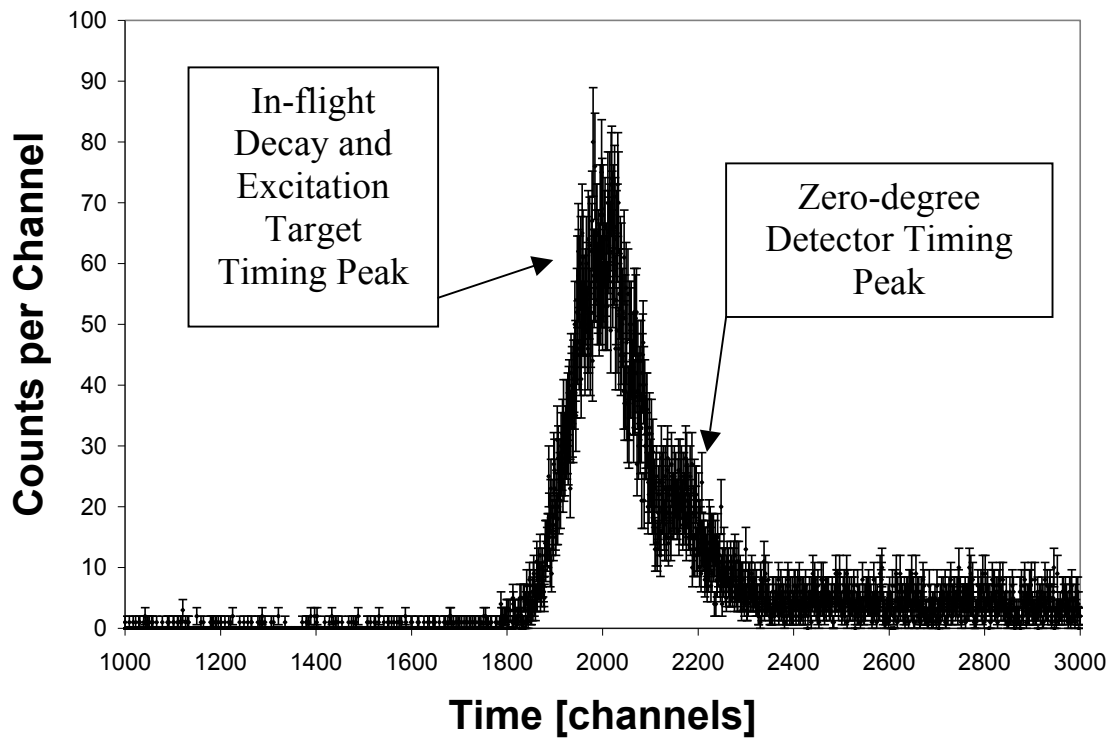


Figure 4.3: Transit-timing spectrum for the ^{18}F Coulomb excitation experiment. Note the timing peak corresponding to Coulomb excitation and in-flight decay events at or near the excitation target and events from beam projectile collisions with the zero-degree detector.

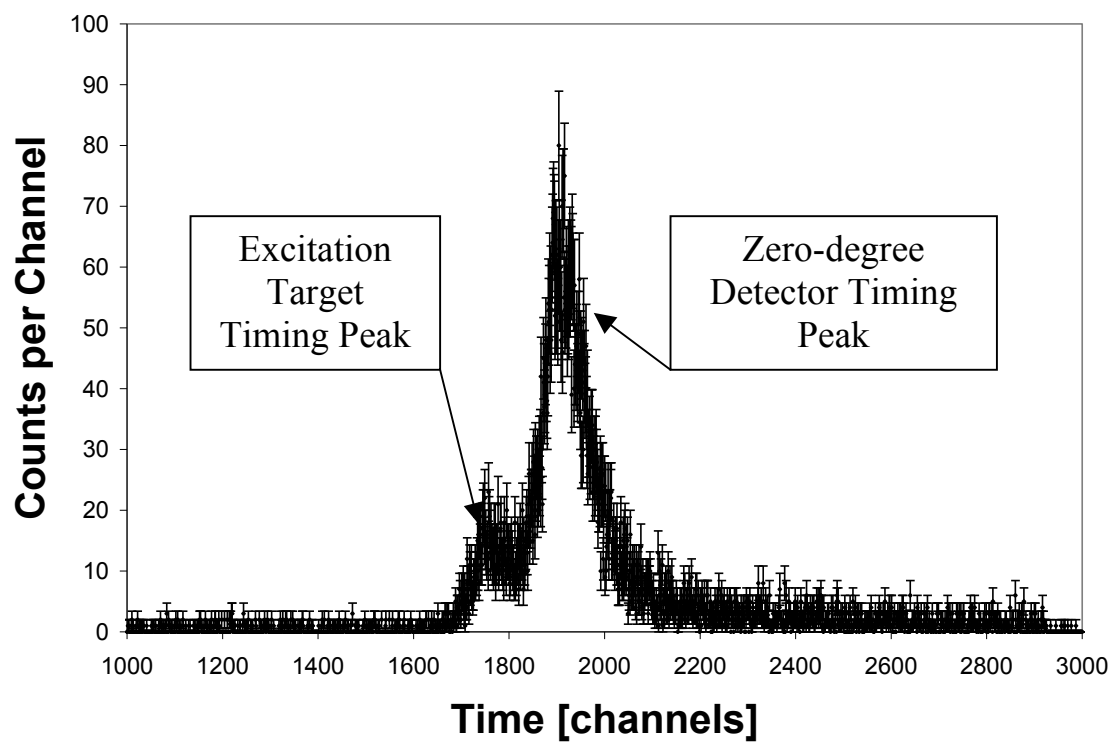


Figure 4.4: Transit timing spectrum for ^{197}Au Coulomb excitation experiment. Note the timing peak corresponding to Coulomb excitation events at the excitation target and events from beam projectile collisions with the zero-degree detector.

4.3 Results and Discussion

4.3.1 Observations

In order to identify the origin of the unusually large amount of events in the target excitation timing peak, two γ -ray energy spectra were constructed. In Figure 4.5 we show raw (lab-frame) and Doppler-corrected γ -ray energy spectra recorded under the condition that a ^{18}F nucleus was detected in the ΔE -TOF particle ID spectrum and a coincident γ -ray in the NSCL array was detected with a time corresponding to the target excitation timing peak in Figure 4.3. As in section 3, the energy spectra displayed are summed over the eleven NaI(Tl) detectors that form the inner ring of the NSCL γ -array. In the projectile frame ($\beta = 0.27c$) two photopeaks with centroids corresponding to γ -ray energies of approximately 2.5 MeV and 2.1 MeV are visible while in the laboratory frame ($\beta = 0$) these photopeaks disperse. These spectra indicate that the γ -rays producing the high energy peaks detected in the NSCL array were emitted by a source moving at beam velocity. There is also a large γ -ray energy region between 700 keV and 1.3 MeV that contains a majority of the spectral counts. However, this energy range does not resolve into distinct photopeaks in either the projectile frame ($\beta = 0.27c$) spectrum or the laboratory frame ($\beta = 0$) spectrum. The detected photons that give rise to the counts in this energy region are most likely due to 938 keV de-excitation photons emitted from isomeric ^{18}F beam nuclei ($\beta = 0.27c$) decaying in flight. These in-flight decay photons will be discussed at length in section 4.3.4 and chapter 5.

4.3.2 The Coulomb Excitation of $^{18}\text{F}_{\text{g.s.}}$

The two distinct photopeaks observed in the projectile-frame spectrum of Figure 4.5 can be assigned to $^{18}\text{F}_{\text{g.s.}}$ Coulomb excitations. The photopeak at 2.1 MeV likely corresponds to a $E1$ de-excitation of the 2101 keV ($J^\pi = 2^-, T_{1/2} = 3.5 \pm 4$ ps) excited state in

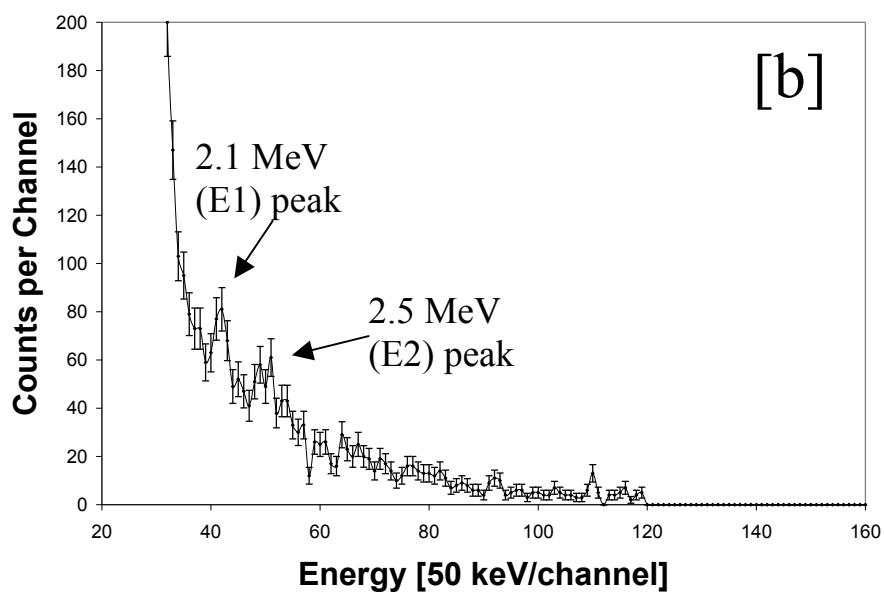
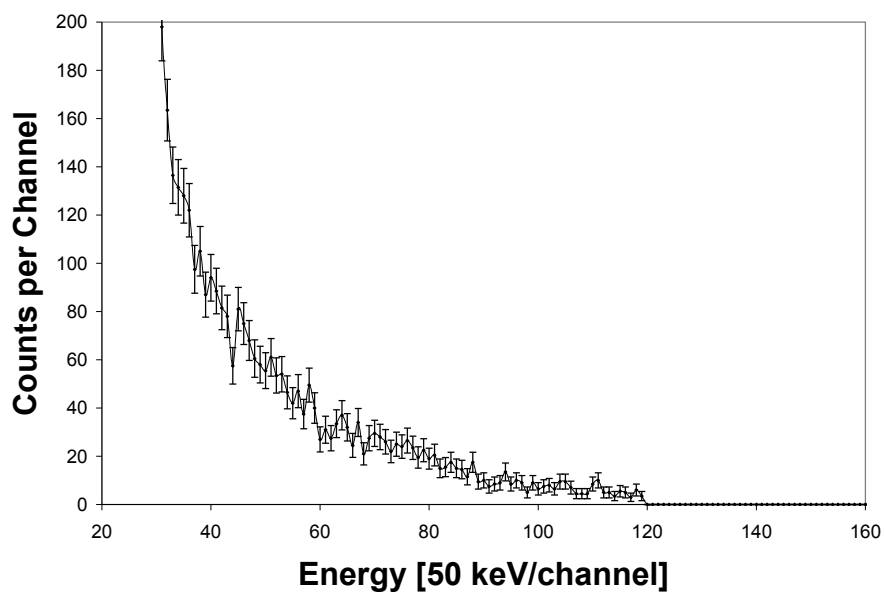


Figure 4.5: Raw energy [a] and Doppler-corrected [b] energy spectra for the ^{18}F Coulomb excitation data. Note the excitation photopeaks in the projectile ($\beta = 0.27c$) frame that dissipate in the laboratory frame ($\beta = 0$).

^{18}F to the 1^+ ground state. The width of the 2.1 MeV photopeak was measured to be 142 keV (7% FWHM). The experimentally-identified photon energy falls within the energy calibration range of the NSCL, and one can confirm that a FWHM width of 7% at 2.1 MeV agrees well with the predicted energy resolution deduced during the energy calibration of the NSCL array (see section 2.2.4). The photopeak at 2.5 MeV can be assigned to a $E2$ transition from the 2523 keV ($J^\pi = 2^+$, $T_{1/2} = 409 \pm 17$ fs) excited state to the 1^+ ground state. Assuming classical hyperbolic Rutherford trajectories, one can calculate the minimum impact parameter between the ^{197}Au excitation target and the ^{18}F nuclei to be approximately 17 fm. This is about 6 fm larger than the distance between the centers of the ^{197}Au target and the ^{18}F projectile assuming touching spheres. In this case and at these distances, one can assume that nuclear contributions to the reaction cross section at the forward angles covered by the zero-degree detector are likely negligible. This assures, along with the timing cut on Figure 4.3, that these photons detected in the NSCL array are probably due to Coulomb excitation events.

Again, by including all eleven inner ring detectors in the final analysis of the ^{18}F ground state beam excitations, we were able to accumulate 89 ± 24 counts in the background-subtracted 2.1 MeV photopeak and 47 ± 17 counts in the background subtracted 2.5 MeV photopeak in approximately nineteen hours. The final value and quoted uncertainties for the background-subtracted peaks take into account the statistical uncertainties (added in quadrature) of three independent fits to the spectra summed over the eleven inner ring detectors. Table 4.1 displays the data gathered from the three fits of the background-subtracted peaks.

Table 4.1: Fits of the 2.1 MeV photopeak and the 2.5 MeV photopeak due to the Coulomb excitation of ^{18}F ground state beam fragments.

<i>Fit</i>	<i>Photo Peak Energy (keV)</i>	<i>Background - Subtracted Area</i>	<i>Background - Subtracted Area Uncertainty</i>	<i>Width FWHM keV</i>	<i>Width FWHM keV Uncertainty</i>	<i>Chi square/D.o.F.</i>
1 (2.1 MeV)	2084(18)	88	34	141	34	1.46
2 (2.1 MeV)	2083(19)	89	35	143	37	1.55
Average (2.1 MeV)	2084(13)	89	24	142	25	--
1 (2.5 MeV)	2505(29)	47	24	146	34	1.46
2 (2.5 MeV)	2506(29)	47	24	147	37	1.55
Average (2.5 MeV)	2506(20)	47	17	147	25	--

As before, one can employ the Coulomb-excitation equation 3-1 to arrive at the Coulomb excitation cross section values for the $^{18}\text{F}_{\text{g.s.}}$ excitations. Using the average of two statistical fits to the experimentally-determined area of the 2.1 MeV photopeak (89 ± 24 events) and adding their uncertainties in quadrature, we extract a Coulomb cross section of (2.2 ± 0.6) mb for the 2.1 MeV $^{18}\text{F}_{\text{g.s.}}$ Coulomb excitation. Assuming pure first-order Coulomb excitation (see Appendix A), we extract the reduced “up” transition strength, $B(E1 \uparrow)$ of $2.5 \cdot 10^{-3} \pm 0.7 \cdot 10^{-3} \text{ e}^2\text{fm}^2$ for the Coulomb excitation of ^{18}F nuclei from a 1^+ ground state to the 2^- 2101 keV excited state from the measured Coulomb-excitation cross section.

Using the average of two statistical fits to the experimentally-determined area of the 2.5 MeV photopeak (47 ± 17 events) and adding their uncertainties in quadrature, we obtain a Coulomb cross section of (1.2 ± 0.5) mb for the 2.5 MeV $^{18}\text{F}_{\text{g.s.}}$ Coulomb excitation and extract the reduced “up” transition strength, $B(E2 \uparrow)$ of $4.0 \pm 1.5 \text{ e}^2\text{fm}^4$ for the Coulomb excitation of ^{18}F nuclei from the 1^+ ground state to the 2^+ 2523 keV excited state.

The quoted uncertainties take into account the statistical error, the uncertainty from the background subtraction, the uncertainty due to the efficiency calibration, as well as the uncertainty introduced by correcting for the photon absorption in the target. The individual uncertainties listed in Table 4.2 were added in quadrature to arrive at the uncertainty in the total cross section.

Table 4.2: Sources of uncertainty included in the final error calculated for the ^{18}F ground state Coulomb cross section value.

<i>Projectile Excitation</i>	<i>Statistical [%]</i>	<i>Fit/ Background [%]</i>	<i>Efficiency [%]</i>	<i>Absorption [%]</i>	<i>Total Uncertainty [%]</i>
^{18}F (E1) (2.1 MeV)	27	8	4	7	29
^{18}F (E2) (2.5 MeV)	36	8	4	7	38

Our $B(E\lambda)$ value has been compared to the transition strength deduced from lifetime measurements, with the comparisons listed in Table 4.3 (see Appendix B).

Table 4.3: Comparison of experimental and theoretical $B(E\lambda\uparrow)$ values for ground-state ^{18}F Coulomb excitations.

<i>Transition</i>	<i>Reference</i>	<i>Excitation Beam</i>	<i>E_{lab} [MeV/nucleon]</i>	<i>$B(E\lambda)$ [$e^2\text{fm}^2$]</i>
$^{18}\text{F}_{g.s.}$ E1 2.101 MeV	This Expt.	^{18}F	40	$2.5 \cdot 10^{-3} \pm 0.7 \cdot 10^{-3} e^2\text{fm}^2$
E1 Adopted*	Lifetime*	-	-	$2.0 \cdot 10^{-3} \pm 0.3 \cdot 10^{-3} e^2\text{fm}^2$
$^{18}\text{F}_{g.s.}$ E2 2.523 MeV	This Expt.	^{18}F	40	$4.0 \pm 1.5 e^2\text{fm}^4$
E2 Adopted†	Lifetime†	-	-	$3.4 \pm 0.6 e^2\text{fm}^4$

* Based on the measured decay lifetime of 5.1 ps.

† Based on the measured decay lifetime of 590 fs.

The measured reduced transition strength $B(E1\uparrow)$ for the 2.1 MeV Coulomb excitation of the $^{18}\text{F}_{g.s.}$ agrees well with the value calculated from the experimentally-determined half-life of the 2101 keV transition. An exhaustive literature search indicated that our value is the first experimental measurement of the $B(E1\uparrow)$ reduced transition strength for the Coulomb excitation to the 2101 keV $J^\pi = 2^-$ level in ^{18}F .

The measured reduced transition strength $B(E2\uparrow)$ for the Coulomb excitation to the 2.5 MeV $^{18}\text{F}_{\text{g.s.}}$ also agrees quite well within the range predicted by the experimentally-determined lifetime of the 2523 keV transition. This is the first direct measurement of this reduced transition strength, and the measured value for the $B(E2\uparrow)$ was found to be in excellent agreement with the strength predicted from the known decay lifetime. The individual γ -ray intensities for photons produced in the decay of the 2.5 MeV excited state carry an uncertainty of $\sim 5\%$. This leads to a branching ratio (the probability ratio of gamma-ray intensities for all photons produced in the decay of a nuclear excited state) uncertainty for the 2.5 MeV excited state of $\sim 9\%$. The experimentally measured lifetime of the 2.5 MeV excited state carries an uncertainty of $\sim 5\%$.

In conclusion, we have made the first experimental measurement of the reduced transition strength for two ^{18}F ground state transitions using intermediate-energy Coulomb excitation. The adopted value for the $B(E1\uparrow)$ transition from the $^{18}\text{F}_{\text{g.s.}}$ ($J^\pi = 1^+$) to the 2101 keV ($J^\pi = 2^-$) excited state is $2.5 \cdot 10^{-3} \pm 0.7 \cdot 10^{-3} \text{ e}^2\text{fm}^2$ while our adopted value for the $B(E2\uparrow)$ transition from the $^{18}\text{F}_{\text{g.s.}}$ ($J^\pi = 1^+$) to the 2523 keV ($J^\pi = 2^+$) excited state is $4.0 \pm 1.5 \text{ e}^2\text{fm}^4$. Both of the experimentally determined values agree with the predicted transition strengths predicted from the measured decay lifetimes.

4.3.4 The Coulomb excitation of $^{18}\text{F}^{\text{m}}$.

A goal of this work is to look for the Coulomb excitation of $^{18}\text{F}^{\text{m}}$. Along with the photopeaks attributed to the Coulomb excitation of $^{18}\text{F}_{\text{g.s.}}$ beam nuclei, care was taken to examine the spectra displayed in Figure 4.5 for Doppler-corrected photopeaks caused by Coulomb excitations of isomeric $^{18}\text{F}^{\text{m}}$ beam nuclei. Previous experiments have used nuclear decay methods to populate collective nuclear levels above the $J^\pi = 5^+$ isomeric state in ^{18}F . These experiments have used this decay information to accurately determine

the excited-state energy and spin as well as the lifetime of the individual states. This information has allowed us to predict the most probable transition channels between the isomeric state and collective states built above the 1.1 MeV isomer. These are listed in Table 4.4.

Table 4.4: Excited ^{18}F nuclear states containing probable E2 transition channels to the $^{18}\text{F}^m$ state.

<i>Excited State Energy [keV]</i>	<i>Spin (J) and Parity(π)</i>	<i>Energy of $^{18}\text{F}^* - ^{18}\text{F}^m$ transition [keV]</i>	<i>Experimentally determined lifetime of $^{18}\text{F}^* - ^{18}\text{F}^m$ transition</i>	<i>Predicted $B(E2 \uparrow)$ transition strength* [$e^2\text{fm}^4$]</i>
4652	4+	3530	12.1 fs	100.5 $e^2\text{fm}^4$
5298	4+	4176	301 fs	1.2 $e^2\text{fm}^4$
4116	3+	2995	NA [†]	NA
3358	3+	2237	NA [†]	NA

**deduced from experimentally-determined E2 transition lifetimes.*

†experimental transition lifetimes not available.

Photopeaks from the expected transitions listed in Table 4.4 were not visible in the Doppler-corrected γ -ray spectra accumulated during the $^{18}\text{F}^m$ runs. Due to the relatively poor resolution of the NaI γ -array at these excitation energies and the limited statistics due to low isomer production, photopeaks from very weak Coulomb excitation transitions could not accumulate enough statistics to be distinguished from the normal high-energy γ -ray background. The upper level limits for the experimentally-determined reduced transition strengths $B(E2 \uparrow)$ of Coulomb excitations from the isomeric 5^+ state to the collective states listed in Table 4.4 were calculated using the intrinsic energy resolution of the γ -array at the energies in question. Our findings are presented in Table 4.5.

Table 4.5: Experimentally determined upper-level limits for the measured transition strengths $B(E2\uparrow)$ of $^{18}\text{F}^m$ Coulomb excitations.

<i>Excited State Energy [keV]</i>	<i>Energy of $^{18}\text{F}^* - ^{18}\text{F}^m$ transition [keV]</i>	<i>Predicted $B(E2\uparrow)$ transition strength* [$e^2\text{fm}^4$]</i>	<i>$B(E\lambda\uparrow)$ Limit [$e^2\text{fm}^4$]</i>
4652	3530	100.5 $e^2\text{fm}^4$	$\leq 17 e^2\text{fm}^4$
5298	4176	1.2 $e^2\text{fm}^4$	$\leq 3 e^2\text{fm}^4$
4116	2995	NA [†]	$\leq 12 e^2\text{fm}^4$
3358	2237	NA [†]	$\leq 22 e^2\text{fm}^4$

*deduced from experimentally determined E2 transition lifetimes.

†transition lifetimes not available.

The upper limits for the measured reduced transition strength $B(E2\uparrow)$ listed in Table 4.5 are the values for Coulomb-excitation transitions deduced from our experimental γ -ray data. The relatively short (~ 24 h) irradiation time and the intrinsic NaI(Tl) detector resolution at the relatively high transition energies made detection of low-probability Coulomb excitations difficult to quantify. Currently, Professor Glasmacher's group at NSCL, who were the principal collaborators on this experiment, are constructing a segmented Germanium large-angle detector array that will improve the intrinsic energy resolution of the array by a factor approaching two orders of magnitude (e.g. from 100-200 keV to 1-10 keV at $E_\gamma = 1-4$ MeV.). While the detection efficiency of the new array will be less than the efficiency of the current NaI(Tl) array, the large improvement in detector resolution should allow future measurements with the $^{18}\text{F}^m$ system. Recent simulations for measurements that can be made with the segmented Ge array indicate the ability to identify weak Coulomb excitation photopeaks to a precision of 10% with, also, a substantial reduction in the required beamtime. A re-measurement of the $^{18}\text{F}^m$ isomeric Coulomb excitations with the segmented Ge array is therefore being considered for the near future.

4.3.5 The in-flight decay of $^{18}\text{F}^m$ nuclei

In this section, we discuss the production of gamma-rays with energies of 184 keV and 938 keV due to the spontaneous decay of $^{18}\text{F}^m$ ($T_{1/2} = 162$ ns) nuclei. A large portion of the energy spectrum collected to identify the Coulomb excitation of ^{18}F nuclei contains counts from photons emitted during the in-flight decay of ^{18}F nuclei in the 5^+ isomeric state. This is due to the unusual situation that the beam particle of interest ($^{18}\text{F}^m$) exists in an unstable excited state that de-populates through a two-step gamma-ray cascade. These two photons, with energies of 184 keV and 938 keV are emitted in rapid succession by the decay of a single nucleus moving at a significant fraction of the speed of light ($\beta = 0.27c$). The emission of this gamma-ray cascade can occur at any time after the production of the original excited state $^{18}\text{F}^m$ nucleus in the A1200 magnet (but typically with a half-life of 162 ns in the ^{18}F frame of reference). A simplified ^{18}F level scheme illustrating the de-excitation photon cascade from the 5^+ ^{18}F isomeric state to the 1^+ ground state is displayed in Figure 4.6.

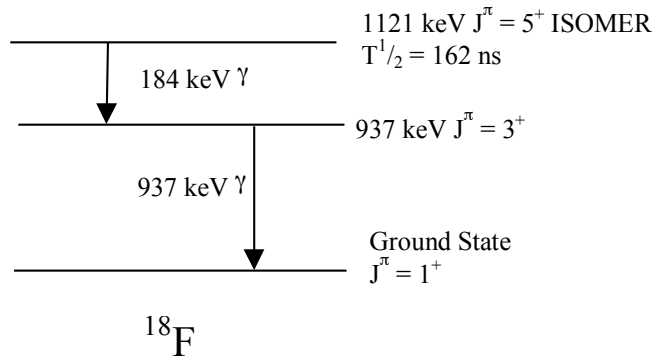


Figure 4.6: A simplified level scheme for ^{18}F . Two photons, with energies of 184 keV and 938 keV are emitted in rapid succession by the decay of a single $^{18}\text{F}^{\text{m}}$ nucleus moving at a significant fraction of the speed of light ($\beta = 0.27c$).

When $^{18}\text{F}^{\text{m}}$ in-flight decays of this nature occur in the vicinity of the NSCL large-angle γ -array, the de-excitation photons will be detected by the array with a known, high efficiency (calculated from our efficiency calibration) and will appear in our energy spectrum. However, these in-flight decay events happen at random times, making the exact location of the γ -ray emission impossible to specify. This eliminates the ability of our Doppler-correction to accurately arrive at the original energy (see Appendix C) of the emitted photon. This ambiguity in terms of the photon energy leads to a broad collection of counts due to the isomeric de-excitation γ -rays in the collected energy spectrum. The large number of particle de-excitations that occur in the vicinity of the NSCL array over the course of the data-collection period will mask any true Coulomb-excitation event that emits a photon in the same energy range as the in-flight $^{18}\text{F}^{\text{m}}$ decays. For this reason, we cannot measure any collective Coulomb excitations from the 5^+ isomeric state in ^{18}F that would be identified by an emitted photon detected by the γ -array in the energy region from 500 keV to 1400 keV. This deficiency in our experiment is not fatal due to the de-

excitation energies of the most probable collective levels built above the ^{18}F isomer being well above this masked energy region (*i.e.* in an energy region with a very low radiation background (see Table 4.5)).

While these isomeric de-excitation gamma-rays detected in the energy region from 500 to 1400 keV do mask possible low-energy $^{18}\text{F}^{\text{m}}$ Coulomb excitations, they also contain some interesting and unexpected information on the in-flight decay of the isomeric state in ^{18}F nuclei. This information will be presented in the next chapter.

CHAPTER 5

FUTURE OUTLOOK: POSSIBLE ACCELERATED EMISSION OF GAMMA RAYS FROM THE 162-NS ^{18}F ISOMER INDUCED BY COULOMB INTERACTION IN NUCLEI

5.1 Introduction

The use of time-dependent electric fields to excite a nucleus from its ground state to an excited state via Coulomb excitation is one of several methods currently used by nuclear scientists to populate excited nuclear states of interest. Two exciting methods have recently received a large amount of attention (and funding). Due to the recent progress in high-intensity laser sources, the possibility of populating excited nuclear states by coupling a nuclear ground state to an atomic electron system perturbed by a laser field is becoming an interesting area of research [Har99,Mat98]. Another exciting area of current research involves the accelerated emission of isomeric gamma-rays induced by the interaction of the isomer with low-energy electromagnetic radiation [Bro95, Irw97, Col99]. These two areas of future research will be discussed in the following sections along with evidence of accelerated isomeric gamma-ray emission in $^{18}\text{F}^m$.

5.2 Nuclear Excitation via Laser Perturbation

The idea of creating a nuclear γ -ray laser based on a nuclear γ -transition has been discussed for several years. In order to create such a device, an efficient mechanism for populating nuclear excited states must be found [Bal98]. To this end, experimenters have

been studying low-energy nuclear isomeric states in hopes of uncovering an reliable excitation method with a large excitation cross section. Harston and Chemin [Har99] have evaluated several experimental attempts to induce a nuclear excitation in ^{235}U , from the ground state ($J^\pi = 7/2^+$) to an isomeric state ($J^\pi = 1/2^+$) lying 77 eV above the ground state using lasers. Figure 5.1 displays the low-energy nuclear states of ^{235}U .

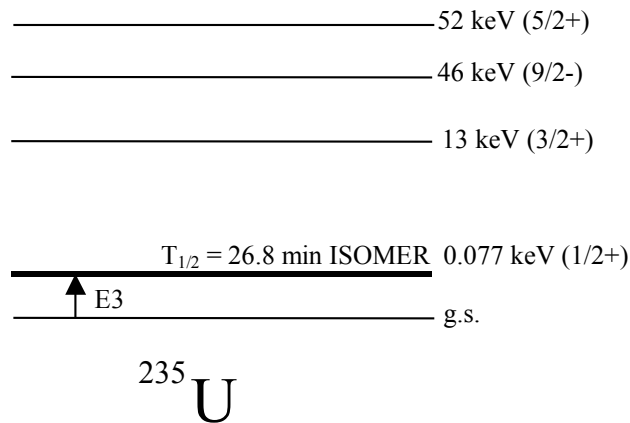


Figure 5.1: Low-lying nuclear levels of ^{235}U .

The first published experiment of this type to claim an excitation to the $^{235}\text{U}^m$ state was performed by Izawa and Yamanaka [Iza79] using a CO_2 laser focused on a U_{nat} target. By detecting conversion electrons from the decay of the 77 eV isomeric state having a characteristic decay rate matching the 26.8 m half-life of the state, the researchers deduced an excitation cross section of $\sim 10^{-29} \text{ cm}^2$. These experiments were followed by similar experiments by Arutyunyan *et al.* [Aru89] in the following decade. Arutyunyan used a higher-power CO_2 laser to create an electron plasma suitable for nuclear excitation of the ^{235}U ground state nuclei, but could not detect the conversion electrons indicating the isomeric excitation [Aru89]. Later, Arutyunyan *et al.* used a 500 keV electron beam to induce the isomeric excitation and calculated an excitation cross section of $\sim 10^{-32} \text{ cm}^2$ [Aru91]. An improvement on these low excitation cross sections

have been achieved by Bounds and Dyer [Bou92] by using a low-power CO₂ laser to create a suitable electron plasma, then excite the plasma with a second high-intensity laser which produced a reported upper limit for the nuclear excitation probability of $4.0 \cdot 10^{-5}$ per 700 fs pulse.

There are several reasonable mechanisms that could be used to describe the process of nuclear excitation evident in these experiments. Various excitation mechanisms have been hypothesized in the literature, virtually eliminating a consensus on the correct excitation mechanism. Harston and Chemin discuss several of these mechanisms with the most probable mechanisms being nuclear excitation by electron transition (NEET), laser-assisted NEET, and nuclear excitation by electron capture (NEEC). Figure 5.2 displays Feynman diagrams for these three nuclear excitation mechanisms.

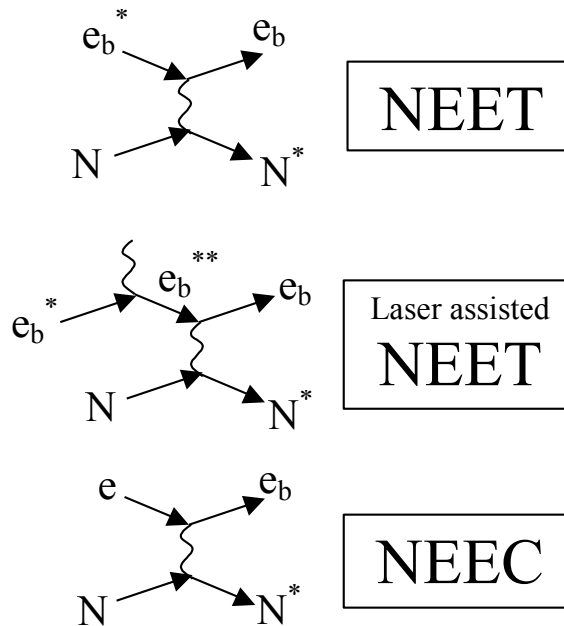


Figure 5.2: Feynman diagrams for three nuclear excitation mechanisms; NEET, laser-assisted NEET and NEEC. N indicates the nuclear ground state, N^* indicates a nuclear excited state, e represents a free electron (or continuum electron), e_b represents an electron in a bound orbital, and the curved line represents an electromagnetic interaction.

Both NEET and laser-assisted NEET occur through a process of exciting a nucleus through a simultaneous de-excitation of the surrounding atomic electrons. This can be visualized as the opposite of a nuclear internal conversion (IC) where a nucleus de-excites by promoting a bound atomic electron to an excited atomic state. This process can only take place when the energy difference in the electron atomic levels is similar to the energy difference in the nuclear levels involved in the excitation. A group of Japanese experimenters have reported the existence of NEET [Sai80,Fuj84] , however Harston notes that the validity of their findings have been brought into question by researchers claiming that a significant portion of the reported NEET excitation was caused by Bremsstrahlung x-ray photoexcitation [Lak95].

NEEC occurs by a process of exciting a nucleus through the capture of a free (or continuum) electron into an orbiting bound atomic state. This can also be visualized as the opposite of a typical nuclear internal conversion but where a nucleus decays by ejecting an atomic electron from the potential well of the nucleus. Generally, a large number of atomic orbitals can participate in an NEEC mechanism. If the energy of the captured free electron E satisfies the condition that the binding energy E_b of the bound electron after capture is less than the energy of the nuclear excitation E_n , then the excitation condition $E = E_n - E_b$ will be satisfied for a large number of electron orbitals as long the free electron comes from an electron system with a wide range of electron energies which is typical for these reactions. The NEEC process has been considered for describing the excitation of several isomers through a process of resonant transfer excitation in which an electron in a solid target is captured into a bound orbital of a projectile nucleus [Cue89].

Experiments continue to explore nuclear excitation using NEET and NEEC mechanisms, however they are limited in scope and excitation energy. Realistic excitation energies due to these procedures are limited to the eV and low keV regions, far below the excitation energy needed to induce excitation from the $^{18}\text{F}^m$ ($J^\pi = 5^+$) excited

state (see section 4.3.4). The following section will describe excitation mechanisms for inducing the emission of isomeric gamma-rays and present data describing the phenomenon as it pertains to the $^{18}\text{F}^m$ nucleus.

5.3 Induced Emission of Isomeric Gamma-Rays

In addition to scientific interest in the ability to populate isomeric states in nuclei discussed in section 5.2, as noted there is also an area of exploration involving the forced de-excitation of nuclear isomers. A recent example that demonstrates this phenomenon involves the ^{178}Hf ($J^\pi = 16^+$, $t_{1/2} = 31\text{y}$) 2.446 MeV isomer and will be discussed in this section. The long half-life of this isomer, unlike $^{18}\text{F}^m$, allows it to be formed into a nuclear target which can be studied in detail using a variety of techniques.

A large majority of nuclear excited states can populate lower nuclear states through the emission of a γ -ray. The gamma-ray must have the precise energy to balance the energy difference between the interacting states, as well as exhibit electromagnetic characteristics to match the difference between the spins (J) and parities (π) of the nuclear levels involved in the transition. As the spin difference between the transitional states decreases and the energy difference between the states increases, the lifetime of the excited state decreases. The excited state lifetime is on the order of femtoseconds ($=10^{-15}$ s) to picoseconds ($=10^{-12}$ s) for relatively small spin differences and large excitation energies. As discussed previously, nuclear isomeric states are excited nuclear states that exhibit unusually long lifetimes when compared to other nuclear excited states of similar energy. The result is a long-lived metastable state that for radioactive nuclei can have a longer lifetime than the corresponding ground state (see section 1.5).

Recent research on the radioactive nucleus ^{178}Hf has suggested the existence of an accelerated emission of the 31-y 2.446 MeV isomeric state due to x-ray irradiation [Col99]. This group of researchers have irradiated a small sample of $^{178}\text{Hf}^m$ with an x-ray

device typically used in dental medicine. This device produced Bremsstrahlung radiation with an end-point energy of 70 or 90 keV. Collins *et al.* claim to have observed a 4% increase in the intensities of selected transitions found in the decay cascade of the ^{178}Hf isomer. This increased isomer gamma-ray production is attributed to the promotion of the isomer via x-ray irradiation to a level with spin characteristics that favor de-excitation through γ -ray production. In examining the level scheme of ^{178}Hf displayed in Figure 5.3, one can see a structure typical of the deformed nuclei in this mass region. Two distinct bands of nuclear excited states dominate the level scheme of ^{178}Hf : a low-energy band of rotational states and a high-energy band of states in the energy region of the $J^\pi = 16^+$ isomeric state. The large spin difference between the positive parity states in the low-energy rotational band forbid transitions connecting these low-energy states to the high-energy isomeric state. The excited nuclear states energetically similar to the isomeric state are negative in parity and relatively low in spin when compared to the isomeric state. These level characteristics inhibit isomeric decay transitions to both the low-energy rotational levels and the high-energy negative parity levels, leading to the extremely long 31-year half-life of the isomeric state. By promoting the isomeric nuclei to a state that can couple strongly with the high-energy negative-parity states surrounding the isomer, nuclei could avoid the long decay lifetimes associated with the isomeric state and de-excite following the normal spontaneous decay pathways.

The data published by Collins *et al.* suggest that x-ray irradiation of the ^{178}Hf isomer promoted a fraction of the isomeric nuclei to an energetically higher (40 ± 20 keV) nuclear level with mixed spin characteristics [Col82]. Levels of this type have been previously found in neighboring nuclei such as ^{180}Ta [Col88] and ^{174}Hf [Wal97]. Collins reported the de-population of the mixed-character state following the normal ^{178}Hf spontaneous decay pathways beginning at the 11^- excited nuclear state. The experimental data indicates a $6.3 \pm 2.2\%$ enhancement in the 495 keV ($11^- \rightarrow 9^-$) γ -ray and a $2.0 \pm 1.3\%$ enhancement in the 495 keV ($8^+ \rightarrow 6^+$) γ -ray while reporting no enhancement in the 574

keV ($13^- \rightarrow 11^-$) γ -ray. As discussed below, the observation of such an enhancement is of particular interest due to the present experimental indication of an apparent enhancement in the production of ^{18}F isomeric gamma-rays due to Coulomb interaction with a ^{197}Au target.

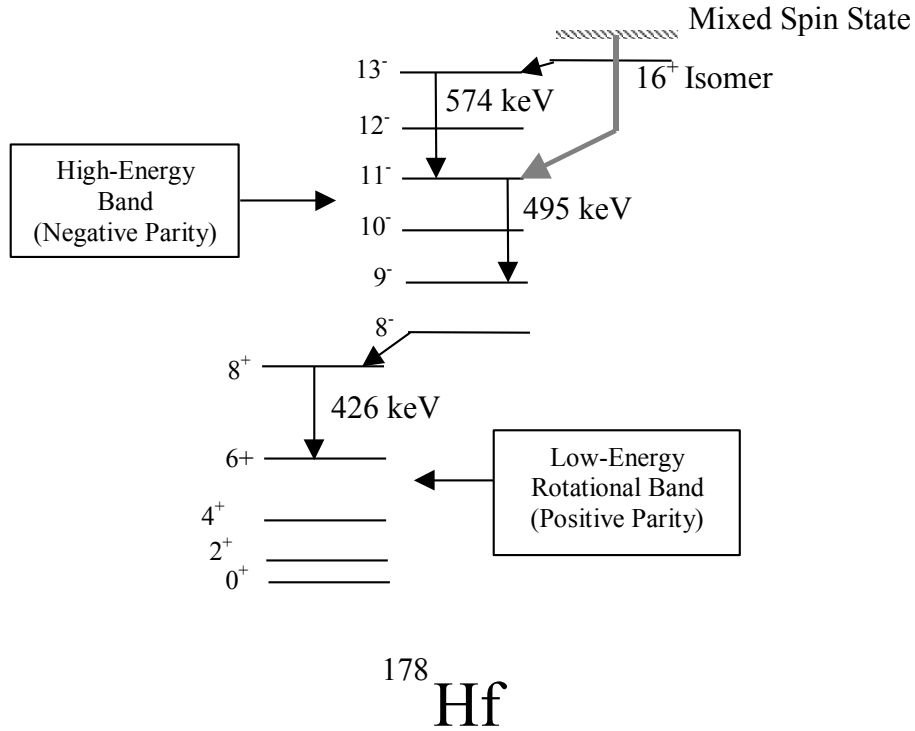


Figure 5.3: Simplified nuclear level scheme for ^{178}Hf . Energies of γ -ray transitions of interest are included.

5.4 Accelerated Emission of Gamma Rays from the 162-ns Isomer of ^{18}F

As noted in section 4.3.5, during the course of analyzing the ^{18}F experimental data, we detected a large number of photons due to the in-flight decay of $^{18}\text{F}^m$ nuclei. One can identify the number of decaying $^{18}\text{F}^m$ nuclei at various positions with respect to the physical position of the NSCL array by segmenting the timing peak due to isomeric gamma-rays detected in the NSCL large-angle array (Figure 4.3). Analysis of the

number of 184 keV-938 keV isomeric γ -ray cascades detected in the NSCL γ -array emitted in the vicinity of the ^{197}Au excitation target appear to indicate an accelerated isomeric photon emission due to an interaction with the ^{197}Au nuclei.

A raw-energy spectrum summed over the eleven NaI(Tl) detectors that form the inner ring of the NSCL γ -array containing detected isomeric γ -ray cascades was collected by requiring the detection of a E_i keV-938 keV γ -ray coincidence (where $E_i = 80$ to 2000 keV) occurring within a 88 ps-two channel transit-time cut. This was achieved by placing a software gate on the energy region containing counts due to Doppler-shifted 938 keV γ -rays (~ 800 -1200 keV - see appendix C) for each of the eleven inner-ring NaI(Tl) detectors. The firing of any of the eleven software gates coupled with the detection of a γ -ray in any of the inner-ring detectors within the 88 ps transit-time cut signified a detected γ -ray coincidence. Subsequently, the energy of each detected γ -ray in coincidence with a 938 keV γ -ray was added to the summed spectrum. The raw-energy γ -ray coincidence spectrum collected from the $^{18}\text{F}^m$ experimental data is presented in Figure 5.4.

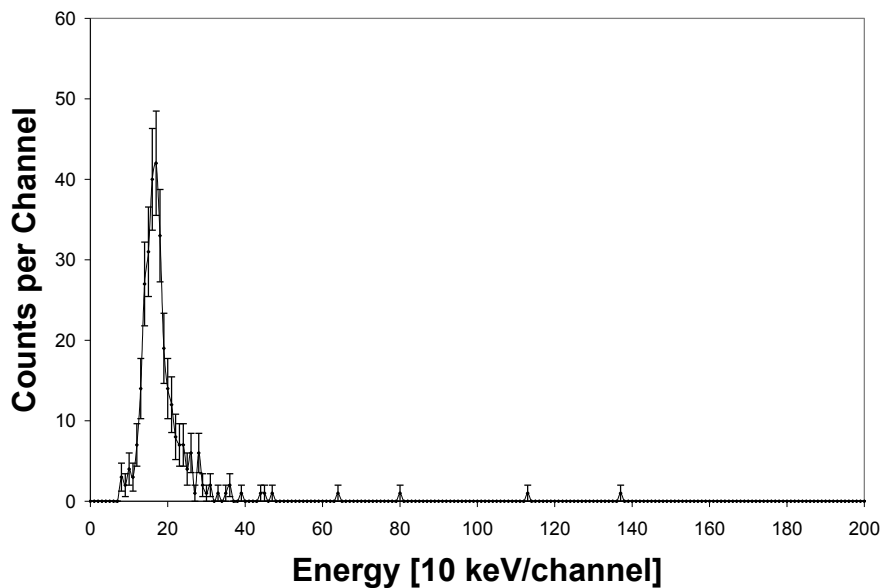


Figure 5.4: Raw-energy spectrum collected under the condition of detecting a 938 keV gamma-ray within a 88 ps transit-time window.

The spectrum displayed in Figure 5.4 clearly shows a photopeak corresponding to the expected 184 keV coincident γ -ray from the in-flight decay of $^{18}\text{F}^m$ nuclei. The observation of a single photopeak in coincidence with the 938 keV energy region is consistent with the known ^{18}F level scheme and the decay emissions of $^{18}\text{F}^m$.

The 184 keV and 938 keV γ -rays emitted in the $^{18}\text{F}^m$ decay are produced sequentially from a single nuclear decay and detected in the NSCL large-angle γ -array (see Figure 4.6). These spontaneous nuclear decays can occur at any time after the production of the $^{18}\text{F}^m$ secondary beam fragments at the primary ^{12}C production target located at dispersive image 2 of the A1200 fragment separator (see Figure 2.1). If a $^{18}\text{F}^m$ decay occurs in the vicinity of the NSCL large-angle array, the detection probability of the emitted photon can be determined using the measured detection efficiency of the NSCL large-angle array at the energy of the emitted photon. The detection probability of each isomeric decay photon in conjunction with information on the number of $^{18}\text{F}^m$ nuclei produced in the primary production reaction, coupled with the physical distance in which γ -rays emitted by beam projectiles can be detected by the large-angle array allows one to calculate the total number of expected isomeric 184 keV-938 keV gamma-ray cascades detected by the γ -array. One can deduce the number of expected $^{18}\text{F}^m$ isomeric γ -ray cascades *occurring at the excitation target position* detected by the NSCL large-angle array by accurately knowing the position of the ^{197}Au excitation target with regards to the NSCL γ -array timing spectrum (Figure 4.3) determined from timing spectra collected during the experiments described in chapter 3 (see Figure 4.4):

$$N_{\gamma-\gamma} = N_{F18} \cdot \frac{F^*}{F} \cdot \epsilon_{184} \cdot \epsilon_{937} \cdot \lambda_{tgt} \quad (5-1)$$

where ϵ_{184} and ϵ_{938} represent the detection efficiency of the NSCL large-angle array at photon energies of 184 keV and 938 keV respectively, N_{F18} designates the

number of ^{18}F nuclei detected in the ΔE v TOF particle identification spectrum (multiplied by the appropriate hardware down-scaling factor of 300 used to eliminate electronic dead time in the data acquisition system), F^*/F denotes the ratio of $^{18}\text{F}^m$ to $^{18}\text{F}_{\text{gs}}$ nuclei calculated from the data collected by the two HPGe detectors, and λ_{tgt} represents the number of $^{18}\text{F}^m$ nuclei decaying in the portion of the timing spectrum corresponding to the position of the excitation target.

The parameters needed in equation 5-1 to calculate $N_{\gamma\tau}$ are collected in several ways. The detection efficiencies ε_{184} and ε_{938} were calculated from efficiency calibration data discussed in section 2.2.5 with the adopted values listed in Table 5.1. A value of $17.5 \pm 1.1\%$ was obtained for the F^*/F ratio of $^{18}\text{F}^m$ nuclei to ^{18}F nuclei from the weighted average of Ge detector beam-purity data taken during the thick and thin ^{12}C production target runs (see section 2.2.1). Following the calculations discussed in chapter 4, the value for N_{F18} was taken directly from the number of ^{18}F nuclei identified by a software gate placed on the ΔE v TOF particle identification spectrum.

Table 5.1: Calculated NSCL large-angle γ -array detection efficiencies for $^{18}\text{F}^m$ isomeric decay photons.

<i>Photon Energy [keV]</i>	<i>Calculated NSCL γ-array Efficiency [%]</i>
184 keV	22.8(0.8)%
938 keV	11.1(0.4)%

To determine the final parameter λ_{tgt} needed to calculate a value for $N_{\gamma\tau}$, the timing peak corresponding to the isomeric photons detected in the NSCL γ -array was divided into segments two channels wide. We must now calculate the amount of time corresponding to two time channels in the NSCL γ -array timing spectrum. The speed of an ^{18}F particle was determined to be $0.2688c$. The distance from the excitation target (placed in the middle of the NSCL array) to the front face of the zero-degree detector (ZDD) was measured as 514.4 mm. The distance traveled by gamma-rays emitted by

$^{18}\text{F}^{\text{m}}$ nuclei decaying in the ZDD was measured as 516.4 mm (the distance from the front face of the ZDD to the NAI array). Based on the centroids of the in-flight decay photon timing peak (due to gamma-rays emitted by $^{18}\text{F}^{\text{m}}$ nuclei decaying in the ZDD) and the timing peak due to the interaction of beam particles with the front face of the zero degree detector, the ^{18}F nuclei with a velocity of $0.2688c$ plus the emitted γ -ray were calculated to have traversed 514.4mm and 520mm respectively in 186 timing channels. This data allows us to calculate a timing value for one channel:

$$\left(\frac{0.5144m}{0.2688 \cdot 2.99 \times 10^8 \frac{m}{s}} \right) + \left(\frac{0.5200m}{1 \cdot 2.99 \times 10^8 \frac{m}{s}} \right) = 8.14 \times 10^{-9} s \div 186 \text{channels} = 4.4 \times 10^{-11} \frac{s}{ch} = 44 \frac{ps}{ch}$$

The value of 44 ps/channel corresponds to a value of 88 ps for the two-channel experimental timing segments and can be used to calculate the number of $^{18}\text{F}^{\text{m}}$ ($T_{1/2} = 162$ ns) isomeric nuclei that will decay in the vicinity of the ^{197}Au excitation target λ_{tgt} :

$$\lambda_{F18} = \frac{\ln 2}{t_{1/2}} = \frac{\ln 2}{162 \times 10^{-9} s} = 4.279 \times 10^6 s^{-1}$$

$$\lambda_{\text{tgt}} = 1 - e^{-\lambda_{F18} t} = 1 - e^{-(4.279 \times 10^6 s^{-1})(8.8 \times 10^{-11} s)} = 3.765 \times 10^{-4}$$

Finally, the number of expected $^{18}\text{F}^{\text{m}}$ isomeric γ -ray cascades *occurring in the timing segment representing decays emitted at the excitation target position* detected by the NSCL large-angle array was calculated:

$$N_{\gamma-\gamma} = 300 \cdot 4.653 \times 10^6 \text{ part} \cdot 0.175 \frac{F^*}{F} \cdot 0.228 \cdot 0.111 \cdot 3.765 \times 10^{-4} = 2328$$

When the calculated isomeric decay yield is compared to the measured number of $^{18}\text{F}^{\text{m}}$ isomeric γ -ray cascades accumulated for each of the timing segments in the vicinity of the excitation target (displayed in Figure 5.5), one finds good statistical agreement. The number of detected in-flight isomeric decays (identified by the detection of the characteristic 184 keV-938 keV γ -ray cascade) agrees within statistics with the predicted value for the timing segments corresponding to areas within the large-angle array other

than the position of the excitation target. In contrast, a slight but significant 2σ increase in the number of coincidences was observed for the timing segment corresponding to the position of the excitation target (as calculated from the ^{197}Au Coulomb excitation data). One can eliminate the contribution of ground state E2 Coulomb excitations that populate the 938 keV ($J^\pi = 3^+$) excited state which would lead to an enhancement in the detection of the 938 keV γ -ray only by requiring the detection of both gamma-rays emitted in the decay of a single isomeric nucleus. The increased decay rate at the ^{197}Au target position is much greater than the contribution expected from ground state Coulomb excitation to the isomeric state (*i.e.* double excitations from the 1^+ ground state (E2) to the 938 keV 3^+ level followed by excitation (E2) from the 3^+ level to the 5^+ isomeric state) which is expected to be several orders of magnitude smaller than the observed enhancement. Therefore, we propose that this increase in isomeric coincidences is due to the interaction of the decaying $^{18}\text{F}^m$ projectile nuclei with the ^{197}Au target nuclei, most likely the Coulomb field of the latter.

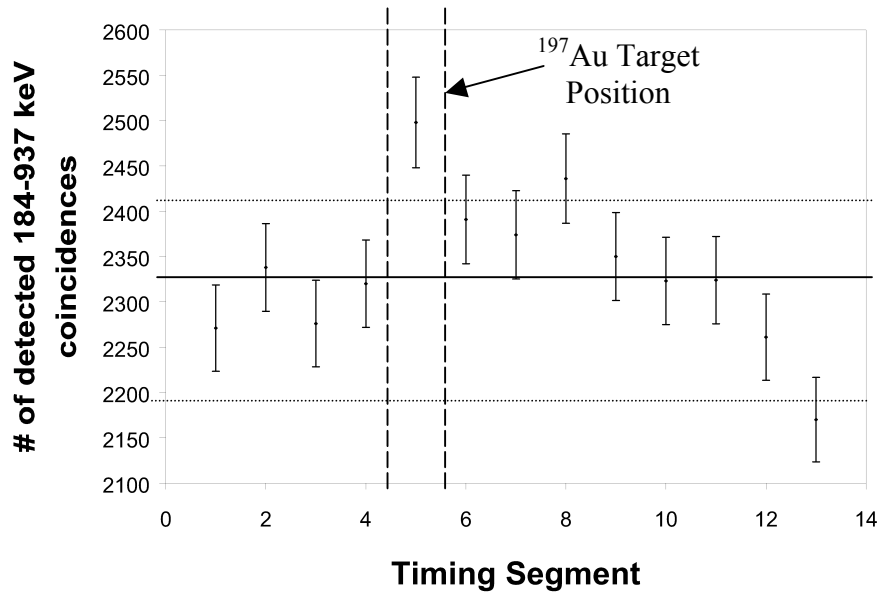


Figure 5.5: Observed number of coincidences due to the in-flight decay of isomeric ^{18}F nuclei. Each timing segment corresponds to a 88 ps transit-time window. The position of the ^{197}Au excitation target (denoted here by

vertical dashed lines) was determined from the ^{197}Au Coulomb excitation data presented in chapter 3. The horizontal line represents the predicted value for the number of detected isomeric decays, with the uncertainty in this value denoted by dashed horizontal lines [note offset scale].

Table 5.2 contains the experimental data collected on the number of observed coincidences for each 88 ps timing segment. From this information, we infer a decay life-time of ~ 160 ps and an accelerated isomeric decay of $\sim 7\%$.

Table 5.2: Experimental data collected on the number of observed 184 keV-938 keV isomeric coincidences for each 88 ps transit-timing segment.

<i>88 ps Transit Timing Segment</i>	<i>184 keV γ-ray Photopeak area</i>
01	2271
02	2338
03	2276
04	2320
05	2498
06	2391
07	2374
08	2436
09	2350
10	2323
11	2324
12	2261
13	2170

In order to confidently assign the accelerated isomer decay to the Coulomb interaction of $^{18}\text{F}^m$ isomeric nuclei with the time-dependent electric field of the ^{197}Au target nuclei, further research with $^{18}\text{F}^m$ beams or similar isomeric nuclei should be

performed. Additional study with the $^{18}\text{F}^m$ nucleus using the NSCL HPGe large-angle array currently under construction can return confirming information for the proposed isomer-decay acceleration mechanism. Another isomer of potential interest is the 616 keV $^{42}\text{Sc}^m$ isomer ($T_{1/2} = 61.7$ s) that has recently been produced as a pure radioactive isomeric beam and is being studied extensively at RIKEN [Uzu94, Kel94]. The UM-MSU group had also proposed studying an isomeric state in ^{39}Cl as part of this experiment, but the length of the $^{18}\text{F}^m$ study prohibited the approval of beam time for experiments with the chlorine nucleus and hence confirmation of the effect observed with $^{18}\text{F}^m$.

APPENDICES

APPENDIX A

COULOMB EXCITATION THEORY

The Coulomb excitation process can be evaluated using a semi-classical method developed by Winther and Alder [Win 79]. This method assumes classical hyperbolic Rutherford trajectories for the motion of the projectile, and assumes the excitation process can be explained using quantum-mechanical perturbation theory. This second assumption only holds for weak Coulomb excitations. The cross section for exciting a final state $|f\rangle$ from an initial state $|i\rangle$ is given by:

$$\frac{\delta\sigma}{\delta\Omega} = \left(\frac{\delta\sigma}{\delta\Omega} \right)_{Ruth} P_{i,f}(\theta)$$

(A-1)

The Rutherford cross section is expressed by:

$$\left(\frac{\delta\sigma}{\delta\Omega} \right)_{Ruth} = \frac{a_0^2}{4 \sin^4 \left(\frac{\theta}{2} \right)} \quad (\text{A-2})$$

here θ is the center-of-mass scattering angle and $2a_0$ is the distance of closest approach.

The quantity a_0 can be expressed as:

$$a_0 = \frac{Z_t Z_p e^2}{m_o c^2 \beta^2} \quad (\text{A-3})$$

where $Z_{t,p}$ is the atomic number of the target and projectile respectively, m_o is the reduced mass of the system, c is the speed of light, and $\beta = v/c$ where v denotes the velocity of the projectile. For reactions with energies below the Coulomb barrier of the system, the minimum impact parameter is achieved through axi-symmetric head-on collisions.

$P_{i,f}$ is defined as the probability to promote the nuclear ground state $|i\rangle$ to the excited state $|f\rangle$. For weak Coulomb excitation, this process can be expressed via time-dependent first order perturbation theory as :

$$P_{i,f} = |a_{i,f}|^2 \quad (\text{A-4})$$

where the transition amplitude $a_{i,f}$, not to be confused with a_o , can be defined as :

$$a_{if} = \frac{1}{i\hbar} \int_{-\infty}^{\infty} e^{i\omega_{fi}t} \langle f|V(r(t))|i\rangle dt \quad (\text{A-5})$$

In this case, $V[\mathbf{r}(t)]$ represents the time-dependent electromagnetic field which can be modeled using a Lienard-Wiechert potential. The energy-difference parameter of the two nuclear levels involved in the excitation process is denoted by ω_{fi} where :

$$\omega_{fi} = \frac{1}{\hbar}(E_f - E_i) \quad (\text{A-6})$$

One can expand the electromagnetic potential $V[\mathbf{r}(t)]$ in its multipole components $V_{\lambda\mu}[\mathbf{r}(t)]$, and express the transition amplitude $a_{i,f}$ in terms of the electric and magnetic multipole moments $M(E\lambda\mu)$ and $M(M\lambda\mu)$ respectively – or using a more general notation $M(\pi\lambda\mu)$ with:

$$a_{if} = i \sum_{\lambda} \frac{Z_t e \langle f|M(\pi\lambda\mu)|i\rangle}{\hbar c a_o^{\lambda}} f_{\lambda}(\xi) \quad (\text{A-7})$$

Here, $f_{\lambda}(\xi)$ is a function that depends on the adiabaticity parameter ξ which, for non-relativistic energies, is given by:

$$\xi = \omega_{fi} \tau_{coll} \quad (\text{A-8})$$

Here, τ_{coll} is the collision time, which is calculated using :

$$\tau_{coll} = \frac{a_o}{v} \quad (\text{A-9})$$

where v is the projectile velocity, and $2a_o$ is the classical distance of closest approach, given by equation A-3. For a value of the adiabaticity parameter $\xi > 1$, the collision is assumed to be adiabatic and the excitation probability falls exponentially with ξ . In order

for the excitation to satisfy this adiabatic condition, the possible excitation energies are limited to the range of 1-2 MeV if the adiabatic cutoff is assumed to be $\zeta \approx 1$.

For intermediate and relativistic energies ($\beta \gg 0$), equation A-8 needs to be slightly modified. For reactions with incident beam energies below the Coulomb barrier of the system, the distance of closest approach is reached using central projectile-target collisions. For higher incident beam energies, one can only consider pure Coulomb excitation reaction channels if the impact parameter b of the colliding system is larger than the sum of the radii of the colliding nuclei. In this case, one must also take the Lorentz contraction of the electromagnetic field into account. This contraction forces one to properly modify the equation describing the adiabaticity parameter (ζ) to account for the relativistic velocity :

$$\zeta = \omega_{fi} \tau'_{coll} = \omega_{fi} \frac{b}{v\gamma} \quad (\text{A-10})$$

where γ is the usual relativistic factor $\left(\gamma = \frac{1}{\sqrt{1-\beta^2}} \right)$. Due to the shorter collision time τ'_{coll} in intermediate and relativistic collisions, the adiabaticity parameter is smaller than in the previously-discussed non-relativistic collisions. Therefore, the maximum reachable excitation energy is correspondingly larger at higher incident beam energies.

One can now describe the partial Coulomb cross section for exciting a state $|i\rangle$ with a λ -pole excitation (eg E1, M1, E2,...) as :

$$\sigma_{\lambda} = 2\pi \int_{b_0}^b b_{adiab} \left| \frac{Z_T e \langle f \| M(\pi\lambda\mu \| i) \rangle}{\hbar c b^{\lambda}} \right|^2 b db \quad (\text{A-11})$$

where the lower integration limit is the minimum impact parameter, given by the sum of the two nuclear radii, and the upper integration limit is given by the impact parameter at

which the adiabaticity parameter ζ (see equation A-8) is equal to unity (adiabatic cutoff). This integral can be evaluated using first order time-dependent perturbation theory. A detailed discussion on this subject can be found in [Win79], and goes well beyond the scope of this thesis. Therefore, we only quote the final result, which relates the Coulomb excitation cross section to the reduced electric transition strength $B(\pi\lambda)$, through the following equation :

$$\sigma_{coul} = \left(\frac{Z_T e^2}{\hbar c} \right)^2 \sum_{\pi\lambda\mu} k^{2(\lambda-1)} \frac{1}{e^2} B(\pi\lambda) \left| G_{\pi\lambda\mu} \left(\frac{v}{c} \right) \right|^2 g_{\mu}(\zeta(b_{\min})) \quad (\text{A-12})$$

where the functions $G_{\pi\lambda\mu}$ are tabulated in [Win79], and the functions $g_{\mu}(\zeta)$ relying on the adiabatic parameter ζ can be expressed via the modified Bessel functions (K_{ν}) :

$$g_{\mu}(\zeta) = g_{-\mu}(\zeta) = \pi\zeta^2 \left[|K_{\mu+1}(\zeta)|^2 - |K_{\mu}(\zeta)|^2 - \frac{2\pi}{\zeta} K_{\mu+1}(\zeta)K_{\mu}(\zeta) \right] \quad (\text{A-13})$$

In the case of the Coulomb excitation of ^{18}F , we are interested in an electric quadrupole transition ($\lambda = 2$) to a high-energy collective excited state from the 5^+ isomeric state.

Therefore, the general equation relating the Coulomb excitation cross section can be simplified to :

$$\sigma_{coul} = \left(\frac{Z_T e^2}{\hbar c} \right)^2 \frac{16\pi k^2 B(E2 \uparrow)}{9e^2} \left[g_1(\zeta) + (1 - \beta^2) g_0(\zeta) \right] \quad (\text{A-14})$$

It should be noted that the adiabaticity parameter ζ is specific to each experiment, as it depends on the beam energy, and on the minimum impact parameter (b_o) which is a direct result of the particle identification detector configuration. One can calculate the minimum impact parameter as follows :

$$b_o = \frac{a_o}{\gamma} \cot\left(\frac{\theta_{\max}}{2}\right) \quad (\text{A-15})$$

In calculating b_o , a_o is given by equation A-3, γ is the relativistic parameter detailed above, and the center-of-mass maximum scattering angle θ_{max} is given by the experimental setup ($\theta_{max} = 5.6^\circ$ for this experiment).

APPENDIX B

NUCLEAR TRANSITION MATRIX ELEMENTS FOR ELECTRIC QUADRUPOLE TRANSITIONS

This appendix will describe how to deduce the reduced electronic transition strength $B(E\lambda)$ -where λ denotes the multipolarity of the transition- from the measured lifetime of the state. Many intermediate steps in the derivation are left out, and for a more detailed description of this subject, the interested reader should refer to texts such as [Won90].

The mean lifetime of a transition T , the half-life $T_{1/2}$ and the transition probability P are related via:

$$T = \frac{T_{1/2}}{\ln 2} = \frac{1}{P} \quad (\text{B-1})$$

As mentioned in Appendix A, for weak interactions one can use first order time-dependent perturbation theory to derive Fermi's golden rule. This condition relates the transition probability P to the square of the nuclear interaction matrix element M_{fi} :

$$P = \frac{2\pi}{\hbar} \left| \langle J_f M_f \xi | H' | J_i M_i \xi \rangle \right|^2 \rho(E_f) \quad (\text{B-2})$$
$$P = \frac{2\pi}{\hbar} |M_{fi}|^2 \rho(E_f)$$

Here $\rho(E_f)$ is the final-state level density per energy interval at the energy E_f , and $|J_i M_i \xi\rangle$ and $|J_f M_f \zeta\rangle$ are the wave functions corresponding to the initial and final nuclear states. The quantity H represents the perturbation due to the coupling between nuclear and electromagnetic fields, and ξ, ζ denote quantum numbers other than angular momentum that are necessary to describe the initial and final nuclear states. One can expand the perturbing Hamiltonian H' in multipoles λ, μ as shown in [Won90], and write the dominant electric piece of H' as appropriate to Coulomb excitation, as:

$$O_{\lambda\mu}(E\lambda) = -\frac{i(2\lambda-1)!!}{ck^{\lambda+1}(\lambda+1)} J(r)\nabla \times (r \times \nabla)(j_\lambda(kr)Y_{\lambda\mu}(\theta, \phi)) \quad (\text{B-3})$$

Here the nuclear current density is given by $J(\rho)$, the $j_\lambda(kr)$ are the spherical Bessel functions, and $Y_{\lambda\mu}(\theta, \phi)$ are the spherical harmonics.

The reduced nuclear matrix element is related to the reduced transition strength $B(\lambda)$ – for a given multipolarity λ – via the following relation:

$$B(\lambda(J_i \rightarrow J_f)) = \sum_{\mu M_f} \left| \langle J_f M_f \zeta | O_{\lambda\mu} | J_i M_i \xi \rangle \right|^2$$

$$B(\lambda(J_i \rightarrow J_f)) = \frac{1}{2J_i + 1} \left| \langle J_f \zeta | O_\lambda | J_i \xi \rangle \right|^2 \quad (\text{B-4})$$

After including the level density of the final states, one can express the “up” transition rate $P(E\lambda \uparrow)$ – given by equation B-2 – in relation to the reduced transition strength $B(E\lambda)$ for electric transitions via the relation :

$$P(E\lambda) = \alpha hc \frac{8\pi(\lambda + 1)}{\lambda[(2\lambda + 1)!]^2} \frac{1}{h} \left(\frac{1}{hc} \right)^{2\lambda+1} E_\gamma^{2\lambda+1} B(E\lambda) \quad (\text{B-5})$$

here E_γ is given in MeV, α is $e^2/(\hbar c)$, and $B(E\lambda\uparrow)$ is assumed to be in units of $e^2\text{fm}^{2\lambda}$. For the $E2$ transition found in ^{197}Au ($E_\gamma = 0.548$ MeV), one can combine the constants in this equation to produce a simplified equation for relating the measured transition rate to the reduced transition strength $B(E2\uparrow)$:

$$P(E2\uparrow) = 1.23 \cdot 10^9 E_\gamma^5 B(E2\uparrow) \quad (\text{B-6})$$

Again, E_γ is given in MeV, and $B(E2\uparrow)$ is in units of $e^2\text{fm}^4$. Using B-6, the calculation of $P(E2\uparrow)$ from the relation stated in B-1, and the measured lifetime, we deduce the $B(E2\uparrow)$ values as shown in Table 3.3.

APPENDIX C

DOPPLER SHIFT CORRECTIONS FOR PHOTONS EMITTED FROM FAST MOVING ($\beta \approx 0.3c$) PROJECTILES

We are interested in detecting photons emitted from a projectile moving at a significant fraction of the speed of light ($\beta \approx 0.3c$). The energy deposited by this photon is captured in the detector crystal via scattering or the ejection of an atomic electron in the detector material, with the energy of the latter being converted to light via scintillation. The latter is then delivered and amplified by the photomultiplier tube and quantified in order to deduce the amount of photon energy involved in the decay transition causing the emitted γ -ray. Only electrons produced via the photo-electric effect are detected with the full photon energy and produce a distinct “photopeak” in the NaI light output. The information on the energies of the experimentally-measured γ -decay transitions are used to understand the nuclear structure of the projectile and to construct nuclear decay schemes based on the experimentally-acquired decay energies. In order to construct a useful model of projectile nuclear decay, the accuracy of the experimentally-acquired photon energy must be adequate.

Emission of γ -rays occurring during the process of radioactive decay, for a set of randomly-oriented, non-polarized nuclei, occurs isotropically in the particle frame. In our experiment, the projectile emitting the photon of interest is moving at a speed between $1/4$ and $1/3$ the speed of light. The photons emitted from these projectiles will not be detected in the NSCL γ -detector array at their original energies, rather, the detected energy will be Doppler-shifted in energy due to the angle of emission and the speed of the projectile as described in the following formula :

$$E_{\gamma} = \frac{E_{\gamma_0} \sqrt{1 - \beta^2}}{1 - \beta \cos(\theta)} \quad (\text{C-1})$$

where E_γ denotes the Doppler-shifted energy observed in the laboratory frame, $E_{\gamma,0}$ represents the emission energy of the photon in the moving particle frame (184 and 938 keV for the case of $^{18}\text{F}^m$), β is the velocity of the moving particle emitting the photon with respect to the laboratory frame in units of the speed of light, and θ is the γ -ray emission angle in the laboratory frame relative to the beam direction. The Doppler shift of the photon energy causes the emitted photon to be detected in the laboratory frame at energies that are 75% to 125% of the actual energy of the photon (see Figure 3.5). This Doppler shift of the detected photon energy causes several unique problems that must be addressed in order to accurately determine the original photon energy.

The angular dependence of the Doppler-shifted photon energies (E_γ) can be seen in Figure C.1. For the purposes of our experiment, the NSCL γ -array was configured to detect γ -rays emitted at angles between 45° to 135° in the laboratory frame. This angular range was limited further by the position calibration restriction of using the eight inner position slices instead of all ten (see section 2.2.3).

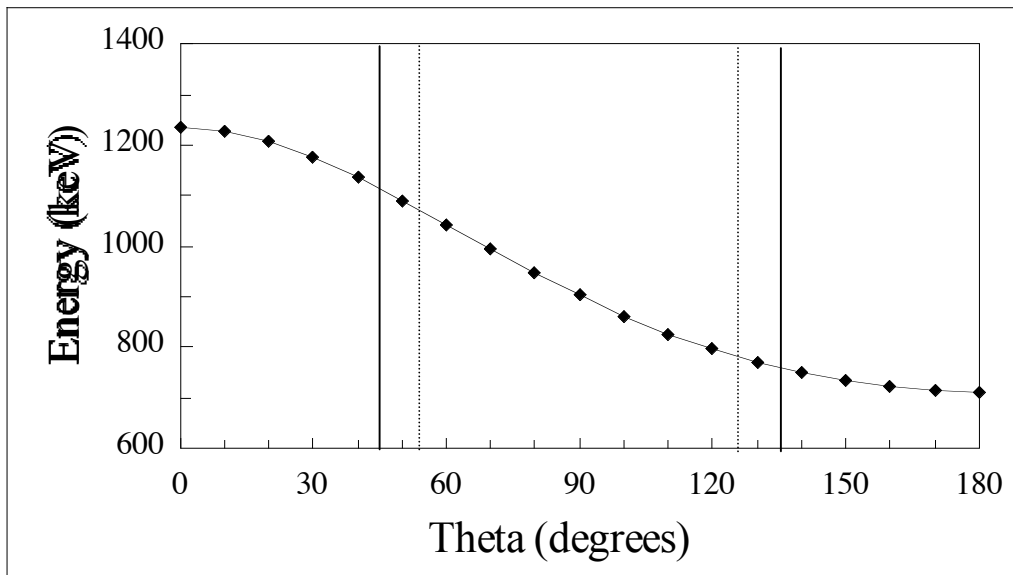


Figure C.1: Doppler-shifted γ -ray energy in the laboratory frame for the 973 keV photon as a function of emission angle in the particle frame. The angular coverage of the NSCL γ -array has been measured to detect γ -rays emitted at angles from 45° to 135° (solid line) from a stationary source placed at the center of the array. The use of only eight inner position calibration slices further restricted these angles to 54° to 126° (dashed line).

For the case of intermediate-energy Coulomb excitation, one would like to Doppler-correct the energies of photons emitted from the subsequent de-excitation of a nucleus involved in a Coulomb interaction with the stationary target. In order to arrive at the original (particle-frame) energy of the detected photon using the equation C-1, one must identify the lab-frame emission angle of the photon. In this experiment, the detected gamma-rays will be emitted very soon (\sim fs) after the interaction of the beam particle with the stationary ^{197}Au target. This allows us to determine the position of the Coulomb-excitation photons in the laboratory frame and accurately calculate the photon emission angle on an event-by-event basis.

This assumption does not hold, however, when examining a nucleus that spontaneously decays at any position with respect to the detector array such as an isomeric beam. Once the position of the photon emission can no longer be correlated with position of the excitation target, the angle of the detected photon cannot be accurately calculated, rendering the Doppler-shift correction useless. With the short half-life of the ^{18}F isomeric state ($T_{1/2} = 163$ ns) and the copious amounts of ^{18}F nuclei produced in the $^{12}\text{C}(^{17}\text{O}, ^{18}\text{F})^{11}\text{B}$ reaction, a large amount of gamma-rays produced in the spontaneous decays of the isomer will be detected in the NSCL detector array which cannot be Doppler corrected. This leads to a large energy range in which Doppler-corrected photons due to Coulomb excitation events will be masked by a large background of Doppler-shifted photons due to the in-flight decay of $^{18}\text{F}^m$. This issue was discussed further in section 4.2.

APPENDIX D

γ-EMISSION DATA FOR ENERGY, EFFICIENCY, AND POSITION CALIBRATIONS

Several calibrated γ-sources were used to generate photons of known energy and emission rate in order to accurately determine detector energy, efficiency, and position calibrations. These were sources of ^{22}Na , ^{60}Co , ^{88}Y , ^{125}Sb , $^{152,154,155}\text{Eu}$, and ^{228}Th . Tables D.1 and D.2 list the applicable data on the photons used in these calibrations.

Table D.1 Photons used for detector energy, efficiency, and position calibrations for the NSCL NaI(Tl) large-angle detector array.

<i>Nuclide</i>	<i>Half-Life</i>	<i>Photon Energy (keV)</i>	<i>Relative Intensity (%)</i>
^{22}Na	2.6088(14) Y	1274.53(2)	99.944(14)
^{60}Co (position only)	5.2714(5) Y	1173.237(4)	99.9736(7)
^{60}Co (position only)	5.2714(5) Y	1332.501(5)	99.9856(4)
^{88}Y	106.65(4) D	898.042(3)	93.7(3)
^{88}Y	106.65(4) D	1836.063(12)	99.2(3)
^{152}Eu	13.537(6) Y	121.777(5)	7.0(9)
^{152}Eu	13.537(6) Y	344.31(3)	2.4(4)
^{152}Eu	13.537(6) Y	841.594(8)	14.2(1.7)
^{152}Eu	13.537(6) Y	963.390(12)	11.7(1.4)

Table D.2 Photons used for detector energy and efficiency calibrations for the two HPGe detectors used to monitor beam purity.

<i>Nuclide</i>	<i>Half-Life</i>	<i>Photon Energy (keV)</i>	<i>Relative Intensity (%)</i>
¹²⁵ Sb	1007.4(4) D	176.313(2)	6.82(21)
¹²⁵ Sb	1007.4(4) D	427.875(6)	29.6(9)
¹²⁵ Sb	1007.4(4) D	463.365(4)	10.5(4)
¹²⁵ Sb	1007.4(4) D	600.600(4)	17.9(6)
¹²⁵ Sb	1007.4(4) D	635.954(5)	11.3(4)
¹⁵² Eu	13.537(6) Y	121.777(5)	7.0(9)
¹⁵² Eu	13.537(6) Y	344.31(3)	2.4(4)
¹⁵² Eu	13.537(6) Y	841.594(8)	14.2(1.7)
¹⁵² Eu	13.537(6) Y	963.390(12)	11.7(1.4)
¹⁵⁴ Eu	8.593(4) Y	123.071(1)	40.6(4)
¹⁵⁴ Eu	8.593(4) Y	247.930(8)	6.91(5)
¹⁵⁴ Eu	8.593(4) Y	591.762(5)	4.96(4)
¹⁵⁴ Eu	8.593(4) Y	723.305(5)	20.11(15)
¹⁵⁴ Eu	8.593(4) Y	873.190(5)	12.20(8)
¹⁵⁴ Eu	8.593(4) Y	996.262(6)	0.893(7)
¹⁵⁴ Eu	8.593(4) Y	1004.25(7)	17.91(12)
¹⁵⁴ Eu	8.593(4) Y	1274.436(6)	35.0(3)
¹⁵⁴ Eu	8.593(4) Y	1596.495(18)	1.788(15)
¹⁵⁵ Eu	4.7611(13) Y	86.545(3)	30.7(7)
¹⁵⁵ Eu	4.7611(13) Y	105.305(3)	21.2(5)

APPENDIX E

MANIPULATION OF EXPERIMENTAL DATA FROM REMOTE LOCATIONS

In order to analyze from remote locations data from the computer programs SMAUG and EXAMINE residing on NSCL computers, commands must be invoked in order to receive the relevant information at the remote terminal.

If the remote computer is running MAC OS:

One must download a Xwindows handler (typically MacX) and configure the handler to accept handshaking from the host containing the experimental data (in the case of MacX, only the activation of the program is required, however other Xwindows programs may need a specific configuration in order to accept commands from remote computers). Once the Xwindows handler has been activated at the terminal location, open a TELNET executable and connect to the NSCL computer:

```
telnet xxxx.nscl.msu.edu
```

Once a connection has been established with the NSCL alpha cluster, a command must be given to inform the NSCL machine to route all visual displays to the remote terminal:

```
set display/create/node=000.000.000.000/transport=TCPIP
```

After the display command has been given, the TELNET session now controls the display capabilities of the NSCL machine. Data analysis programs such as EXAMINE which are windows driven (GUI) can now be controlled remotely.

If the remote computer is running OPEN-VMS:

After logging in to the remote computer running OPEN-VMS, go to the Session Manager/Options/Security menu and enter the following command:

```
TCPIP *.* , *.*
```

This will allow the remote computer to accept display commands from any machine that can be reached by TELNET. Many users can see this as a security risk. If security is an issue on the remote machine you wish to use, you can specify the specific login and machine you wish to communicate with. Once the security command has been given, establish a data connection between the remote terminal and the NSCL host:

```
telnet xxxx.nscl.msu.edu
```

Once a connection has been established with the NSCL alpha cluster, a command must be given to inform the NSCL machine to route all visual displays to the remote terminal:

```
set display/create/node=000.000.000.000/transport=TCPIP
```

After the display command has been given, the TELNET session now controls the display capabilities of the NSCL machine. Programs such as EXAMINE which are windows driven (GUI) can now be controlled remotely.

REFERENCE LIST

REFERENCES

- [Aru89] R.V. Arutyunyan *et al.*, *Kurchatov Institute of Atomic Energy Preprint IAE-4864/2* (1989).
- [Aru91] R.V. Arutyunyan *et al.*, *Sov. J. Nucl. Phys.* **53**, 23 (1991).
- [Bec90] F.D. Becchetti *et al.*, *Phys. Rev.* **C42**, 801 (1990).
- [Boh98] A. Bohr and B.R. Mottelson, *Nuclear Structure, Vol.1 and 2*, (World Scientific, 1998).
- [Bou92] J.A. Bounds and P. Dyer, *Phys. Rev.* **C46**, 852 (1992).
- [Bro95] J.A. Brown *et al.*, *Phys. Rev.* **C51**, 1312 (1995).
- [Col82] C.B. Collins *et al.*, *J. Appl. Phys.* **53**, 4645 (1982).
- [Col88] C.B. Collins, C.D. Eberhard, J.W. Glesener, and J.A. Anderson, *Phys. Rev.* **C37**, 2267 (1988)
- [Col99] C.B. Collins *et al.*, *Phys. Rev. Lett.* **82**, 695 (1999).
- [Cue89] N. Cue, J-C. Poizat, and J. Remillieux, *Europhys. Lett.* **8**, 19 (1989).
- [Dey98] P. A. DeYoung *et al.*, *Phys. Rev.* **C58**, 3442 (1998).
- [Dra98] G. Dracoulis and P. Walker, *Science Spectra* **12**, 50 (1998).
- [Fir96] Richard B. Firestone, Virginia S. Shirley, Coral M. Baglin, S.Y. Frank Chu, and Jean Zipkin, *The 8th edition of the Table of Isotopes*, (John Wiley & Sons, Inc., 1996).
- [Fog71] B. Fogelberg and A. Backlin, *Nucl. Phys.* **A171**, 353 (1971).
- [Fuj84] H. Fujioka *et al.*, *Z. Phys. A* **315**, 121 (1984).
- [Gei95] H. Geissel *et al.*, *Annu. Rev. Nucl. Part. Sci.* **45**, 163 (1995).
- [Gla97] T. Glasmacher *et al.*, *Phys. Lett. B* **395**, 163 (1997).
- [Har99] M.R. Harston and J.F. Chemin, *Phys. Rev.* **C59**, 2462 (1999).

- [Ibb98] R. W. Ibbotson, T. Glasmacher, B. A. Brown, L. Chen, M. J. Chromik *et al.*, *Phys. Rev. Lett.* **80**, 2081 (1998).
- [Irw97] G.M. Irwin and K.H. Kim, *Phys. Rev. Lett.* **79**, 990 (1997).
- [Iza79] Y. Izawa and C. Yamanaka, *Phys. Lett.* **88B**, 59 (1979).
- [Kel94] H.Keller *et al.*, *Z.Phys.* **A348**, 67 (1994).
- [Kol98] J. J. Kolata *et al.*, *Phys. Rev. Lett.* **81**, 4580 (1998).
- [Lak95] L. Lakosi, N.C. Tam, and I. Pavlicsek, *Phys. Rev.* **C52**, 1510 (1995).
- [Liu96] J.-f. Liu, Y.-s. Zhang, C.-y. Yang, J.-f. Shen, and B. A. Robson, *Phys. Rev.* **C 54**, 2509 (1996).
- [Mat98] S. Matinyan, *Phys. Rep.* **298**, 199 (1998).
- [May48] M. G. Mayer, *Phys. Rev.* **74**, 235 (1948).
- [Mcg71] F.K. McGowan *et al.*, *Ann.Phys.(N.Y.)* **63**, 549 (1971).
- [Mye66] W.D. Myers, and W.J. Swiatecki, *Nucl. Phys.* **88**, 1 (1966).
- [Pri99] Pritychenko *et al.*, NSCL publication MSUCL-1128, submitted for publication to *Phys. Lett. B*, July 1999.
- [Rob95] D.A. Roberts *et al.*, *Nuc. Phys. A* **58**, 247c (1995).
- [Sai80] T. Saito *et al.*, *Phys. Lett.* **B92**, 293 (1980).
- [Sat90] G.R. Satchler, *Introduction to Nuclear Reactions* (Oxford University Press, 1990).
- [Sch96] H. Scheit, T. Glasmacher, B. A. Brown, J. A. Brown, P. D. Cottle *et al.*, *Phys. Rev. Lett.* **77**, 3967 (1996).
- [She91] B.M. Sherrill *et al.*, *Nucl. Instrum. Methods* **B56**, 1106 (1991).
- [Sin85] K. P. Singh, D. C. Tayal, G. Singh, and H. S. Hans, *Phys. Rev.* **C 31**, 79 (1985).
- [Sou92] G. A. Souliotis and D. J. Morrissey *et al.*, *Phys. Rev.* **C46**, 1383 (1992).
- [Swa84] D. Swan, J. Yurkon, D.J. Morrissey, *Nucl. Instrum. Methods* **A348**, 314 (1984).
- [Uzu94] J.L.Uzureau *et al.*, *Phys.Lett.* **331B**, 280 (1994).
- [Wal97] P.M. Walker *et al.*, *Phys. Lett. B* **408**, 42 (1997).

[War95] R. E. Warner *et al.*, *Phys. Rev.* **C52**, 1166 (1995).

[Won90] S.S.M. Wong, *Introductory Nuclear Physics* (Prentice Hall, 1990).

[Yen92] S. J. Yennello *et al.*, *Phys. Rev.* **C46**, 2620 (1992).